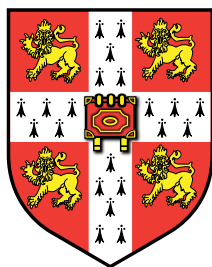


Chemical Softness as a Predictor for  
Reactivity at Metal Surfaces.



This thesis is submitted for the degree of Doctor of Philosophy

Amy Louise Gunton

Magdalene College  
University of Cambridge

November 17, 2023

## **Declaration**

This thesis is the result of my own work and includes nothing which is the outcome of work done in collaboration except as declared in the Preface and specified in the text. I further state that no substantial part of my thesis has already been submitted, or, is being concurrently submitted for any such degree, diploma or other qualification at the University of Cambridge or any other University or similar institution except as declared in the Preface and specified in the text. It does not exceed the prescribed word limit for the Degree Committee for the Faculty of Physics and Chemistry.

## Abstract

### Chemical Softness as a Predictor for Reactivity at Metal Surfaces

Amy Louise Gunton

Heterogeneous catalysis is an important global industry, but there are many gaps in our understanding of catalytic selectivity. Reactivity indices are helpful for predicting selectivity, and it would be useful to have a reactivity index which can be applied to metal surfaces and adsorbates. The local softness is a reactivity index based on Pearson's theory of hard and soft acids and bases. It is the derivative of the local electron density with respect to the chemical potential, at constant external electric potential. It can be calculated simply for molecules or nanoparticles which have a band gap. However, the calculation for conductors is less straightforward.

In this work, a method was developed to calculate the local softness of metal surfaces using density functional theory. This required a solution to the problem of increasing the chemical potential while keeping the external electric potential constant, which is difficult to do in charged cells with periodic boundary conditions. This problem was solved by correcting for a shift in energy reference with charge and by extrapolating to an infinitely sized unit cell. The local softness was visualised using isosurfaces and colourplots and was used to compare predicted reactivity between different sites on various metal surfaces.

In order to get a measure of the softness of individual atoms on a surface, Bader's theory of atoms in molecules was used to integrate the local softness over the regions of atomic volume. The resulting reactivity index, the atomic softness, was used to predict the adsorption energy of carbon monoxide on eighteen different metal surfaces. The local and atomic reactivity indices were also used to study directing effects for aromatic adsorbates on the Pt{111} surface. The local and atomic softness were found to be useful for predicting reactivity trends between different sites on metal surfaces and for adsorbates.

## Acknowledgements

I would like to acknowledge EPSRC for their funding without which I could not have done my studies. I would like to thank my supervisor Professor Stephen Jenkins for his wise advice and support. I would also like to thank the other past and present members of the Jenkins group for useful and interesting discussions. In particular I would like to thank Dr Bianca Provost, Dr Sabine Matysik and Dr Israel Temprano. I would also like to thank everyone else who has encouraged me on the journey of writing this thesis, especially my husband, my mum, my sister and my friends Dr Esther Johnston, Dr Spencer Johnston, Dr Ming-Hsuan Wen, the Reverend Mrs Helen Bence, Charlotte Walton and Greg Walton.

1 Corinthians 10:31 'whatever you do, do it all for the glory of God.'

# Contents

<b>1</b>	<b>Introduction</b>	<b>2</b>
1.1	Heterogeneous catalysis . . . . .	3
1.2	Active sites in catalysis . . . . .	4
1.2.1	Disambiguation: ‘active sites’ in heterogeneous and homogeneous catalysis . . . . .	6
1.2.2	Finding active sites for heterogeneous catalysts . . . . .	7
1.3	Surface science approach to catalysis . . . . .	8
1.4	Scaling relations and volcano plots . . . . .	10
1.5	Reactivity indices . . . . .	11
1.5.1	Hard and soft acids and bases . . . . .	12
1.6	Local reactivity indices . . . . .	13
1.6.1	Reactivity indices based on metallic electronic theory . . . . .	14
1.6.2	Local reactivity indices based on HSAB . . . . .	17
1.7	Calculating the local softness . . . . .	20
1.8	Approximating the local softness: The Fermi softness . . . . .	21
1.9	New method of calculating local softness . . . . .	23
1.10	Summary of this thesis . . . . .	24
<b>2</b>	<b>Methodology</b>	<b>26</b>
2.1	Electronic structure theory . . . . .	26
2.2	Approximations often used for chemistry . . . . .	28
2.2.1	Born-Oppenheimer approximation . . . . .	28

2.3	Density functional theory . . . . .	29
2.3.1	Hohenberg-Kohn theorems . . . . .	30
2.3.2	Thomas-Fermi theory . . . . .	32
2.3.3	Kohn-Sham equations . . . . .	33
2.3.4	Local density approximation . . . . .	35
2.3.5	Generalised gradient approximation . . . . .	37
2.3.6	Costs and accuracy of DFT . . . . .	38
2.4	Plane-wave pseudopotential method . . . . .	39
2.4.1	Plane waves . . . . .	39
2.4.2	Pseudopotentials . . . . .	41
2.4.3	Fast Fourier transforms . . . . .	43
2.4.4	Energy-minimisation algorithms . . . . .	43
2.5	Surfaces studied . . . . .	44
2.6	Computational details . . . . .	45
2.7	Notation to describe supercell geometry . . . . .	48
2.7.1	Choice of slab and vacuum thickness . . . . .	48
2.8	Problems calculating local softness . . . . .	49
2.8.1	Charged calculations in CASTEP . . . . .	49
2.8.2	CASTEP energy reference . . . . .	49
2.9	Calculating the local softness . . . . .	50
2.10	Calculating the chemical potential . . . . .	52
2.10.1	Uncorrected chemical potential . . . . .	52
2.10.2	The CASTEP energy reference . . . . .	53
2.10.3	Slab average potential correction . . . . .	55
2.10.4	DOS correction method: bands2dos . . . . .	57
2.10.5	DOS correction method: OptaDOS . . . . .	57
2.10.6	Computational details for spectral tasks and OptaDOS . . . . .	60
<b>3</b>	<b>Calculating the Denominator of Local Softness</b>	<b>61</b>
3.1	Convergence of uncorrected properties . . . . .	62
3.1.1	Convergence of the numerator of local softness . . . . .	62
3.1.2	Uncorrected denominator convergence . . . . .	63
3.1.3	Convergence of $\mu$ and slab average potential . . . . .	65

3.1.4	Implications for the method of calculating $\mu$ . . . . .	72
3.2	Slab average potential correction . . . . .	72
3.2.1	Convergence with slab thickness . . . . .	73
3.2.2	Convergence with vacuum thickness . . . . .	76
3.2.3	Convergence with surface-normal supercell dimension . . . . .	77
3.2.4	Problems with slab average potential correction . . . . .	79
3.2.5	Friedel oscillations in the xy-average potential . . . . .	81
3.3	DOS cross-correlation correction . . . . .	82
3.3.1	Comparing OptaDOS broadening methods . . . . .	83
3.3.2	Convergence with surface-normal supercell dimension . . . . .	84
3.3.3	Varying ratio of slab to vacuum thickness . . . . .	88
3.3.4	Varying the DOS range for cross-correlation . . . . .	90
3.4	Denominator convergence for eighteen metal surfaces . . . . .	97
3.5	Summary . . . . .	101
<b>4</b>	<b>Visualising the Local Softness of Clean Metal Surfaces</b>	<b>104</b>
4.1	Isosurfaces of local softness for copper . . . . .	105
4.1.1	Cu{100} . . . . .	105
4.1.2	Cu{111} . . . . .	106
4.1.3	Cu{110} . . . . .	113
4.2	Colourplots of the local softness for eighteen surfaces . . . . .	114
4.2.1	Top-down views . . . . .	116
4.2.2	Side views . . . . .	125
4.3	Summary . . . . .	125
<b>5</b>	<b>Atomic Softness:</b>	
	<b>Predicting CO Adsorption Energy</b>	<b>127</b>
5.1	Bader's theory of atoms in molecules . . . . .	128
5.2	Calculating atomic softness . . . . .	129
5.3	Calculating CO adsorption energy . . . . .	129
5.3.1	Literature review of CO binding sites . . . . .	129
5.3.2	Slab and vacuum thickness . . . . .	135

5.3.3	Adsorption energy calculation methodology . . . . .	136
5.4	Predicting CO adsorption energy from atomic softness . . . . .	136
5.4.1	Predicting CO adsorption: experimental sites . . . . .	136
5.4.2	Predicting CO adsorption: atop sites . . . . .	140
5.4.3	General observations . . . . .	143
5.4.4	Trends for individual facets . . . . .	144
5.5	Summary . . . . .	146
<b>6</b>	<b>The Local and Atomic Softness of Aromatic Adsorbates</b>	<b>147</b>
6.1	Directing effects in aromatic adsorbates . . . . .	149
6.2	Computational methods used to study aromatic adsorption . . . . .	150
6.3	Adsorption energy and optimised geometry for aromatic adsorbates . . . . .	151
6.4	Local softness of aromatic adsorbates . . . . .	155
6.5	Visualising the atomic softness of aromatic molecules on platinum . . . . .	163
6.6	Testing the approximation of using the clean-surface denominator . . . . .	166
6.7	Summary . . . . .	167
<b>7</b>	<b>Summary and Outlook</b>	<b>169</b>
7.1	Analysing the local softness of clean metal surfaces . . . . .	171
7.2	Calculating the atomic softness for clean metal surfaces . . . . .	172
7.3	Using the chemical softness to predict directing effects in aromatic adsorbates . . . . .	173
7.4	Further work . . . . .	175
7.5	Conclusions . . . . .	177
<b>A</b>	<b>Computational Details</b>	<b>178</b>
A.1	Calculation of lattice constants . . . . .	178
A.2	Supercell geometries for CO adsorption calculations . . . . .	180
A.3	Aromatic adsorption computational details . . . . .	180



# Chapter 1

## Introduction

The use of metals as structural materials, catalysts and in other applications represents a significant percentage of the world's Gross Domestic Product (GDP).<sup>1,2</sup> In all of these applications a surface or interface will be present. In many cases this is key to material or catalyst performance.<sup>3</sup> The importance of understanding the properties of metal surfaces and interfaces may be exemplified by the problems of corrosion. Corrosion at metal surfaces is a hugely significant industrial problem worldwide.<sup>4</sup> In fact, for most countries corrosion costs between 2-5% of the Gross National Product (GNP).<sup>5</sup> Controlling the properties of metal surfaces to prevent corrosion is essential in order to ensure the safety of industrial workers and others.<sup>6</sup> However, the prevention of corrosion, while necessary for safety and economy, itself comes with an environmental cost. For example, one of the main methods used to prevent corrosion is painting, but paint, for example on ships, degrades with time to release toxic particles which can poison marine organisms.<sup>7</sup>

Another important use of metals where understanding of the surface is needed is heterogeneous catalysis. The use of metal nanoparticles and metal-oxide surfaces as catalysts is key for the production of many important chemicals used worldwide.<sup>8-10</sup> The properties of heterogeneous catalysts are dominated by the characteristics of the surface.<sup>3</sup> Due to the importance of the properties of metals in general and their surfaces in particular, it is desirable to

understand these as well as possible. This would enable a more informed approach to catalyst design and corrosion prevention.

## 1.1 Heterogeneous catalysis

Heterogeneous catalysis is the process where fluid reactants (i.e. liquids or gases) are passed over a finely-divided metal or metal-oxide surface.<sup>11</sup> This finely-divided surface often consists of metal nanoparticles on a metal-oxide support.<sup>2</sup> The support stabilises the nanoparticles and prevents coarsening. The interaction between reactant molecules and the catalyst allows a different reaction mechanism to occur to form the product. This mechanism has a lower thermodynamic barrier than for the reaction without the catalyst. A lower reaction-energy barrier results in a faster reaction rate at a given temperature and pressure. This also allows the reaction to happen in milder conditions, which is generally more environmentally friendly.<sup>12</sup> The catalyst surface enables a higher rate of reaction and can be used multiple times for this purpose without being consumed.<sup>12</sup> The advantages of heterogeneous catalysts (over homogeneous catalysts which are in the same phase as the reactants and products) include high durability, the potential for continuous flow reactions and the potential for lower cost.<sup>13</sup> Ease of separating catalyst and products results from the catalyst being in the solid phase whereas the reactants and products are in the gas or liquid phase.<sup>11</sup>

Control of catalytic processes is very important, as it enables production of the desired product in high yield. It is very rare for any reaction to only have one product, as generally a variety of products are formed. For a given catalytic process, the desired product is rarely the most thermodynamically stable of a set of possible products.<sup>12</sup> There are two key concepts which describe the behaviour of a catalyst. These are activity and selectivity. Activity is a measure of the rate of the catalysed reaction. Selectivity is a measure of the extent to which a catalyst promotes one specific reaction resulting in the desired product over those which produce by-products.<sup>11</sup> A catalyst may be highly active but produce a mixture of products, where the desired

product is a small minority. In contrast, a selective catalyst results in a high proportion of the desired product.

For a reaction with several possible products, the catalyst modifies the kinetic favourability of the formation of products and intermediates.<sup>12</sup> An optimal catalyst will be selective - it will make forming the desired product more kinetically favourable and forming undesirable by-products less favourable (or at least relatively less favourable). In this way, the equilibrium of species in the reaction chamber will be shifted towards the desired product as opposed to starting material or by-products. In addition it is important for the catalyst to be as active as possible, so that the rate of reaction is high.

The catalyst surface has a subtle set of roles, including slowing undesirable processes while enabling desirable processes. In order for a catalyst to be optimal for a given reaction, the catalyst surface must bind reactants strongly enough for activation. However, if the reactants are too strongly bound the reaction will not proceed. Also, if products or by-products bind to the catalyst too strongly there will be less catalyst surface available. This will result in a lower rate (i.e. poisoning). These observations led to the Sabatier principle, which is a theory that intermediate reactivity is best for catalysts.<sup>14</sup> Very reactive catalysts do not allow products to leave, whereas very unreactive catalysts do not form a strong enough interaction with reactants to influence the reaction rate.<sup>1</sup>

## 1.2 Active sites in catalysis

An important measure of catalytic activity is the turnover frequency (TOF), otherwise known as the turnover rate (TOR).<sup>15</sup> This is the number of product molecules formed per second per active site.<sup>15,16</sup> An active site is the site at which the catalysis occurs (the site at which reactants bind and are converted to products). In homogeneous catalysis, where the catalyst consists of a small metal complex, there is one active site per catalyst particle, which makes the turnover frequency easy to calculate.<sup>16</sup>

In comparison, heterogeneous catalysts, consisting generally of nanoparticles on a support, have a multitude of different sites present. The nature and number of these sites is generally not known, unlike in homogeneous catalysis. In calculating the TOF for heterogeneous catalysts, it is generally assumed that every surface atom is an active site. This estimate allows the nominal TOF to be calculated, which will be a lower limit to the real TOF.<sup>15</sup> For some heterogeneous catalytic processes, the nominal TOF is a good approximation. The number of active sites is proportional to the number of atomic sites.<sup>15</sup> The processes for which this is true are known as structure-insensitive reactions.<sup>15</sup>

However, this is not always the case. For many catalytic processes the majority of the reaction turnover occurs on only a small subsection of the available sites.<sup>17</sup> These active sites consist of an ensemble of atoms, and different surface facets and different nanoparticle sizes can have dramatically different TOFs. This class of catalytic processes are known as structure-sensitive reactions.<sup>15</sup> For catalytic processes that are structure-sensitive, rates of reaction on different facets may vary by up to two orders of magnitude.<sup>18,19</sup> Examples of structure-sensitive reactions include the dehydrocyclisation of alkanes to aromatic hydrocarbons on platinum and ammonia synthesis on iron.<sup>19,20</sup>

For structure-sensitive catalytic processes, the large number of different sites which are present can cause a problem. The reaction will occur at different rates in different localities. Different sites may have varying selectivity for particular reactions. Some sites may catalyse side reactions resulting in the formation of unwanted by-products, which may even poison the catalyst itself.<sup>10,21</sup> If it is known what type of sites catalyse the desired reaction and which catalyse unhelpful side reactions, then catalyst selectivity can be systematically improved. For example, sites which catalyse unhelpful side reactions could be selectively blocked.

There are great advantages to identifying and characterising active sites. For structure-sensitive reactions the number of active sites is highly dependent on catalyst geometry. Therefore it can be deduced that knowledge of the

active sites can allow rational catalyst design.<sup>22,23</sup> This should allow more active and selective catalysts to be made. This would reduce the cost of a catalytic procedure and reduce wasteful side reactions.

### 1.2.1 Disambiguation: ‘active sites’ in heterogeneous and homogeneous catalysis

The term ‘active site’ is used in both homogeneous and heterogeneous catalysis. It is important to note several key differences in heterogeneous catalysis in comparison to homogeneous catalysis. This makes active sites much more difficult to identify and characterise in heterogeneous catalysis. In heterogeneous catalysis, the active site is the location or set of locations at which the rate of the desired reaction is locally maximised. Reactions that occur at the active site have the most favourable rate and yield of the desired product.

Homogeneous catalysts are molecular complexes with well defined structures. While there may be changes to the structure of the catalyst during the course of a reaction this is between two or three known structures. The structure of homogeneous catalysts varies little in reaction conditions and can be characterised. This helps in finding and characterising active sites. Homogeneous catalysts tend to have only one active site which can be found, controlled and modified with relative ease.<sup>13</sup>

In contrast, the structure of working heterogeneous catalysts is very difficult to study. The clean catalyst surface may little resemble the catalyst surface found under reaction conditions. In particular, the so called temperature and pressure gap makes it difficult to study active catalysts as many of the best structural characterisation techniques work best at high (or even ultra-high) vacuum and low temperature. The structure of the working catalyst is rarely fully characterised. In many systems, the catalyst structure used for calculations can be thought of as an educated guess.<sup>22</sup>

In addition to the problems of characterising heterogeneous catalyst structure, it is known that a multitude of different sites will be present.<sup>24</sup> All

of these sites can be expected to have some catalytic ability either for the desired reaction or for side reactions. Generally it is difficult to characterise the properties of individual sites on a catalytic surface. Identifying active sites in heterogeneous catalysis is therefore extremely challenging. There have been, however, various studies where active sites have been found, often by extensive experimental work involving several complementary techniques.<sup>25,26</sup>

Obtaining physical insight into the reactivity of catalytic materials is highly desirable. This may allow greater control of heterogeneous processes and the systematic design of catalytic processes. In particular, an important area of research is searching for a way to predict the active sites for stereospecific reactions.<sup>2</sup> Studying the reactivity of molecules adsorbed on metal surfaces may provide insight into the mechanism of reactions. Together, these increases in understanding could enable the design of more specific heterogeneous catalysts. This could enable heterogeneous catalysts to make progress towards the degree of control available with homogeneous catalysts.<sup>2</sup>

Properties of heterogeneous catalysts include turnover frequency, activity, selectivity, stability, lifetime and resistance to poisoning.<sup>12,20</sup> To understand the behaviour of heterogeneous catalysts it is important to characterise these properties. Many of these properties are strongly related to reactivity. Therefore it is desirable to understand the reactivity of metal surfaces better, both with and without adsorbates. This may then allow greater understanding of the impact of reactivity on properties such as activity and selectivity.

### **1.2.2 Finding active sites for heterogeneous catalysts**

As discussed above, finding the active sites for a given process allows for systematic catalyst design and improvement. Different sites on a metal catalyst often catalyse different reactions.<sup>27</sup> For example, Pestman and co-workers<sup>27</sup> investigated the Fischer-Tropsch reaction and found that while step-edge sites were important for chain elongation, the terrace sites were important for chain termination. Therefore, by modifying the composition of sites in the

catalyst, it was possible to modify the length of the hydrocarbon molecules formed.<sup>27</sup> Many studies have also found that the rate of the CO dissociation step in Fischer-Tropsch synthesis is higher for step-edge sites than for terrace sites.<sup>28</sup> It would be valuable to have a descriptor that can compare the properties of step-edge sites with those of terrace sites. This would enable processes such as Fischer-Tropsch synthesis to be better understood.

### 1.3 Surface science approach to catalysis

Heterogeneous catalysts tend to consist of metal nanoparticles on an oxide support.<sup>20</sup> Industrial catalytic processes occur at high temperatures and pressures. These extreme conditions limit the number of techniques which can be used to study working catalysts. In addition, at the high temperatures and pressures of a working catalyst, it can be expected that there may be significant disorder.<sup>29</sup> The nanoparticles may not be well defined in their shape and other properties but may fluctuate between different shapes and sizes based on what adsorbates are bound. This results in a dynamic and highly-correlated system. It can be clearly seen that there will be a large number of different sites present on a working catalyst but it is difficult to know what those sites will be like.

The traditional way to study catalysis is to look at the behaviour of the catalyst under realistic working conditions. By controlling and varying the temperature, pressure and flow of reactants, and by measuring the synthesis of products, a great deal of information can be deduced indirectly.<sup>24</sup> Benefits of this approach are that any conclusions drawn must be true of the real industrial system. However, this indirect approach has drawbacks, for example in terms of finding out exactly what geometry the active sites might have. Most techniques which could be used to study surfaces only work at low temperature and ultra-high vacuum. This problem is known as the temperature and pressure gap.

In contrast to the catalysis approach, the surface science approach involves studying a model catalyst that is much simpler than the real catalyst, but can

be investigated thoroughly using surface science techniques. Unfortunately, these techniques generally require ultra-high vacuum and low temperature, which differs from reaction conditions, but they allow the catalyst surface to be very precisely characterised. One example of this approach was used by Sabatier and others to characterise a model catalyst before and after operation.<sup>18,21</sup> This surface science approach to catalysis can be used to understand the structural sensitivity of reactions and to find the active sites.<sup>18</sup>

Many aspects of the reactivity of surfaces are still not well understood. Metal surfaces are typically very rough with a vast number of different microfacets each containing a variety of different sites. The behaviour of catalysts as a whole is difficult to categorise in terms of individual sites and often a more general system approach is taken. An example of this is microkinetic modelling, which involves various assumptions.<sup>30</sup> One of these assumptions involves generalising from many sites at which catalytic events take place to one type of site for a given catalytic process. The properties of these sites are found from the average properties of the catalyst as a whole.<sup>30,31</sup>

However, since the work of Langmuir, Armstrong, Hilditch and Taylor, it has long been hypothesised that the majority of catalytic events take place on a minority of the sites.<sup>17,32,33</sup> In particular, their work found that a very small amount of poisoning agent reduced the catalytic activity by several orders of magnitude.<sup>32</sup> This is consistent with a small number of active sites accounting for the majority of catalytic events.<sup>17,33</sup> More recently the active sites for various reactions have been found.<sup>34</sup>

In order to test this hypothesis it is necessary to build greater understanding of the properties of individual sites on a metal surface. This may confirm the ‘active sites hypothesis’, in which case it would be highly desirable to identify and characterise the active sites. The identification and characterisation of the active sites would have great potential for the systematic design of heterogeneous catalysts.

## 1.4 Scaling relations and volcano plots

It has generally been observed in surface processes that the activation energy for catalytic properties tends to be a linear function of the reaction energy.<sup>1,35,36</sup> These linear Brønsted-Evans-Polanyi (BEP) relations can be deduced by considering the transition state as the position where two hypothetical potential-energy curves (one for the reactants and one for the products) intersect. An increase in the reaction enthalpy would result in one of the potential-energy curves being rigidly shifted relative to the other, with a resulting linear change in activation energy.<sup>36</sup> Therefore there is a linear relationship between the reaction enthalpy and the activation energy of a given process. Plots of these relations can be very useful in rationalising the differences in the reactivity of surfaces. In particular the BEP approach allows the activation energy  $E_a$  to be expressed as

$$E_a = \alpha\Delta E + \beta \quad (1.1)$$

where  $\Delta E$  is the reaction energy. Equation 1.1 is taken from the 2008 review by Nørskov et al.<sup>36</sup> The authors suggested that the slope ( $\alpha$ ) of a BEP line gives information about the electronic component of reactivity, whereas the offset ( $\beta$ ) gives information about the purely geometric part.<sup>36</sup>

It can be argued from BEP relations that as the reactivity of a surface increases, the activation energy of adsorption steps will decrease due to reactants binding more strongly to the surface. However, this will be offset by an increase in activation energy of desorption of products and for on-surface reactions.<sup>10</sup> Therefore, as observed much earlier by Sabatier<sup>14</sup>, the activation energy for the reaction as a whole indicates a minimum for metal surfaces which are neither highly reactive nor highly noble.<sup>1</sup> This can be rationalised in terms of very reactive metals having a high barrier for desorption, whereas very noble metals have a high barrier for forming metal-adsorbate bonds.<sup>36</sup> Therefore for a series of metal species of increasing reactivity, the activation energy will first increase, then reach a peak and then decrease. A plot of the activation energy with respect to the reactivity of catalytic materials is

therefore called a volcano plot.<sup>10</sup>

The Sabatier approach, as discussed above, can be used to predict the catalytic activity of individual sites. However, this involves making certain assumptions implicit in the surface science approach to catalysis. For example, this analysis involves making the assumption that catalytic surfaces, which generally are made up of nanoparticles on a support, can be thought of as consisting of various crystal facets with sites such as step edges and kink atoms.<sup>1,35</sup> The question of to what extent the behaviour of a catalyst can be divided up into a set of more or less independent sites is one of some debate.<sup>12,18,21,31,37</sup>

There are a variety of different properties that characterise a particular site on a surface. These include activity (turnover frequency) and reactivity (binding strength). The latter is often studied directly through the binding energy of a set of adsorbates, as described above. However, the binding energy is a property of both the metal and the adsorbate. In order to gain physical insight into the reactivity of the metal itself and make comparisons and predictions for metals in general, it is desirable to use a reactivity index. This enables a quantitative comparison of the reactivity of different sites, metals and adsorbates to be made.

## 1.5 Reactivity indices

Reactivity indices can, following the approach of Chermette, be separated into three main groups.<sup>38</sup> The first of these groups comprises electronegativity and global reactivity indices based on the theory of hard and soft acids and bases (HSAB). The other groups are local reactivity indices and non-local response functions. There can also be reactivity indices which fall into two of these groups, for example the Fukui function is a local reactivity index based on HSAB theory.<sup>39,40</sup>

### 1.5.1 Hard and soft acids and bases

The concept of hard and soft acids and bases, developed by Pearson in 1963, has inspired the development of many global, local and non-local reactivity indices.<sup>41</sup> This theory states that soft acids will be most reactive with soft bases. Softness qualitatively implies low net charge and high polarizability, whereas hardness means the opposite.<sup>42</sup> Pearson’s theory was made quantitative after the advent of conceptual DFT with the global reactivity indices of hardness and softness.<sup>43</sup> The global hardness and softness are sometimes called molecular properties as they give a single number to characterise the reactivity of a whole molecule. The use of these descriptors, however, is not restricted to organic molecules and they have even been used for nanoparticles.<sup>44</sup> The global hardness,  $\eta$ , characterises the hardness of a molecule or nanoparticle.  $\eta$  is defined in DFT as

$$2\eta = \left( \frac{\partial \mu}{\partial N} \right)_v = \left( \frac{\partial^2 E}{\partial N^2} \right)_v \quad (1.2)$$

where  $\mu$  is the chemical potential,  $N$  is the number of electrons,  $E$  is the energy as obtained by DFT and  $v$  is the external potential.<sup>45</sup> The chemical potential is defined as the energy of an infinitesimally small test charge when added to a system. Within the conceptual framework of density functional theory the chemical potential can be expressed as

$$\mu = \frac{\delta E}{\delta \rho(\mathbf{r})} \quad (1.3)$$

where the quantity on the right is a functional derivative of the energy with respect to the electron density.<sup>43</sup> The global softness, the inverse of the global hardness, is defined as

$$S = \left( \frac{\partial N}{\partial \mu} \right)_v = \frac{1}{2\eta} \quad (1.4)$$

where  $N$ ,  $\mu$ , and  $v$  are defined as above for Eqn. 1.2.<sup>40</sup> Generally, the chemical potential, hardness and softness are approximated using a finite-difference

approximation. Within this approach  $\mu$  is approximated as

$$\mu \approx \frac{I + A}{2} \quad (1.5)$$

where  $I$  and  $A$  are the ionisation potential and the electron affinity respectively.<sup>43</sup> Similarly the hardness can be approximated as

$$\eta \approx \frac{I - A}{2} \quad (1.6)$$

where it is important to note that this relies on the band gap being non-zero.<sup>43</sup> This assumption is valid for organic molecules and nanoparticles but can be expected to break down for bulk metal surfaces. By substituting Eqn. 1.6 into Eqn. 1.4, the finite-difference approximation to the global softness,

$$S \approx \frac{1}{I - A} \quad (1.7)$$

is obtained.<sup>46</sup> It can be deduced that the denominator of Eqn. 1.7 would go to zero for a bulk conductor with no band gap. This would then mean that the local softness itself would therefore diverge.

## 1.6 Local reactivity indices

Global reactivity indices are useful for understanding the reactivity of whole nanoparticles, which can elucidate the reactivity of catalytic surfaces. It is also helpful, however, to have a measure of the relative reactivity of different sites on a surface. Local reactivity indices quantify reactivity as a function in three-dimensional space. The main local reactivity indices in use for studying catalytic systems fall into two main groups. Some, such as the Wilke function and d-band centre, can only be used to describe the reactivity of metals. Others, such as the Fukui function and local softness, are derived from HSAB theory (discussed earlier in Section 1.5.1) and can be used for metals and adsorbates.

## 1.6.1 Reactivity indices based on metallic electronic theory

### The d-band centre

The d-band centre was developed by Hammer, Nørskov and co-workers as a measure of transition-metal reactivity.<sup>1,47,48</sup> Essentially the d-band centre is a measure of energy of the ‘centre of mass’ of the d band at a particular point in space.<sup>1</sup> In order to find this quantity, first the local Density of States (DOS) must be calculated and then projected onto the metal d orbitals.<sup>47</sup> Then the resulting spectrum of DOS for different energy can be analysed to find the energy of the ‘centre of mass’ of the d band, as illustrated in Fig. 1.1.<sup>49</sup> This energy,  $\epsilon_d$ , is measured relative to the Fermi level, following the convention that the Fermi level is set as zero on DOS spectra. The d-band centre is shown for an example metal in Fig. 1.1.

The difference in energy between the d-band centre and the Fermi level has been shown to be related to the reactivity. This is because the closer the d-band centre is to the Fermi level, the more the d-band states can interact with the frontier orbitals of adsorbed molecules. This means there will be more antibonding orbitals pushed high in energy above the Fermi level, which can then become unoccupied. Alternatively, bonding states can be shifted down in energy below the Fermi level and become occupied.<sup>1</sup>

The d-band centre has been extensively used to explain trends in reactivity between different transition metals, surfaces and catalysts.<sup>1,49</sup> For example, Hammer and co-workers found that there was a strong linear trend between the d-band centre and the adsorption energy of CO at different sites on flat, stepped and kinked platinum surfaces.<sup>50</sup> Recent applications of the d-band centre include elucidating activity of single cluster catalysts<sup>51</sup> and predicting hydrogen diffusion on different gold facets<sup>52</sup>. However, the limitation of this reactivity index is that in being specific to transition-metal atoms, only some of the reactivity of a catalytic system can be studied with it. This method therefore cannot be used to predict the reactivity of adsorbate atoms.

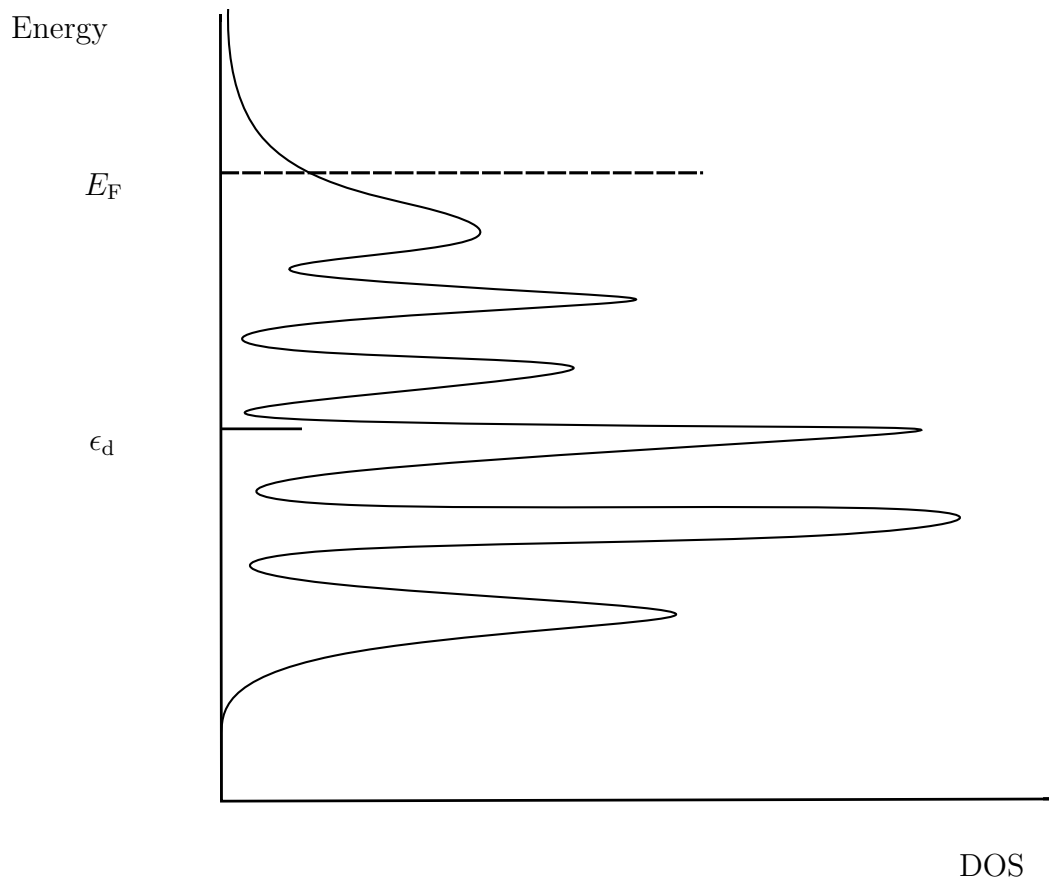


**Figure 1.1:** Hypothetical DOS for a transition metal, illustrating the location of the d-band centre.

## The Wilke function

The Wilke function,  $w^N(\mathbf{r})$ , is defined as

$$w^N(\mathbf{r}) = \frac{1}{k_{\text{B}}^2 T_{\text{el}}} \left( \frac{\partial \rho(\mathbf{r})}{\partial T_{\text{el}}} \right)_{v(\mathbf{r}), N} \quad (1.8)$$

where  $T_{\text{el}}$  is the electron temperature,  $\rho(\mathbf{r})$  is the local electron density,  $v(\mathbf{r})$  is the local potential and  $N$  is the number of electrons.<sup>53</sup> The advantages of the Wilke function include the fact that  $w^N(\mathbf{r})$  is defined with respect to a fixed number of electrons. This is more computationally advantageous than the HSAB approach (described in Section 1.6.2) which requires properties to be calculated for different number of electrons. However, the Wilke function has not been much calculated, in comparison to the d-band centre which is very frequently used. More importantly, the Wilke function can only be used for metals, which makes it less useful as a reactivity index.

## The local electron attachment energy

The local electron attachment energy was proposed by Stenlid and co-workers<sup>54</sup> as a measure of the accessibility of states above the Fermi level. If the local electron attachment energy is high above the Fermi level, this will mean that the lowest unoccupied state is not easily accessed at that location, and a reaction is less likely. In comparison, if the electron attachment energy is close to the Fermi level then the lowest unoccupied state is close in energy to the Fermi level and a reaction is likely. This local reactivity index is, like the Wilke function and the d-band centre, restricted to metals only. This is because it is based on theory related specifically to metals rather than on reactivity more generally. As mentioned above, there is a unifying theory for understanding reactivity called hard and soft acids and bases (HSAB). This is the theoretical basis for various reactivity indices, which will now be discussed.

## 1.6.2 Local reactivity indices based on HSAB

### The Fukui function

Within the HSAB framework outlined in Section 1.5.1 the Fukui function,  $f(\mathbf{r})$ , was defined by Parr and Yang in 1984 as

$$f(\mathbf{r}) = \left( \frac{\partial \rho(\mathbf{r})}{\partial N} \right)_{v(\mathbf{r})} \quad (1.9)$$

where  $\rho(\mathbf{r})$  is the local electron density,  $N$  is the number of electrons and  $v(\mathbf{r})$  is the local external potential.<sup>40</sup> The integral of the Fukui function over a molecule is

$$\int f(\mathbf{r}) d\mathbf{r}_{\text{molecule}} = 1 \quad (1.10)$$

where  $d\mathbf{r}_{\text{molecule}}$  is the volume element.<sup>40</sup>

The Fukui function is easy to calculate for molecules, nanoparticles and metal surfaces.<sup>38</sup> In addition the Fukui function can be experimentally determined via STM measurements.<sup>55</sup> However, the Fukui function is a measure of the relative distribution of reactivity over a surface rather than an absolute measure of reactivity. Therefore the Fukui function cannot be used for inter-molecular comparisons or comparisons between catalytic surfaces.

### Condensation of reactivity indices

Expressions such as Eqn. 1.9 yield a local reactivity index which needs to be visualised in three dimensions. This is relatively labour intensive and requires a careful choice of presentation method, e.g. isosurface threshold. Condensation methods have therefore been developed by Yang and Mortier for use in conceptual DFT.<sup>46</sup> These methods yield greater chemical insight into reactivity at atomic sites. The method involves an atomic rendering of the Fukui function within a molecule. This allows the spatial variation of the Fukui function within the molecule to be captured in a coarse-grained way. This atomic rendering of reactivity is often more useful to experimentalists than local indices. The condensed Fukui function can be used to make predictions,

for example at which atom a reaction may occur. Yang and Mortier<sup>46</sup> developed a finite-difference approximation to calculate a condensed nucleophilic Fukui function for an atom or molecule labelled  $i$ ,

$$(f_i)^+ = q_i(N + 1) - q_i(N) \quad (1.11)$$

where  $q_i(N)$  and  $q_i(N+1)$  are the numbers of electrons in the neutral molecule and anionic form respectively. The same authors also developed a corresponding expression for the condensed electrophilic Fukui function

$$(f_i)^- = q_i(N) - q_i(N - 1) \quad (1.12)$$

where  $q_i(N + 1)$ ,  $q_i(N - 1)$  and  $q_i(N)$  were obtained by a Mulliken analysis using gross charges.

### The dual descriptor

Another reactivity index which has been developed within the framework of conceptual DFT is the dual descriptor<sup>56</sup>

$$\Delta f(\mathbf{r}, N) = \left( \frac{\partial^2 \rho(\mathbf{r}, N)}{\partial N^2} \right)_{v(\mathbf{r})} \quad (1.13)$$

This has been proposed as a predictor of electrophilicity (positive  $\Delta f$ ) and nucleophilicity (negative  $\Delta f$ ) for regions within molecules.<sup>56</sup> This formulation of the dual descriptor has been used to explain the reactivity of carbocations and to predict the formation of halogen bonds.<sup>57</sup>

### The local softness

The local softness,  $s(\mathbf{r})$ , is defined as

$$s(\mathbf{r}) = \left( \frac{\partial \rho(\mathbf{r})}{\partial \mu} \right)_{v(\mathbf{r}), T} \quad (1.14)$$

where  $\rho(\mathbf{r})$  is the local electron density at a position  $\mathbf{r}$  and  $\mu$  is the chemical potential. The external potential,  $v(\mathbf{r})$ , and the temperature  $T$  must be kept constant. The local softness is a reactivity index closely related to the Fukui function and Wilke function as it too involves a partial derivative of the local electron density.<sup>38</sup>

The local softness and Fukui function are related by the global softness

$$s(\mathbf{r}) = Sf(\mathbf{r}) \quad (1.15)$$

due to the normalisation of the Fukui function as shown in Eqn. 1.10.<sup>43</sup> Therefore the local softness can be considered to be the global softness weighted by the distribution of the Fukui function.<sup>38</sup>

The local softness can be integrated over space to find the global softness,  $S$ , of an atom, molecule or site.

$$S = \int s(\mathbf{r})d\mathbf{r} \quad (1.16)$$

In order to find the softness of an atom  $i$ , Eqn. 1.16 can be applied over a restricted volume corresponding to that individual atom. The atomic softness,  $s_i$ , is defined as

$$s_i = \int_i s(\mathbf{r})d\mathbf{r} \quad (1.17)$$

where the integral is over the volume associated with atom  $i$ .

The local softness is an extremely useful reactivity index as, unlike the Fukui function,  $s(\mathbf{r})$  is an absolute measure of reactivity. Therefore  $s(\mathbf{r})$  can be used to compare the reactivity of sites within different molecules or nanoparticles with a different value of global softness  $S$ . In metal surfaces, for example, the local softness can be used to compare the reactivity of a step-edge site with a terrace site. As comparing the active sites in different surfaces is very useful for designing catalysts, this makes  $s(\mathbf{r})$  very well suited for this purpose.

Likewise the local softness has advantages over the Wilke function and the d-band centre as it is not restricted to metal atoms. In particular, the local softness can be calculated for adsorbates on metal surfaces. In addition, unlike the Wilke function, the local softness can be calculated for systems such as MOFs where no bulk conducting metal framework is present.

## 1.7 Calculating the local softness

As can be seen above, the local softness is a particularly valuable reactivity index which lends physical insight to the reactivity of surfaces.  $s(\mathbf{r})$  can be used for absolute comparisons and to find the reactivity of adsorbates and metal surface sites. However, a disadvantage of the local softness is that at present, it is difficult to calculate the local softness in the exact form of Eqn. 1.14 for extended systems, e.g. surfaces or bulk materials. This is because extended systems require periodic boundary conditions. It is difficult to vary the chemical potential without changing the charge, and therefore (in periodic boundary conditions) the external potential.

As discussed in the previous section, Yang and Mortier<sup>46</sup> proposed a scheme where some local information can be gained of the reactivity within a molecule or nanoparticle, while retaining the convenience of the approximations used for the global measures in Eqns. 1.6 and 1.7. These are the so-called condensed local reactivity indices, though in reality they are closer to being a global measure for a given atom in a molecule or nanoparticle than to a local reactivity index. The Fukui function is discontinuous for molecules and nanoparticles, so there are two functions; the nucleophilic Fukui function defined in Eqn. 1.11 and the electrophilic descriptor, 1.12. There is a similar expression for the condensed local softness of an atom  $i$ ,

$$s_i^\alpha = f_i^\alpha S^\alpha \quad (1.18)$$

where  $\alpha$  may be  $+$  or  $-$  for the nucleophilic and electrophilic softness, respectively. The vast majority of studies of the local softness use this method.<sup>58</sup> In particular this method has been used to predict the reactivity of transition-

metal nanoparticles, both with and without CO adsorbed.<sup>44</sup> This allowed the reactivity of different sites on different facets to be compared and the electronic effects of an adsorbate molecule to be studied.<sup>44</sup> However, it is important to note that the finite-difference approach of Yang and Mortier is a relatively crude approximation.<sup>58</sup> In addition it is necessary to estimate the global softness using the finite-difference method of Eqn. 1.7. This is a problem for bulk metals as the global softness is then not defined, as discussed in Section 1.5.1.

## 1.8 Approximating the local softness: The Fermi softness

Recent work by Huang and co-workers<sup>59</sup> provided a method to estimate the local softness. This was by calculating a reactivity index which they named the Fermi softness. This quantity can be defined as either a local or a global function. The global Fermi softness was defined by Huang et al as

$$s_{\text{F}} = \int g(E)w(E)dE = - \int g(E)f'(E - E_{\text{F}})dE \quad (1.19)$$

where  $g(E)$  is the density of states and  $w(E)$  is a weighting function defined as the derivative of the Fermi-Dirac function,  $f(E - E_{\text{F}})$ , with respect to energy  $E$ . Equation 1.19 is taken from the paper by Huang and co-workers.<sup>59</sup> Huang and co-workers expressed the global chemical softness in terms of the DOS. Their result is analogous to Eqn. 1.4 in Section 1.5.1. This defines the global softness as

$$s = \left( \frac{\partial N}{\partial \mu} \right)_{v(\mathbf{r}),T} = \frac{\partial}{\partial E_{\text{F}}} \left[ \int g(E)f(E - E_{\text{F}})dE \right] \quad (1.20)$$

where the other quantities are defined as above. In the expression on the right hand side of Eqn. 1.20 the order of differentiation and integration can be swapped. It is then possible to use the product rule to expand out the

right hand side of the equation:

$$s = \int \frac{\partial}{\partial E_F} [g(E)f(E-E_F)] dE = \int \left[ \frac{\partial g(E)}{\partial E_F} f(E-E_F) + g(E) \frac{\partial f(E-E_F)}{\partial E_F} \right] dE \quad (1.21)$$

where it can be recognised that if  $g(E)$  were constant with respect to changes in the Fermi level then the first term in the expression in square brackets will be zero. The second term can be simplified by noting that the derivative of the Fermi-Dirac function with respect to the Fermi level is equal to the derivative with respect to energy multiplied by minus one. Therefore, in the case that the DOS does not depend on the Fermi level, Eqn. 1.21 can be simplified to result in the right hand side of Eqn. 1.19. In other words, the Fermi softness is equal to the global softness where the DOS is independent of the Fermi level. This result simplifies the calculation of the local softness considerably, as all that is needed is to calculate the DOS for a neutrally charged calculation and multiply by a weighting function. The authors also suggest a local reactivity index, the local Fermi softness, based on Eqn. 1.19 but replacing the DOS with the Local Density of States (LDOS). This equation is an approximation to the local softness based on the assumption that the LDOS will be independent of the Fermi level.

Another way of considering the assumption that the DOS will not vary with Fermi level is to consider the situation of applying a fictitious potential  $v(\mathbf{r})$  in order to stop the electrons from moving in response to an increase in the number of electrons as the Fermi level increases. This would therefore break the requirement for the external electric potential to remain constant when increasing the chemical potential, as noted earlier in Eqn. 1.19. This suggests that there will be a problem with the approach used to approximate the softness based on the Fermi softness. In fact, it is certainly the case that the DOS does vary with a change in the Fermi level, as will be discussed later in this work concerning Fig. 3.21. To conclude, the Fermi softness has the advantage of being easy to calculate, but it is only an approximate measure of the softness. It would be helpful to have a method of calculating

the local softness more exactly, provided that this can be done for constant potential.

## 1.9 New method of calculating local softness

As discussed earlier in Section 1.7 the local softness has so far only been calculated for molecules and nanoparticles, rather than for surfaces. This is due to inherent problems with the method set out above in Section 1.7, of working via the global softness which is undefined for metal surfaces. An alternative way of thinking of this is that metals, as conductors, have an infinitely small band gap.<sup>44</sup> It is therefore desirable to find a new method of calculating the local softness of surfaces.

An obvious way to calculate local softness is to directly calculate the local softness via Eqn. 1.14. In particular, the local softness can be calculated by splitting the partial derivative using the chain rule:

$$s(\mathbf{r}) = \left( \frac{\partial \rho(\mathbf{r})}{\partial \mu} \right)_{v(\mathbf{r}),T} = \frac{(\partial \rho(\mathbf{r})/\partial \sigma)_{v(\mathbf{r}),T}}{(\partial \mu/\partial \sigma)_{v(\mathbf{r}),T}} \quad (1.22)$$

where  $\rho(\mathbf{r})$ ,  $\mu$  and  $v(\mathbf{r})$  are defined as in Section 1.6.  $\sigma$  is the surface charge,

$$\sigma = Q/A \quad (1.23)$$

where  $Q$  is the charge in the supercell and  $A$  is the total area (of both surfaces in a slab simulation supercell). The numerator of local softness is, like the Fukui function, a relative measure of reactivity within a surface. The name relative local softness has been suggested<sup>60</sup> for this quantity,  $s_{\text{rel}}(\mathbf{r})$ , defined as

$$s_{\text{rel}}(\mathbf{r}) = \left( \frac{\partial \rho(\mathbf{r})}{\partial \sigma} \right)_{v(\mathbf{r}),T} = \frac{d\rho(\mathbf{r})}{d\sigma} \quad (1.24)$$

which can be expected to be independent of any external potential. The temperature can be expected to be constant for DFT calculations, therefore the right hand equality of Eqn. 1.24 should hold.  $s_{\text{rel}}(\mathbf{r})$  can be expected to

vary within three-dimensional space, but to be independent of the external potential applied by a plane-wave code. In comparison, the denominator of local softness can be expected to be a function of the external potential when calculated by a plane-wave code with periodic boundary conditions. This is because the practical method of changing the surface charge necessarily involves adding or subtracting electrons. However, this will certainly change the external potential.

$$\left(\frac{\partial\mu}{\partial\sigma}\right)_{v(\mathbf{r}),T} \neq \frac{d\mu}{d\sigma} \quad (1.25)$$

In this case, a plane-wave code imposes an external potential to prevent divergence of energy in charged cells with periodic boundary conditions. This potential is not constant with respect to changes in simulation supercell geometry.<sup>61,62</sup> The quantity on the right hand side of Eqn. 1.25 is the quantity that would be calculated naively by a plane-wave code such as CASTEP and can certainly be expected to differ from the true value of the denominator of local softness. This problem must be solved in order to calculate the local softness.

## 1.10 Summary of this thesis

As discussed above, it would be desirable to calculate  $s(\mathbf{r})$  for metal surfaces in order to gain physical insight into catalyst reactivity. This requires the calculation of the denominator of local softness in a way that excludes the dependence on the external potential imposed by plane-wave codes for charged systems. However, there are various problems which need to be overcome in order to do this. In Chapter 2, a method is presented by which the true denominator of  $s(\mathbf{r})$  can be calculated.

This requires solving a problem with convergence by correcting the chemical potential. The results obtained using this correction are discussed in Chapter 3. Isosurfaces and colourplots of the local softness for eighteen metal surfaces are analysed in Chapter 4. The atomic softness is calculated and shown to correlate with CO adsorption energy in Chapter 5. The local and

atomic softness are used to explain directing effects in aromatic adsorbates on Pt{111} in Chapter 6. Chapter 7 discusses the potential applications for solving the problem of selectivity in heterogeneous catalysis.

# Chapter 2

## Methodology

In this chapter, the methods used for this thesis will be discussed. The general concepts of electronic structure theory and its application within plane-wave codes such as CASTEP will be explained in Sections 2.1-2.4. Sections 2.5-2.10 are concerned with the specific use of CASTEP in this work to calculate the chemical softness for particular systems.

### 2.1 Electronic structure theory

The postulates of quantum mechanics were developed in the 1920's by Heisenberg, Schrödinger and others. They provide a mathematical approach for modelling chemical systems.<sup>63-65</sup>

Two postulates of quantum mechanics are particularly relevant to this work. The first of these defines a wavefunction that (amongst other things) can be used to model chemical behaviour mathematically. A system of  $n$  particles labelled with an index  $i$  at positions  $\mathbf{r}_i$  at time  $t$  can be mathematically modelled using the time-dependent wavefunction,  $\Psi(\mathbf{r}_1, \mathbf{r}_2, \dots, \mathbf{r}_n, t)$ <sup>66</sup>

The second postulate is the time-dependent Schrödinger equation. This expresses how the wavefunction  $\Psi$  changes with time.<sup>66</sup>

$$i\hbar \frac{\partial \Psi}{\partial t} = \hat{H} \Psi \quad (2.1)$$

In Eqn. 2.1,  $\hbar$  is the reduced Planck's constant and  $\hat{H}$  is the Hamiltonian operator, which corresponds with the total energy of the system. The Hamiltonian can be expressed as

$$\hat{H} = \hat{T} + \hat{V} \quad (2.2)$$

where  $\hat{T}$  is the kinetic energy operator and  $\hat{V}$  is the potential energy operator.<sup>66</sup>

For cases where the potential energy operator  $\hat{V}$  from Eqn. 2.2 is independent of time, the differential Eqn. 2.1 can be simplified. Valid wavefunctions will then be the product of a time-independent wavefunction  $\psi$  and a time-dependent complex exponential

$$\Psi = \psi e^{-iEt/\hbar} \quad (2.3)$$

where the time-independent wavefunction,  $\psi$ , is a function of spatial coordinates alone.<sup>66</sup>  $E$  is the energy eigenvalue, which can be calculated using the time-independent Schrödinger equation:

$$\hat{H}\psi = E\psi \quad (2.4)$$

Equation 2.4 provides a way to calculate the energy of any system of electrons and nuclei. This is useful as many important physical properties can be calculated using the energy.<sup>67</sup>

## 2.2 Approximations often used for chemistry

There are many problems in chemistry that would benefit from the electronic-structure-theory approach. In principle, any chemical system can be modelled theoretically, but the resulting equations are too difficult to solve for all but the simplest of systems.<sup>68</sup> For example, even the smallest molecule,  $\text{H}_2^+$ , has three particles, which means the Schrödinger equation cannot be solved analytically.<sup>66</sup> Various approximations must be made to apply Electronic Structure theory to chemically relevant systems.

### 2.2.1 Born-Oppenheimer approximation

One of the most fundamental approximations is the Born-Oppenheimer approach. This involves simplifying the treatment of the interaction between electrons and nuclei. This approximation is needed to solve the problem mentioned above in applying electronic structure theory to molecules such as  $\text{H}_2^+$ . The Born-Oppenheimer approach is based on the observation that electrons have much smaller mass than nuclei (electron mass is 0.000549 amu whereas the lightest nucleus weighs 1.01 amu).<sup>66</sup> This factor of three orders of magnitude in the masses corresponds to a large difference in the speed of movement of electrons and nuclei.<sup>69</sup>

Based on this large difference, it may be assumed that electron movement is effectively instantaneous relative to the timescale of nuclear movement. In most cases this is a reasonable approximation, though there are cases where the Born-Oppenheimer approach cannot be used. This is particularly likely for light atoms such as hydrogen. For example, the Born-Oppenheimer approach fails to correctly model the diffusion of atomic hydrogen in palladium.<sup>70</sup> Nevertheless, for the vast majority of systems, the Born-Oppenheimer approximation gives accurate results.<sup>66</sup>

The Born-Oppenheimer approach involves calculating the electron energy for a variety of fixed nuclear coordinates. This is then used to construct a potential energy surface. The nuclear coordinates of stable structures correspond to minima in the potential energy surface.<sup>66</sup> An example of a typical

Born-Oppenheimer procedure is as follows:

1. Choose a set of nuclear coordinates.
2. Minimise the energy over electron degrees of freedom while keeping nuclear coordinates fixed.
3. Calculate forces acting on the nuclei (based on the results from step 2) and use these to find new lower-energy nuclear coordinates. For more detail see Section 2.4.4.
4. Repeat steps 2-3 until the coordinates that minimise the energy are obtained. Depending on the starting coordinates and minimisation scheme used, this may be a local minimum on the potential energy landscape, rather than the global minimum.<sup>71</sup>.

The electronic wavefunction  $\psi(\mathbf{r}; \mathbf{R})$  can be defined as depending directly on electron positions  $\mathbf{r}$  and only parametrically on nuclear coordinates  $\mathbf{R}$ . The corresponding electronic Schrödinger equation,

$$\hat{H}\psi(\mathbf{r}; \mathbf{R}) = E(\mathbf{R})\psi(\mathbf{r}; \mathbf{R}) \quad (2.5)$$

can be solved to find the electronic energy  $E(\mathbf{R})$  for a fixed set of nuclear positions  $\mathbf{R}$ .<sup>66</sup>

## 2.3 Density functional theory

Density Functional Theory (DFT) is an electronic structure method for calculating the electronic energy. The theoretical justification for DFT as an *ab initio* approach was developed by Hohenberg and Kohn.<sup>72,73</sup>

### 2.3.1 Hohenberg-Kohn theorems

#### Hohenberg-Kohn existence theorem

Hohenberg and Kohn showed that two systems that have the same ground state electron density,  $\rho(\mathbf{r})$ , must also have the same external potential  $v(\mathbf{r})$ .<sup>72,73</sup> Hohenberg and Kohn used this result to show that in principle all ground-state properties can be found from  $\rho(\mathbf{r})$ .<sup>66</sup> In particular it follows that the ground-state energy  $E$  is a functional of  $\rho(\mathbf{r})$ <sup>72</sup> and the energy can therefore be expressed as

$$E = E[\rho] = T[\rho] + V[\rho] \quad (2.6)$$

where  $E[\rho]$  is the energy functional, and  $T[\rho]$  and  $V[\rho]$  are the kinetic and potential energy functionals. A functional, such as  $E[\rho]$ ,  $T[\rho]$  or  $V[\rho]$ , acts on a function to produce a number.<sup>66</sup> Functionals have special mathematical properties, as they have contributions from the whole range of values of a function such as  $\rho(\mathbf{r})$ .<sup>66</sup>

The potential energy functional,  $V[\rho]$ , can be separated into two components from nuclear and electronic interactions, resulting in the following expression for the energy functional

$$E[\rho] = T[\rho] + V_{ee}[\rho] + V_{\text{ext}}[\rho] \quad (2.7)$$

where  $V_{ee}[\rho]$  is the electron-electron interaction energy and  $V_{\text{ext}}[\rho]$  is the total external potential, giving the energy of interaction between electrons and nuclei.<sup>66</sup> The total external potential can be calculated by integrating the product of electron density and local external potential  $v(\mathbf{r})$  over all space.

$$V_{\text{ext}}[\rho] = \int \rho(\mathbf{r})v(\mathbf{r})d\mathbf{r} \quad (2.8)$$

## Hohenberg-Kohn variational theorem

Hohenberg and Kohn also showed that the variational principle can be applied to iteratively find the ground-state density  $\rho$  from considering a set of valid trial densities,  $\{\tilde{\rho}\}$ . This requires an expression for the energy functional  $E[\rho]$ . Valid  $\tilde{\rho}$  must contain the correct number of electrons:

$$\int \tilde{\rho}(\mathbf{r})d\mathbf{r} = N \quad (2.9)$$

Among trial densities  $\tilde{\rho}$  that conform to Eqn. 2.9, the correct ground-state electron density will minimise the energy.

$$E[\tilde{\rho}] \geq E[\rho] \quad (2.10)$$

Equation 2.10 means that the energy is minimised for the ground-state electron density. At the minimum energy the derivative will be zero. This result can be used in the following differential equation,

$$\delta E[\rho] - \mu \cdot \delta \left[ \int \rho(\mathbf{r})d\mathbf{r} - N \right] = 0 \quad (2.11)$$

where  $\mu$  is the chemical potential, which is also the Lagrange multiplier associated with condition 2.9.<sup>72,74</sup>

There is a corresponding Euler-Lagrange expression for the chemical potential,

$$\mu = v(\mathbf{r}) + \frac{\delta T[\rho]}{\delta \rho(\mathbf{r})} + \frac{\delta V_{ee}[\rho]}{\delta \rho(\mathbf{r})} \quad (2.12)$$

where the second and third terms are functional derivatives.<sup>74</sup>

Equations 2.10-2.12 provide a way to model ground-state atoms or molecules, given an initial guess at the electron density and the correct energy functional. This approach confers a great reduction in computational cost over

wavefunction methods. The  $N$ -electron wavefunction is a  $3N$ -dimensional function whereas  $\rho(\mathbf{r})$  is only a local function in three dimensions. However, an analytic expression for  $E[\rho]$  is required, and this is not known. This problem makes it difficult to make use of Eqn. 2.6. A potential way forward would be to find a way of approximating  $E[\rho]$ . Equation 2.10 would then provide a way of finding the best density for a given energy functional.<sup>66</sup>

### 2.3.2 Thomas-Fermi theory

An early contribution to the search for approximate energy functionals was made by Llewellyn Thomas and Enrico Fermi in 1927 and 1928.<sup>75,76</sup> They used Eqn. 2.7 and made several approximations to result in more easily-calculated terms. They substituted the kinetic energy of a homogeneous electron gas for  $T[\rho]$  and used the classical Hartree model for  $V_{ee}[\rho]$ .

$$E_{TF}[\rho] = T_{\text{hom}}[\rho] + V_{\text{Hart}}[\rho] + V_{\text{ext}}[\rho] \quad (2.13)$$

These are relatively drastic approximations, especially to the kinetic energy.<sup>77</sup> Also, Eqn. 2.13 neglects the effects of electron correlation and exchange.<sup>66</sup> The application of Thomas-Fermi theory to metal surfaces can be considered using a jellium model. The jellium or free electron model is a simple way to approximate the behaviour of metals in an extended solid and at a surface.<sup>78-80</sup>

In the jellium model, only the electrostatic behaviour of the ion cores is considered, and this only in a spatially averaged way. The positive charge from ion cores is treated as constant in an extended solid and as a step function for a solid that is extended in two dimensions and with a surface in the third dimension.<sup>79</sup> Several researchers have applied the Thomas-Fermi approximation for the jellium model of a metal surface.<sup>79,81</sup> For a semi-infinite slab, there would be negative surface energies and the work function would be zero.<sup>79</sup>

The vanishing work function means that there would be no difference in

energy between an electron at the Fermi level and an electron in the vacuum. This means there would be no energy barrier to remove the highest energy electron from the metal slab. Negative surface energy implies it would always be energetically favourable to divide the jellium solid up into smaller and smaller pieces. This is equivalent to Teller’s non-binding theorem for atoms in molecules, which states that in the Thomas-Fermi approximation a molecule would not be stable but would dissociate into its constituent atoms.<sup>82</sup>

This is a catastrophic failure of the Thomas-Fermi method to model basic chemical behaviour. This failure shows that both kinetic energy and exchange and correlation effects are important to model electron binding properly. A more accurate energy functional is needed in order to correctly model chemistry. In particular, more accuracy is needed to calculate the kinetic energy, as the failures of Thomas-Fermi theory show that the effect of errors in  $T[\rho]$  is considerable. In order to do this, a different approach is needed. This was developed several decades later by Kohn and Sham.

### 2.3.3 Kohn-Sham equations

The Kohn-Sham equations provide a way to formulate an approximate expression for the energy functional.<sup>73</sup> Kohn and Sham re-expressed Eqn. 2.7 in terms of the energy of a more computationally-tractable reference system. They added a small, approximate correction term to account for differences between the real system and the reference system, including exchange and correlation effects. This approximate inclusion of exchange and correlation is an improvement compared with Thomas-Fermi theory, which did not consider them at all.

Unlike the Thomas-Fermi model, the Kohn-Sham approach uses an exact expression for the kinetic energy. However, there were still challenges in finding the correct functional for the potential in Eqn. 2.6. Finding the exact  $V[\rho]$  functional was too theoretically and computationally difficult. Instead, Kohn and Sham considered a reference system of non-interacting electrons.<sup>73</sup> In this system the potential  $v_{\text{ref}}(\mathbf{r})$  is chosen to make sure that the density of

the reference system  $\rho_{\text{ref}}(\mathbf{r})$  is the same as the ground-state electron density of a system of interest  $\rho(\mathbf{r})$ .

The Hamiltonian of the reference system,  $\hat{H}_{\text{ref}}$ , can be expressed as

$$\hat{H}_{\text{ref}} = \sum_{i=1}^{N_e} \hat{H}_i^{\text{KS}} \quad (2.14)$$

where  $N_e$  is the number of electrons. The right hand side of Eqn. 2.14 is a sum over one-electron Kohn-Sham Hamiltonians  $\hat{H}_i^{\text{KS}}$

$$\hat{H}_i^{\text{KS}} = -\frac{\hbar^2}{2m_e} \nabla_i^2 + v_{\text{ref}}(\mathbf{r}_i) \quad (2.15)$$

where  $\nabla_i^2$  is the Laplacian operator for electron  $i$ .<sup>66</sup> This approach simplifies the calculation of energy considerably. The energy functional can therefore be expressed as

$$E[\rho] = T_s[\rho] + J[\rho] + V_{\text{ext}}[\rho] + [(T[\rho] - T_s[\rho]) + (V_{\text{ee}}[\rho] - J[\rho])] \quad (2.16)$$

Where  $T_s[\rho]$  is the non-interacting kinetic energy,  $J[\rho]$  is the coulomb potential and the quantity in square brackets is a correction term to take into account the effects of electron correlation and exchange. This correction term is needed to find the energy of the real system from that of the non-interacting reference system. It is called the exchange-correlation functional,

$$E_{\text{xc}}[\rho] = (T[\rho] - T_s[\rho]) + (V_{\text{ee}}[\rho] - J[\rho]) \quad (2.17)$$

To summarise, the Kohn-Sham approach describes the complex effects of electron exchange and correlation using a single functional,  $E_{\text{xc}}[\rho]$ , which makes a small but significant contribution to the overall energy.<sup>83</sup>

The problem is that there is no understanding of what form this functional

will take. A comparison with wavefunction methods may help to illustrate why this is such a significant issue. In wavefunction methods, the mathematical form of the exact Hamiltonian is well defined and is known. This means that different levels of approximations can be compared with that of the exact expression. Knowing the form of the exact Hamiltonian allows for systematic improvement of approximations.<sup>84</sup> In comparison, in DFT the form of  $E_{xc}[\rho]$  is not known.<sup>74</sup> Therefore it is hard to know where to start and from an initial guess, it is hard to systematically improve models for  $E_{xc}[\rho]$ .<sup>84</sup> However, not all is dark. There are a few things that can be predicted about how  $E_{xc}[\rho]$  should behave.

Electrons are charged particles that repel each other and therefore instantaneously are less likely to be found near to each other (Coulomb correlation). Electrons are fermions and therefore two electrons of the same spin cannot be in the same location instantaneously (exchange or Fermi correlation). These dynamic interactions mean that around the instantaneous position of each electron in a system there will be an area of depleted electron density.<sup>84</sup> These ‘exchange-correlation holes’ have a particular set of physical properties. In particular, the exchange or ‘Fermi’ hole will be negative everywhere and integrate over all space to  $-1$ . This sum rule is useful for checking if a functional is modelling holes well.

### 2.3.4 Local density approximation

The Local Density Approximation (LDA) is a way of tackling the problem of exchange and correlation by comparison with the uniform electron gas. This way of approximating  $E_{xc}$  involves considering a simple system for which the exchange energy can be calculated exactly. This approach was used by Kohn and Sham in 1965 to find an expression for the exchange-correlation energy of the uniform electron gas,<sup>73</sup>

$$E_{xc}^{LDA} = \int \epsilon_{xc}(\rho)\rho(\mathbf{r})d\mathbf{r} \quad (2.18)$$

where  $\epsilon_{xc}$  is the exchange-correlation energy per particle of the uniform electron gas of density  $\rho$ . This can be expressed as

$$\epsilon_{xc} = \epsilon_c + \epsilon_x \quad (2.19)$$

where  $\epsilon_c$  and  $\epsilon_x$  are the correlation and exchange contributions. For the uniform electron gas, there is an exact expression for the exchange term,

$$\epsilon_x = -\frac{3}{4} \left( \frac{3}{\pi} \right)^{\frac{1}{3}} \rho(\mathbf{r})^{\frac{1}{3}} \quad (2.20)$$

By contrast there is no known analytic expression for the correlation of the uniform electron gas.<sup>84</sup> However, it is possible to fit an approximate expression to data from highly accurate Monte Carlo calculations performed by Ceperley and Alder in 1980.<sup>85</sup> In order to do this it is helpful to re-express the density in terms of the local Seitz radius,

$$r_s = \left( \frac{3}{4\pi\rho} \right)^{\frac{1}{3}} \quad (2.21)$$

which is the radius of a sphere enclosing a volume that, for a given density, would contain exactly one electron. Perdew and Wang used the numerical values from Ceperley and Alder to derive the following expression for the correlation energy per particle as a function of the relative spin polarisation  $\zeta = (\rho_\alpha - \rho_\beta)/\rho$  and the local Seitz radius,

$$\epsilon_c(r_s, \zeta) = \epsilon_c(r_s, 0) + \alpha_c(r_s) \frac{f(\zeta)}{f''(0)} (1 - \zeta^4) + [\epsilon_c(r_s, 1) - \epsilon_c(r_s, 0)] f(\zeta) \zeta^4 \quad (2.22)$$

$$f(\zeta) = \frac{[(1 + \zeta)^{4/3} + (1 - \zeta)^{4/3} - 2]}{2^{4/3} - 2} \quad (2.23)$$

where  $\alpha_c(r_s)$  is the spin stiffness  $\partial^2 \epsilon_c(r_s, \zeta = 0) / \delta \zeta^2$ .<sup>86</sup> The exchange-correlation

energy per particle can be found by substituting Eqns. 2.20 and 2.22 into Eqn. 2.19. The key step in this approach is to compute  $\epsilon_{xc}$  for each infinitesimally-small portion of space as if it were part of a uniform electron gas of that density. These individual contributions are added up to form  $E_{xc}$  using Eqn. 2.18. This is a good approximation in the limit of a slowly-varying density.<sup>74</sup> However, for atoms and molecules the electron density varies sharply near the nuclei. Therefore an approach like LDA, which approximates  $E_{xc}$  based on only the local density at each point, seems likely to be inaccurate for these systems.<sup>84</sup>

### 2.3.5 Generalised gradient approximation

In order to go beyond the local density approximation, one intuitive approach is to consider the LDA as the first step in a Taylor-series expansion in terms of the density. For example, this allows the effects of inhomogeneity to be included by considering  $E_{xc}$  to be a function not only of the local density but of its gradient  $\nabla\rho(\mathbf{r})$ .

$$E_{xc} = \int f(\rho(\mathbf{r}), \nabla\rho(\mathbf{r})) d\mathbf{r} \quad (2.24)$$

Rather than using a homogeneous electron gas as a model, this involves comparison with a slightly inhomogeneous electron gas.<sup>84</sup> This model system of slowly-varying density can be expected to be at least somewhat more realistic for inhomogeneous real systems of atoms and molecules. However, rather counter-intuitively, the addition of successive terms in a gradient expansion generally gives worse results than LDA.<sup>74</sup> This is partly because the LDA model of exchange-correlation holes are relatively close to the holes found in real systems.<sup>84</sup>

The Generalised Gradient Approximation (GGA) is a modification of this approach where the functional is not a simple Taylor expansion in terms of the density, but is also constrained to follow certain rules. These rules enforce particular conditions for the exchange-correlation holes generated

by the GGA method. This should mean GGA exchange and correlation functionals will model real systems more accurately.<sup>84</sup>

GGA functionals often model exchange and correlation separately. A commonly-used GGA exchange functional is the PBE functional,

$$E_x^{\text{PBE}} = E_x^{\text{LDA}} - C_D \sum_{\sigma} \int \rho_{\sigma}^{4/3} \left( \kappa - \frac{\kappa}{1 + \frac{\mu s^2}{\kappa}} \right) d\mathbf{r} \quad (2.25)$$

where  $s$  is a dimensionless reduced density,  $C_D$  is the Dirac exchange constant and  $\kappa$  and  $\mu$  are constants chosen to maintain certain performance criteria.<sup>87</sup> The authors focussed on those known features of the exact functional that would have the largest impact on the energy. This includes accurate modelling of systems with density that is close to uniform, which is important for correct treatment of metals.<sup>87</sup> Also, they made sure the functional would satisfy the Lieb-Oxford bound.<sup>87</sup>

The same authors also developed a correlation functional,

$$E_c^{\text{PBE}} = \int \rho(\mathbf{r}) [\epsilon_c^{\text{unif}}(r_s, \zeta) + H(r_s, \zeta, t)] d\mathbf{r} \quad (2.26)$$

where  $\epsilon_c^{\text{unif}}$  is the uniform electron gas expression found in Eqn. 2.22,  $t$  is a dimensionless density gradient and  $H$  is a fitted analytic function with parameters chosen to satisfy energetically important correlation behaviour, especially the condition that the integral of the correlation functional over all space should be zero, which means that for rapidly-varying densities  $t \rightarrow \infty$ , correlation should vanish.<sup>87</sup> The PBE functional performs well for a wide variety of systems and is one of the most commonly-used functionals, especially for materials applications.<sup>83</sup>

### 2.3.6 Costs and accuracy of DFT

The computational cost of DFT generally scales as  $N^3$ , where  $N$  is the number of electrons.<sup>38</sup> This represents a significant advantage over wavefunc-

tion methods. For example CCSD(T), which is often regarded as the gold-standard technique, scales with the sixth order of system size.<sup>88,89</sup> DFT has the potential to be exact, provided that the analytical form of the exchange-correlation functional is known. However, this is not currently possible except for the simplest of cases.<sup>90</sup>

## 2.4 Plane-wave pseudopotential method

In Section 2.3 it was established that DFT can be used along with an approximate exchange-correlation functional to model the behaviour of the electrons in chemical systems. There are several other related approximations and techniques that are useful. These include periodic boundary conditions, plane waves, pseudopotentials, fast-Fourier transforms (FFT's) and energy-minimisation algorithms.<sup>91,92</sup> Periodic boundary conditions allow the treatment of extended solids or surfaces with computational methods, by avoiding the need to simulate an infinite number of particles.

### 2.4.1 Plane waves

A basis set of plane waves can be used to form the one-electron wavefunctions required by Kohn-Sham theory. Any periodic function can be modelled by an infinite set of plane waves. Bloch's theorem can be used to represent the one-electron wavefunctions as a product of a plane wave, which represents the long-range part of the wavefunction, and a periodic Bloch function,

$$\psi_{n,\mathbf{k}}(\mathbf{r}) = u_{\mathbf{k}}(\mathbf{r})\exp(i\mathbf{k} \cdot \mathbf{r}) \quad (2.27)$$

Where  $\mathbf{k}$  is the wavevector of a plane wave in reciprocal space and  $u_{\mathbf{k}}(\mathbf{r})$  is a Bloch function defined to have periodic symmetry to match that of the real-space system such that

$$u_{\mathbf{k}}(\mathbf{r}) = u_{\mathbf{k}}(\mathbf{r} + \mathbf{R}) \quad (2.28)$$

where  $\mathbf{R}$  is an arbitrarily chosen real-space lattice vector.

Equation 2.27 is the form of the set of one-electron eigenfunctions that satisfy the symmetry imposed by periodic boundary conditions. There are an infinite number of eigenfunctions specified by their wavevector  $\mathbf{k}$ , which can be used as a quantum number. Each will have a different value of the wavevector  $\mathbf{k}$ . The Bloch factorisation is not unique, which means that for each  $\mathbf{k}$  wavevector there are an infinite number of possible factorisations based on whether the exponential of a general reciprocal lattice vector  $\mathbf{G}_j$  is in the Bloch function or plane-wave part of the Bloch factorisation. The index  $j$  denotes which Brillouin zone the reciprocal lattice vector points into.

The reduced-zone scheme involves choosing to always put this exponential factor in the Bloch function. Therefore the plane-wave part of Eqn. 2.27 will always point within the first Brillouin zone in reciprocal space. However, for each wavevector  $\mathbf{k}$  in the reduced-zone scheme there will be an infinite set of different eigenfunctions. These will differ in their Bloch functions, which will take the form

$$u_{j,\mathbf{k}}(\mathbf{r}) = u_{\mathbf{k}_j}(\mathbf{r})\exp(i\mathbf{G}_j \cdot \mathbf{r}) \quad (2.29)$$

where  $u_{\mathbf{k}_j}(\mathbf{r})$  is the factor of the Bloch function from the alternative factorisation method where the Bloch function is chosen to be as small as possible (the extended-zone scheme). In the reduced-zone scheme,  $j$  is an additional quantum number which specifies the correct Brillouin zone. The lowest energy eigenvalues for a given value of  $\mathbf{k}$  will correspond to Bloch functions where both factors in Eqn. 2.29 have mostly in-phase bonding interactions rather than anti-bonding. For the  $\exp(i\mathbf{G}_j \cdot \mathbf{r})$  factor this will be achieved for zero or small values of  $\mathbf{G}_j$ . Instead of finding all the eigenfunctions (which are infinite), a helpful approach is to note that the eigenfunctions at very nearby regions in reciprocal space will be very similar. Therefore a finite set of grid points in reciprocal space within the first Brillouin zone can be assumed to be representative of the finite region of reciprocal space surrounding them. Electrons can then be allocated to the lowest-energy eigenfunctions up to the

Fermi level. The eigenvalues of occupied eigenfunctions can be added up to find the total energy.

The Bloch functions can be expressed as a Fourier series. This would be possible for any periodic function, but due to the special symmetry of the Bloch function, the basis set of plane waves must be commensurate with the real-space lattice. This means suitable wavevectors for the plane-wave expansion are restricted to the smaller but still infinite set of reciprocal lattice vectors  $\mathbf{G}$ ,

$$u_{j,\mathbf{k}}(\mathbf{r}) = \sum_{\mathbf{G}} A_{j,\mathbf{k}}^{\mathbf{G}} \exp(i\mathbf{G} \cdot \mathbf{r}) \quad (2.30)$$

where  $\{A_{j,\mathbf{k}}^{\mathbf{G}}\}$  are a set of coefficients. Equation 2.30 can be substituted into Eqn. 2.27 to form a new expression for the one-electron wavefunctions,

$$\psi_{n,\mathbf{k}}(\mathbf{r}) = \sum_{\mathbf{G}} A_{j,\mathbf{k}}^{\mathbf{G}} \exp(i(\mathbf{k} + \mathbf{G}) \cdot \mathbf{r}) \quad (2.31)$$

where the sum is over an infinite sum of plane-waves with wavevector equal to reciprocal lattice vectors  $\mathbf{G}$ . In order to make the calculations possible, the plane-wave basis set can be restricted to include only those plane waves with energy below a certain energy cutoff. This will be a good approximation in most cases, although the number of plane waves required for accuracy increases with the highest curvature of the real-space function modelled.<sup>92</sup> Unfortunately, this means that using plane waves to model the core electrons would be very expensive. To avoid this it is helpful to use a pseudopotential to collectively model the nuclei and core electrons as ion cores.<sup>92</sup>

## 2.4.2 Pseudopotentials

Core-electron wavefunctions are difficult to model as they vary sharply, which means they are difficult to model using plane waves. One way round this problem is to develop approximate pseudopotential functions to model the

interaction between valence electrons and ion cores. There are certain requirements of the core-electron wavefunctions that must be met by the pseudopotential functions. For example, core one-electron wavefunctions must be orthogonal to each other and also to valence wavefunctions. Therefore pseudopotentials are constructed to conform to the orthogonality requirement between core and valence states.<sup>92</sup> Norm-conserving pseudopotentials are also constructed to have the correct amount of charge within the core region compared with the case where all electrons are accounted for explicitly. Pseudopotentials are constructed to be weaker than the true potential, which means that there is less curvature in the core region for valence states, which can therefore be modelled using fewer plane waves. One assumption of the pseudopotential approach is that all core electrons of the same element can be modelled using the same pseudopotential, even in different environments. This is a reasonable assumption as the behaviour of core electrons is similar for atoms of a given element whatever the surrounding system.

An approach which can be used to reduce the cost of electronic-structure-theory calculations is to relax the norm-conservation requirement for the pseudopotentials. This means that the pseudopotentials will be made softer (i.e. requiring a smaller kinetic-energy cutoff for the plane waves in any given calculation). The functions used in this approach are called ultrasoft pseudopotential functions.<sup>93</sup> The relaxation of the norm-conservation requirement introduces an error. However, this error is easy to quantify and can be easily and cheaply corrected. The extra cost of correcting the error is much smaller in magnitude than the saving achieved by using a smaller kinetic-energy cutoff in the calculation. Therefore ultrasoft pseudopotentials are generally much cheaper to use than traditional norm-conserving ones. Overall, the use of pseudopotentials saves a lot of computational cost as it avoids the need to use so many plane waves as the core electrons (which would have needed the largest number of plane waves for accuracy) are modelled using the pseudopotential instead. This allows a smaller cutoff energy to be used. The pseudopotential approximation is the second-largest source of error in the calculations after  $E_{xc}$ .<sup>92</sup> However, it is still a reasonable approximation,

and has substantial benefits for system scaling.<sup>92</sup>

### 2.4.3 Fast Fourier transforms

In the plane-wave pseudopotential method, some calculations can be more easily performed in real space whereas others are cheaper and simpler in reciprocal space. For example, calculating the kinetic energy is much simpler in reciprocal space.<sup>92</sup> Fast-Fourier-transform algorithms allow exact and efficient conversion of functions between their values at a set of real-space grid points and the corresponding values at a set of grid points in reciprocal space. This means the wavefunctions and electron density can be quickly and cheaply converted between real and reciprocal space. This allows the Schrödinger equation to be split up, and components calculated in whichever space is cheaper. This is of particular benefit for larger systems.<sup>92</sup>

### 2.4.4 Energy-minimisation algorithms

As mentioned in Section 2.2.1 the Born-Oppenheimer approximation is used to separate electronic and nuclear degrees of freedom. DFT can be used to calculate the electronic energy for a given set of nuclear coordinates. Starting from a given set of coordinates, an energy-minimisation algorithm can be used to calculate forces acting on nuclei and move them downhill to find new positions. This can be repeated until a minimum is reached and the equations are self-consistent. There are several different types of energy-minimisation algorithm. Some of the most common types are the conjugate-gradient minimisation method, Newton-Raphson and quasi-Newton-Raphson methods.<sup>94</sup>

In a conjugate-gradient method the energy is minimised along a single direction in multi-dimensional phase space, then along a direction that is orthogonal to the previous choice. This is continued until the energy converges. In a Newton-Raphson method the Hessian is calculated in full at every step. This means there will be fewer, more expensive steps. In a quasi-Newton-Raphson method the Hessian is approximated and this approximation is steadily im-

proved each step using information from all previous steps. An example of this class of methods is the Broyden–Fletcher–Goldfarb–Shanno (BFGS) quasi-Newton scheme.<sup>71</sup>

Note that plane-wave pseudopotential methods require an energy-minimisation algorithm for several purposes. An energy-minimisation algorithm is required to relax nuclear coordinates. Based on the Born-Oppenheimer approximation, a Self-Consistent Field (SCF) electronic minimization procedure is required as well. This iterative procedure minimises the electronic energy for each set of nuclear positions. For each step in this SCF process the electronic wavefunction must be calculated for a given potential. It is standard practice to use another energy-minimisation algorithm to find the lowest-energy eigensolutions corresponding to a given potential, rather than solving them directly by matrix inversion. For example, the CASTEP plane-wave code uses the conjugate gradient method for this.<sup>92</sup>

## 2.5 Surfaces studied

Six metals were investigated using the local softness. These comprised three transition metals (rhodium, palladium and platinum) and three coinage metals (copper, silver and gold). Working catalysts consist of a range of mostly low-index facets. However, there will be a variety of facets and sites present, including defect sites with low coordination number that may be particularly important for catalysis. As mentioned in Section 1.2, a large number of important catalytic processes are structurally sensitive. In particular, in various catalytic processes the more reactive, higher-index surfaces are more active in catalysis, particularly in bond-dissociation reactions.<sup>18</sup> It is thought that the particular electronic properties of step-edge and kink sites, such as lower work function, make these ideal for breaking bonds.<sup>19,21</sup> For example, the very strong CO bond can be broken by kink atoms on platinum, but not by any other platinum surface sites.<sup>95</sup> Higher-index facets, which contain defect sites such as step edges or kinks, are therefore important for catalysis.

The analysis of Jenkins and Pratt provides a method of categorising surfaces

based on their symmetry and structure.<sup>96</sup> Surfaces containing two or more close-packed rows are classed as flat. These flat surfaces include fcc  $\{111\}$  and  $\{100\}$ . Surfaces containing only one close-packed row are classed as stepped. Examples include the fcc  $\{110\}$  surface. Kinked surfaces contain no close-packed rows and include the fcc  $\{210\}$  and  $\{531\}$  surfaces. Higher-index surfaces require a larger unit cell for CASTEP calculations. The computational cost of CASTEP calculations scales with roughly  $N^3$ , where  $N$  is the number of atoms in the unit cell. This was a factor in choosing which systems to study. In order to study a range of surfaces but minimise computational cost, relatively low-index flat and stepped surfaces were chosen for the study of local softness. Flat surfaces studied were the fcc  $\{111\}$  and  $\{100\}$ . The stepped  $\{110\}$  surface was also studied. The geometries of these three fcc surfaces are illustrated in Figs. 2.1, 2.2 and 2.3 respectively.

## 2.6 Computational details

CASTEP, a plane-wave code for implementing DFT using periodic boundary conditions, was used for all calculations.<sup>67,97</sup> The version of CASTEP used was 6.11 (released in 2013) for earlier calculations and then 18.1 (released in 2017) for later calculations.<sup>1</sup> There was no significant difference in energies obtained using different versions of CASTEP. This similarity in energies is not very surprising as the CASTEP releases between 2013-2017 mostly consisted of minor additions to functionality and a few bug fixes, rather than fundamental changes to the way the code worked. The exchange and correlation functional used within CASTEP was that of Perdew, Burke and Ernzerhof.<sup>87</sup> The plane-wave-basis-set energy cutoff was 340 eV. The standard CASTEP library pseudopotentials were used for all calculations.<sup>67</sup>

The geometry of the unit cell was of a double-sided slab symmetrically placed in the centre of the supercell. The lateral dimensions of all surfaces were cho-

---

<sup>1</sup>The reader should not be alarmed at the apparent large jump in version numbers. In 2015 the CASTEP developers increased their version number from 8 to version 16. This jump of eight version numbers was due to CASTEP becoming partners with the company Biovia, and did not correspond with a large change in the function of the CASTEP code.

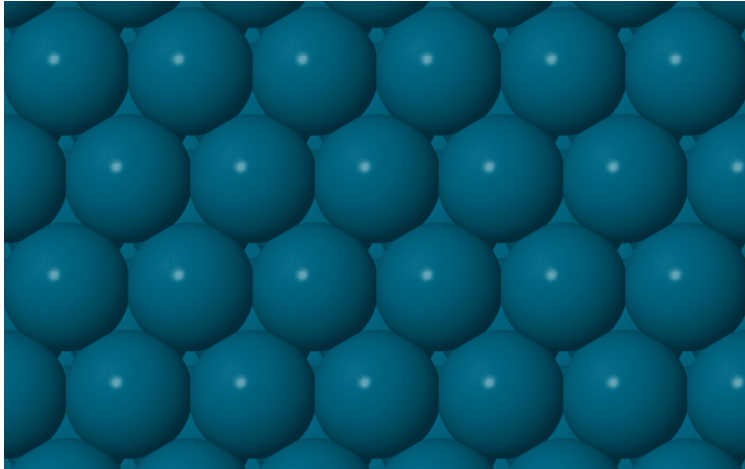


**Figure 2.1:** Face centred cubic {111} facet

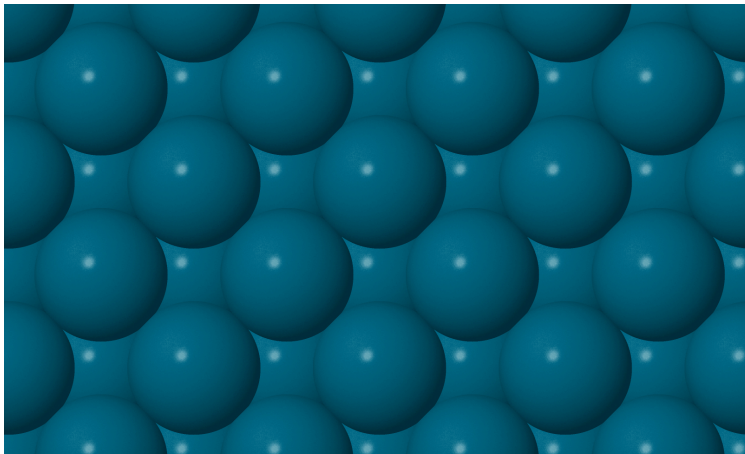


**Figure 2.2:** Face centred cubic {100} facet

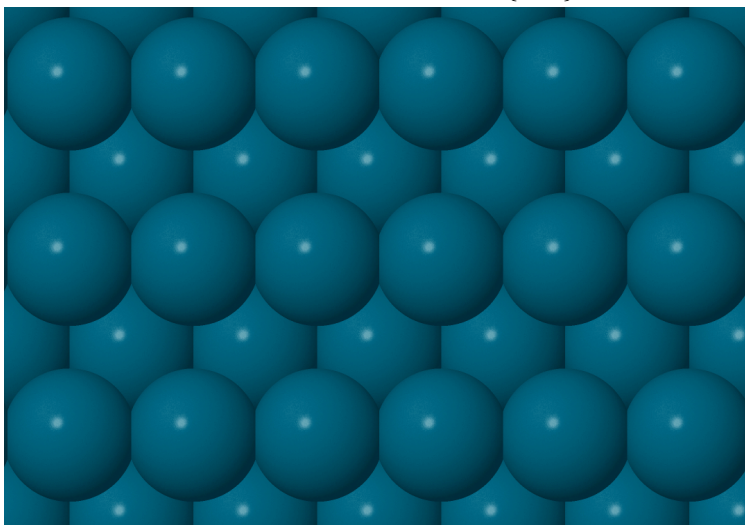


**Figure 2.3:** Face centred cubic {110} facet

sen to be the smallest possible unit cell retaining the surface symmetry. For the  $\{100\}$ ,  $\{111\}$  and  $\{110\}$  surfaces this was the  $(1 \times 1)$  cell. Geometry optimisations were performed using the BFGS quasi-Newton optimisation method implemented in CASTEP.<sup>71</sup> The force tolerance for geometry optimisations was  $0.05 \text{ eV \AA}^{-1}$ . The energy tolerance per atom for geometry optimisations was  $2 \times 10^{-5} \text{ eV}$ . The outermost layers of atoms on both sides of the clean slab were allowed to relax. The inner layers of atoms were constrained along x, y and z axes. The number of layers that were allowed to relax varied according to the layer spacing. See the start of Chapter 3, Section 6.2 and the Appendix for more detail on the number of relaxed layers. The electronic energy tolerance per atom was  $10^{-7} \text{ eV}$  in single point calculations. The convergence testing of  $d\mu/d\sigma$  was performed for the smallest lateral dimensions that preserved the symmetry for each surface.

As explained in Section 2.4.1, calculating the electronic structure requires sampling the first Brillouin zone at a mesh of  $\mathbf{k}$  points in reciprocal space.<sup>98</sup> The sampling along each reciprocal lattice vector  $\mathbf{b}_n$  should be inversely proportional to the length of the corresponding real-space vector  $\mathbf{a}_n$ . For the  $\{100\}$  and  $\{111\}$  surfaces the real-space vectors  $\mathbf{a}_1$  and  $\mathbf{a}_2$  are the same length whereas for the  $\{110\}$  surface the ratio of  $|\mathbf{a}_1|$  to  $|\mathbf{a}_2|$  is  $1 : \sqrt{2}$  which (to the nearest integer) corresponds with a Monkhorst-Pack  $\mathbf{k}$ -point mesh of  $8 \times 6 \times 1$ . Therefore the Brillouin-zone integration was performed using an  $8 \times 8 \times 1$  Monkhorst-Pack  $\mathbf{k}$ -point mesh for the  $\{100\}$  and  $\{111\}$  surfaces and a  $8 \times 6 \times 1$  mesh for the  $\{110\}$  surfaces.

An energy cutoff of 340 eV was used for all surfaces. This was chosen so that oxygen or oxygen-containing molecules (such as CO) could be added to the surfaces without needing to change the energy cutoff. Oxygen requires a higher cutoff energy than most commonly used elements. A cutoff of 340 eV is high enough for oxygen and more than high enough for metals and other elements found in common adsorbates such as C and H. The surface-normal dimension of the supercell and the thickness of the slab and vacuum layers were varied systematically and the softness was calculated.

## 2.7 Notation to describe supercell geometry

A particular CASTEP repeat supercell geometry will be described in terms of the number of layers of slab and vacuum. The latter will always be in terms of the spacing of the metal surface  $d\{hkl\}$ . For example, to specify a certain number of slab and vacuum layers of Cu{100}, the simplified notation

$$n_s + n_v$$

means a supercell with  $n_s$  layers of Cu{100} and  $n_v$  layers of vacuum of thickness  $d(100)$ , where  $d(100)$  is the spacing of the Cu{100} planes. For example a calculation with a repeat unit of 9 layers of Cu{100} slab and 8 layers of vacuum would be referred to as a 9 + 8 calculation. A series with a given constant vacuum thickness and variable  $n_s$  can be described using the same notation. For example the series with variable slab thickness and constant  $n_v = 8$  would be referred to as the  $n_s + 8$  series. Similarly the series with constant  $n_s = 13$  layers and variable  $n_v$  would be referred to as the  $13 + n_v$  series. A series with a constant ratio of  $n_s$  to  $n_v$  is referred to as  $\alpha\%$  where  $\alpha$  is the percentage of vacuum. For example, the 50% series is one where the ratio of  $n_s$  to  $n_v$  is 1 : 1. The length of the supercell surface-normal dimension is referred to as  $c$  with the total number of layers  $n_s + n_v$ .

### 2.7.1 Choice of slab and vacuum thickness

The slab thickness should be large enough that there are negligible interactions between the two surfaces through the slab. Due to the nature of the CASTEP implementation of DFT as a plane-wave calculation, periodic boundary conditions are necessary. Therefore the supercell has an infinite number of repeat images. The vacuum thickness needs to be sufficient that there is negligible interaction between the surfaces and their images in neighbouring supercells.

## 2.8 Problems calculating local softness

### 2.8.1 Charged calculations in CASTEP

It is possible to perform charged calculations in CASTEP<sup>61</sup> but their interpretation is not straightforward. CASTEP applies periodic boundary conditions in order to model periodic systems.<sup>62</sup> This results in problems when doing a calculation of a surface with non-zero charge. The charge of a metal slab localises on the surface (for a two-sided slab at both surfaces). Due to the periodic boundary conditions the system behaves, from an electrostatic point of view, like an infinite number of charged plates at a regular spacing determined by the slab and vacuum thickness. This is a problem as the energy of an infinite set of charged plates would diverge. The way in which CASTEP solves this problem is that an external electric potential is applied so that the overall charge for the supercell is neutral.<sup>62</sup> There is more detail on how this affects the chemical potential in Section 2.10.1.

### 2.8.2 CASTEP energy reference

The energies reported by CASTEP are based on an energy reference that is arbitrarily defined based on the average potential over the whole supercell.<sup>99</sup> The energies obtained by a CASTEP calculation, for example the total energy, chemical potential and other energies, can be compared with each other for a given supercell composition. However, if another calculation is performed with a different number of slab or vacuum layers, then energies will differ due to the difference in energy reference. Similarly, a CASTEP calculation with a different charge will also have a different energy reference, as the compensatory potential that CASTEP adds to neutralise the charge will be different in this case.

One energy reference is defined for each CASTEP calculation. There is no reason to expect the energy reference for two CASTEP calculations to be the same, if the supercells differ. For two calculations with different numbers of vacuum layers, one would expect all energies to be the same from a physical

point of view, provided that both vacuum thicknesses were sufficient to screen fictitious interactions between the metal surfaces. However, the difference in reference energy would cause all CASTEP reported energies to be shifted rigidly between calculations.

Figure 2.4 shows the effect of a change in vacuum thickness on the CASTEP reported energies. The DOS for supercells a and b should be identical as long as the vacuum thickness for both is enough to screen fictitious interactions. However, the slab and vacuum regions have different potentials. Therefore increasing the vacuum thickness changes the average cell potential. This means the CASTEP energy reference used to calculate the energies is different, so all energies are rigidly shifted for calculation b. There are the same number of electrons in each supercell so the difference in the chemical potential is simply the difference in the energy reference  $R$ .

## 2.9 Calculating the local softness

As the numerator of local softness,  $s_{\text{rel}}(\mathbf{r})$ , is known to vary in three-dimensional space but not with external potential, this can be calculated using a single supercell geometry. A simple linear approximation was made in order to calculate the numerator of local softness,

$$s_{\text{rel}}(\mathbf{r}) = \frac{d\rho(\mathbf{r})}{d\sigma} \approx \frac{\rho(\mathbf{r})_+ - \rho(\mathbf{r})_-}{\sigma_+ - \sigma_-} \quad (2.32)$$

where a + or - subscript indicates a quantity calculated for positive and negative surface charge,  $\sigma$ , respectively. It should be noted that it is advantageous to use as small a value of  $\sigma$  as possible, so as to better approximate the derivative. However, below a certain value, numerical accuracy would begin to become a problem. The denominator of local softness is invariant with position in space, but can be expected to be dependent on external potential. The external potential can be expected to vary with supercell geometry for charged calculations. However, unlike  $s_{\text{rel}}(\mathbf{r})$  the denominator of local softness is a global quantity. Therefore if the dependence on external field can be

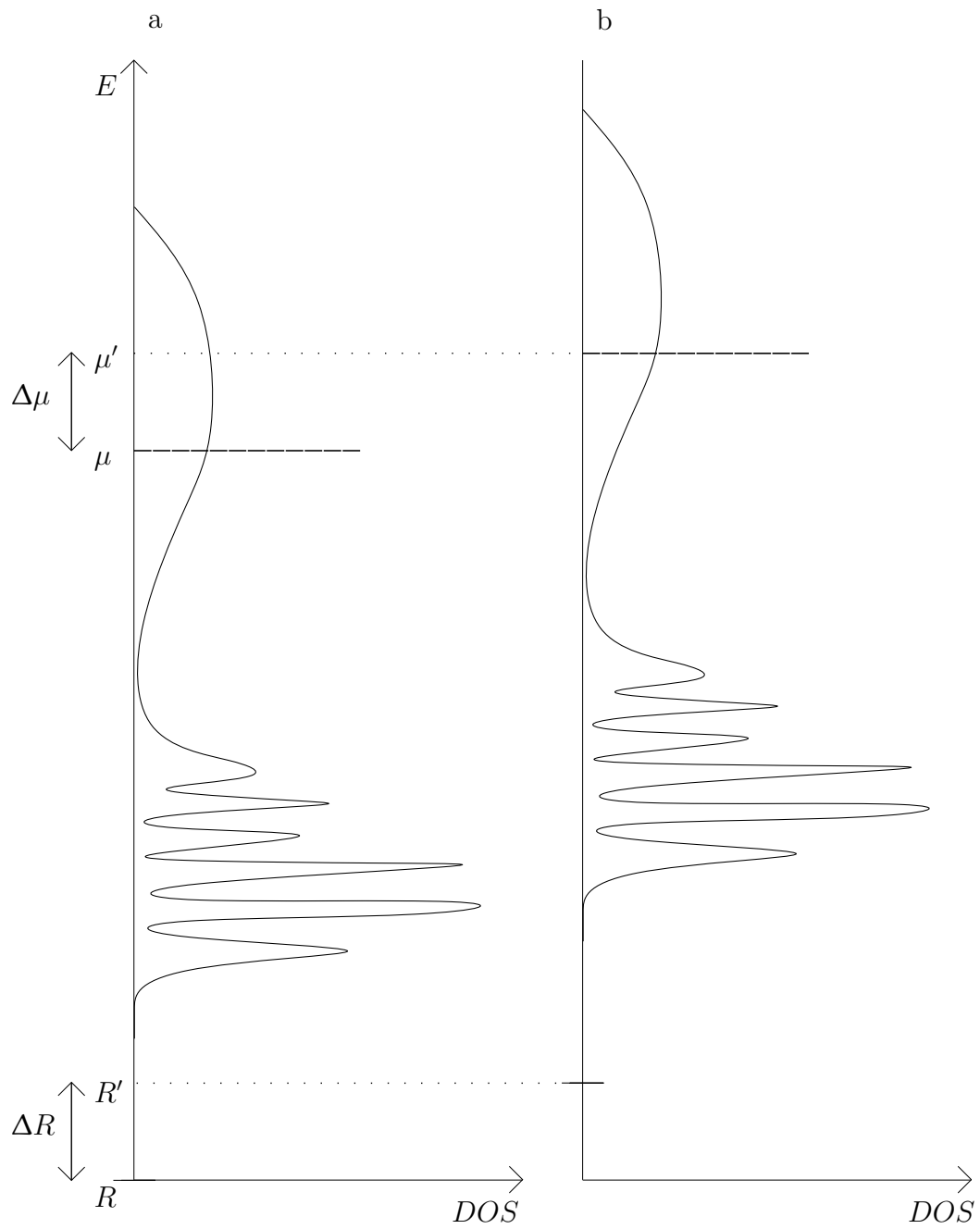


**Figure 2.4:** Hypothetical DOS for two CASTEP supercells a and b. Supercells are identical except that b has a different vacuum thickness.

corrected to find the true denominator of local softness,  $(\partial\mu/\partial\sigma)_{v(\mathbf{r}),T}$ , then this can be used to calculate the local softness by simple division.

## 2.10 Calculating the chemical potential

In order to calculate the denominator of local softness, the chemical potential must first be calculated for different values of surface charge. CASTEP was used to calculate the Fermi level and local potential for each geometry of supercell. For the purposes of this study, it was assumed that the Fermi level was equal to the chemical potential. This is reasonable for a metal with no band gap.<sup>100</sup> Several methods of calculating the chemical potential were investigated.

### 2.10.1 Uncorrected chemical potential

The denominator of local softness can be calculated using the CASTEP reported values of the chemical potential for different surface charges. However, there is a problem with calculating the chemical potential this way. As explained in Section 2.8.1, CASTEP applies periodic boundary conditions. The energy of an infinite set of charged plates would diverge. CASTEP solves the problem of charge by applying an external potential. However, from Eqn. 1.22, it can be seen that the external potential  $v(\mathbf{r})$  should be constant. One way of solving this problem is to extrapolate to infinite slab and vacuum thickness. For an infinitely large cell, there would be no periodic neighbours and so there would be no charge interaction. Therefore the potential applied by CASTEP would approach zero as the cell size approached infinity.

A second problem comes from the way in which CASTEP defines the reference potential. The CASTEP reference potential cannot be expected to be constant with charge or supercell geometry. Therefore it is not straightforward to compare the energy or chemical potential of two surfaces with a different vacuum thickness, even though they should be identical. In addition, changing the charge would also change the reference potential.

## 2.10.2 The CASTEP energy reference

The CASTEP estimate of the denominator of the local softness,  $d\mu/d\sigma$ , was calculated using a linear approximation:

$$\frac{d\mu}{d\sigma} \approx \frac{\mu_+ - \mu_-}{\sigma_+ - \sigma_-} \quad (2.33)$$

where  $\mu_+$  is the chemical potential for a given positive surface charge  $\sigma_+$  and  $\mu_-$  is the chemical potential for a given negative surface charge  $\sigma_-$ . This method was used irrespective of whether  $\mu$  was corrected as described in Section 2.10.3. In order for the linear approximation to hold, a small surface charge was chosen equivalent to  $\pm 0.1 e$  per supercell. The problem with the approach in Eqn. 2.33 is that the outputted chemical potential,  $\mu^{\text{CASTEP}}$ , is relative to an unknown energy reference that changes with charge and supercell dimensions.

$$\mu_+^{\text{CASTEP}} = \mu_+ - R_+ \quad (2.34)$$

where  $\mu_+$  is the true chemical potential for a given positive charge and  $R_+$  is the CASTEP energy reference for the same charge. There is an equivalent expression for the outputted chemical potential for negative charge,

$$\mu_-^{\text{CASTEP}} = \mu_- - R_- \quad (2.35)$$

where  $\mu_-$  is the true chemical potential for a given negative charge and  $R_-$  is the CASTEP energy reference for the same charge.

All energies outputted by CASTEP for a single calculation are relative to the same energy reference. Therefore it would be helpful to find an energy  $C$  (or set of energies) that can be expected to be constant with added charge and supercell dimensions. The expression for this energy as outputted by CASTEP would therefore be

$$C_+^{\text{CASTEP}} = C - R_+ \quad (2.36)$$

where  $C$  is a constant energy that can be expected to be invariant with changing charge and supercell dimensions.  $C_+^{\text{CASTEP}}$  is the CASTEP outputted value of  $C$  relative to the CASTEP energy reference for a given supercell and for  $+\sigma$  surface charge. The equivalent expression for negative charge would be

$$C_-^{\text{CASTEP}} = C - R_- \quad (2.37)$$

where  $C$  and  $R_-$  are defined as above.  $C_+^{\text{CASTEP}}$  and  $C_-^{\text{CASTEP}}$  can be used to correct the CASTEP outputted chemical potential so it is no longer dependent on the CASTEP energy reference. This is done by subtracting  $C^{\text{CASTEP}}$ . When Eqns. 2.34 and 2.36 are substituted in, the terms in  $R_+$  cancel out.

$$\mu_+^{\text{corr}} = \mu_+^{\text{CASTEP}} - C_+^{\text{CASTEP}} = \mu_+ - C \quad (2.38)$$

There is an equivalent expression for negative charge,

$$\mu_-^{\text{corr}} = \mu_-^{\text{CASTEP}} - C_-^{\text{CASTEP}} = \mu_- - C \quad (2.39)$$

Equations 2.38 and 2.39 can be subtracted to cancel out the dependence on  $C$

$$\mu_+^{\text{corr}} - \mu_-^{\text{corr}} = \mu_+ - \mu_- \quad (2.40)$$

Equation 2.40 can then be substituted into Eqn. 2.33, resulting in the following expression for the corrected denominator of local softness:

$$\frac{d\mu}{d\sigma} \approx \frac{\mu_+^{\text{corr}} - \mu_-^{\text{corr}}}{\sigma_+ - \sigma_-} \quad (2.41)$$

Several methods of correcting the chemical potential were investigated:

- Correcting the chemical potential using the slab average potential
- Correcting the chemical potential using the bulk slab average potential (excluding a number of surface layers)
- Correcting the chemical potential using the DOS obtained from a simple CASTEP tool
- Performing an extremely precise DOS calculation using OptaDOS, then using cross-correlation of the DOS for positive and negative charge to obtain the shift. This shift can then be used to correct the shift in chemical potential for different charges.

### 2.10.3 Slab average potential correction

One approach used to try to solve the problem of the variable CASTEP energy reference was to correct the chemical potential using the average potential of the slab. In this approach, the corrected chemical potential,  $\mu_{\text{corr}}$ , is defined as

$$\mu_{\text{corr}} = \mu_{\text{calc}} - V_{\text{slab}} \quad (2.42)$$

where  $\mu_{\text{calc}}$  is the uncorrected chemical potential reported by CASTEP relative to the CASTEP reference potential.  $V_{\text{slab}}$  is the average bulk potential, which is also calculated by CASTEP relative to the reference it uses. However, the physical value of the average slab potential should certainly be constant for all supercell geometries. Therefore the calculated value of  $\mu_{\text{corr}}$  should be a true measure of the chemical potential.

In order to calculate the slab average potential, the CASTEP formatted potential file was used. This was averaged along the x and y coordinates so that only the dependence on the surface-normal direction was kept. This produces data of the sort shown in Fig. 2.5. The positions of the outermost

minima are found and then an average is performed over the whole of the x and y dimensions and over the region of the slab indicated with the solid horizontal line in Fig. 2.5. This method averages between the outermost minima in the xy-average potential. This should be relatively constant with added charge. In order to improve this and make sure that  $V_{\text{slab}}$  was independent of charge as required by the approach in Eqns. 2.41-2.38, I also investigated a modified method where one, two or three of the outermost minima were excluded from the average.

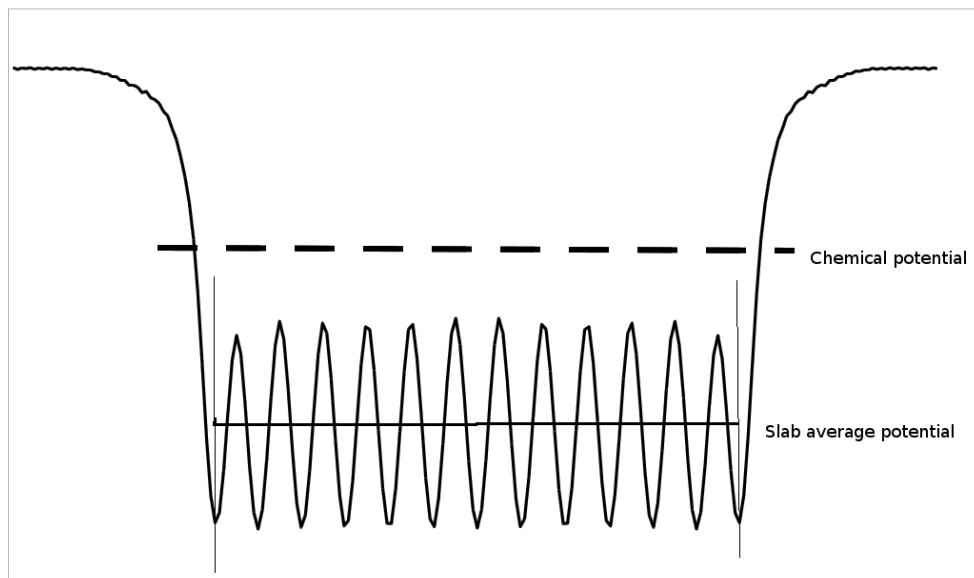


**Figure 2.5:** Method of calculating the slab average potential  
Vertical lines indicate positions of outermost minima between which the average is performed

In Fig. 2.5 the xy-average potential shows a variation with z coordinate. Minima in the potential correspond to the the z coordinates of layers of atoms. In this figure it can be seen that the surface layers of atoms at each side of the slab are slightly higher in potential than bulk layers. This is a result similar to that for most low-index surfaces.

As mentioned in Section 1.9, the calculated value of  $d\mu/d\sigma$  cannot be expected to be equal to the denominator of local softness,  $(\partial\mu/\partial\sigma)_{v(r)}$ . This will be the case even for the corrected denominator calculated using  $\mu_{\text{corr}}$ .

Therefore as the CASTEP energy reference can be expected to be dependent on the supercell geometry, whereas the true denominator is not, convergence testing was performed with respect to the supercell dimensions. This was performed for  $d\mu/d\sigma$  and the quantities connected to it, the chemical potential and average slab potential. The convergence of the corrected  $d\mu/d\sigma$  was analysed with  $n_s$ ,  $n_v$  and supercell surface-normal repeat length  $c$ . This will be discussed in Chapter 3.

$$(\partial\mu/\partial\sigma)_{v(\mathbf{r})} = (d\mu/d\sigma)_{c\rightarrow\infty} \quad (2.43)$$

#### 2.10.4 DOS correction method: bands2dos

CASTEP has a utility called bands2dos that can be used to obtain simple Densities of States (DOS). As the shift in reference potential should affect all energies reported by CASTEP in the same way, the DOS could be used to correct for the effects of shifting energy reference. Unfortunately, although the bands2dos method is cheap, the DOS produced is not precise enough to be able to calculate an accurate value for the shift in energy reference. A more accurate DOS would be needed to correct the chemical potential.

#### 2.10.5 DOS correction method: OptaDOS

The OptaDOS code was developed by Andrew Morris, Chris Pickard Rebecca Nicholls, Jonathan Yates and others to calculate very accurate density of states (DOS) and spectra.<sup>101,102</sup> They developed a way to obtain accurate DOS by integrating over the Brillouin zone using a linear extrapolation broadening method.<sup>103,104</sup>

As explained in Section 2.10.1, all energies in CASTEP are reported relative to an energy reference, which changes with charge and supercell dimensions. In Section 3.1.3 it was suggested that if  $d\mu/d\sigma$  is calculated relative to this changing energy reference then it will never converge with supercell dimensions. It would be helpful to know the CASTEP energy reference for each calculation so it could be corrected for. However, this energy reference is not

outputted by the CASTEP code.

One way of solving this problem is to find an energy or set of energies that should remain constant with added charge as well as with supercell dimensions. Therefore any change in these energies with charge and supercell dimensions simply reflects the change in the CASTEP energy reference, which can therefore be corrected for. An example of a set of energies that should be constant with changing charge is the occupied density of states (DOS) well below the Fermi level. As these states are occupied, they are not likely to change with added electrons. This means that the only change in the DOS well below the Fermi level with increasing charge is due to the change in CASTEP energy reference. Therefore the DOS well below the Fermi level can be used to correct for changes in CASTEP energy reference.

A standard CASTEP calculation does not output the DOS but a tool called OptaDOS can be used to calculate an accurate DOS from the band structure outputted by CASTEP.<sup>101-105</sup> As the DOS is a function of energy, the best way to calculate an accurate shift in energy with changing energy reference is to calculate the cross-correlation of the DOS for negative charge with the DOS for positive charge. The DOS in general would be a continuous function with energy  $D(E)$ . However, the DOS can only realistically be calculated when sampled at a set of energy points with index  $m$ . This is a discrete function  $D(E_m)$ . The cross-correlation of two discrete functions  $f$  and  $g$  is defined as

$$(f \star g)[n] = \sum_m f^*[m]g[m + n] \quad (2.44)$$

where  $f^*[m]$  denotes the complex conjugate of  $f[m]$ .  $n$  is the index by which the two functions are shifted relative to each other.<sup>106,107</sup> The value of the shift index  $n$  that results in the maximum value of  $(f \star g)[n]$  can be used to calculate the shift in energy reference with varying charge. This can then be used to correct the chemical potential and calculate an accurate value for  $d\mu/d\sigma$ .

$$E_{\text{shift}} = C_+^{\text{CASTEP}} - C_-^{\text{CASTEP}} \quad (2.45)$$

Equations 2.36 and 2.37 can be substituted in for  $C_+^{\text{CASTEP}}$  and  $C_-^{\text{CASTEP}}$  and terms in  $C$  cancel, resulting in the following equation

$$E_{\text{shift}} = -(R_+ - R_-) \quad (2.46)$$

It would be helpful to express Eqn. 2.33 in terms of  $\mu_+^{\text{CASTEP}}$ ,  $\mu_-^{\text{CASTEP}}$  and  $E_{\text{shift}}$ . In order to do this, Eqns. 2.34 and 2.35 can be substituted into an expression of the difference between the CASTEP reported chemical potentials. This can then be used to find an alternative expression for the numerator of Eqn. 2.33.

$$\mu_+^{\text{CASTEP}} - \mu_-^{\text{CASTEP}} = \mu_+ - \mu_- - (R_+ - R_-) \quad (2.47)$$

The third term on the right of Eqn. 2.47 can be recognised from Eqn. 2.46 as  $E_{\text{shift}}$ . This can be used to express the numerator of Eqn. 2.33 in terms of  $\mu_+^{\text{CASTEP}}$ ,  $\mu_-^{\text{CASTEP}}$  and  $E_{\text{shift}}$ .

$$\mu_+ - \mu_- = \mu_+^{\text{CASTEP}} - \mu_-^{\text{CASTEP}} - E_{\text{shift}} \quad (2.48)$$

Equation 2.48 can then be substituted into Eqn. 2.33 to result in an expression that does not require an expression for the unmeasurable CASTEP energy reference.

$$\frac{d\mu}{d\sigma} \approx \frac{\mu_+^{\text{CASTEP}} - \mu_-^{\text{CASTEP}} - E_{\text{shift}}}{\sigma_+ - \sigma_-} \quad (2.49)$$

### 2.10.6 Computational details for spectral tasks and OptaDOS

There are three options for estimating the broadening in OptaDOS (in order to estimate the DOS based on spectra specified at a finite number of  $\mathbf{k}$  points). These are adaptive, linear and fixed broadening. For adaptive and linear broadening, an optics spectral task was performed using CASTEP and then OptaDOS was run using the CASTEP optical matrix elements and band structure. For fixed broadening, a DOS spectral task was performed using CASTEP and then OptaDOS was run with fixed broadening using the band structure as outputted by CASTEP. The smearing widths used for fixed broadening were 0.1, 0.2, 0.3 and 0.4 eV. For all the broadening types, the spectral task  $\mathbf{k}$  point grid was  $30 \times 30 \times 1$  for the  $\{111\}$  and  $\{100\}$  surfaces and  $30 \times 21 \times 1$  for the  $\{110\}$  surfaces. The other computational details were as specified in Section 2.6. It should be noted that while a large number of  $\mathbf{k}$  points were used for the spectral tasks, each spectral task started with a singlepoint calculation for which the  $\mathbf{k}$  points used were those specified in Section 2.6.

## Chapter 3

# Calculating the Denominator of Local Softness

As discussed in the previous chapter, there are various problems with using energies as outputted directly by CASTEP, as these are relative to an arbitrarily defined energy reference. Also, the external potential is not constant when supercell dimensions and charge are varied. The effect this has on the quantities that are outputted directly by CASTEP will be discussed in Section 3.1 below. As explained in the previous chapter in Section 2.10.2, there are several possible methods of correcting the energies obtained by CASTEP. These methods involve subtraction of the energy of a quantity that should be constant with increasing supercell dimensions and charge. The methods that were investigated to correct the chemical potential were subtracting the slab average potential (which will be discussed in Section 3.2) and cross-correlating the DOS (which will be discussed in Section 3.3). The latter method was found to be preferable, and therefore was used to calculate the denominator for eighteen metal surfaces, in Section 3.4. Throughout this chapter, the  $(1 \times 1)$  lateral dimensions were used. As will be discussed in the following sections, the number of slab and vacuum layers were varied, but in all cases a double-sided slab was used and the outermost layers were allowed to relax. For the  $\{100\}$  and  $\{111\}$  surfaces, three layers were allowed

to relax on either side of the slab. The  $\{110\}$  surface had a smaller layer spacing, so four layers were relaxed on each side of the slab.

### 3.1 Convergence of uncorrected properties

As mentioned above, the thickness of the slab and vacuum layers in the repeat unit should have no physical effect on  $s(\mathbf{r})$ . This would be expected to be true provided the number of slab layers,  $n_s$ , is large enough to prevent finite size effects.<sup>108</sup> However, the number of vacuum and slab layers is expected to have a computational effect, following the argument set out in Sections 1.9 and 2.9. This would arise as CASTEP applies a fictitious potential to offset the effect of charge distributions in the unit cell. As charge in a metal slab generally is found at the surface, effectively a charged calculation with periodic boundary conditions will consist of an infinite number of charged sheets. The potential of an infinitely repeating set of sheets of charge can be expected to be a function of the spacing between them. Therefore it can likewise be expected that the corrective potential applied by CASTEP may vary according to the vacuum and slab layer spacings.

The convergence of the CASTEP ‘out of the box’ properties was tested with respect to supercell dimensions for the Cu $\{100\}$  surface. These were tested for certain datasets where either the slab or vacuum thickness was varied, keeping the other thickness constant. The datasets tested included two that kept the slab thickness constant and varied the vacuum thickness (referred to as  $10 + n_v$  and  $23 + n_v$ ). There were also two datasets that kept the vacuum thickness constant and varied the slab thickness (referred to as  $n_s + 8$  and  $n_s + 18$ )

#### 3.1.1 Convergence of the numerator of local softness

The numerator of local softness,  $d\rho/d\sigma$ , can be expected to be constant with supercell dimensions as the local electron density is conserved when the dimensions of the supercell are increased. Therefore if the local softness itself is not constant with increasing supercell dimensions then this can be expected

to be as a result of a change to the denominator of local softness.

### 3.1.2 Uncorrected denominator convergence

The denominator of local softness as defined in Eqn. (1.22) is an intensive quantity that should be constant with supercell dimensions. However, as explained above in Section 3.1, this was not found to be the case due to problems with the way CASTEP defines the energy reference and due to the potential CASTEP adds to neutralise the charge. Figure 3.1 shows a strong positive correlation between  $n_s$  and  $d\mu/d\sigma$ . For both values of  $n_v = 8$  and 18 the value of  $d\mu/d\sigma$  increases with increasing  $n_s$  to a maximum value. However, the asymptotic value is different for each dataset, at about  $0 \text{ eV } \text{\AA}^2 e^{-1}$  for the  $n_s + 8$  dataset and  $-50 \text{ eV } \text{\AA}^2 e^{-1}$  for the  $n_s + 18$  dataset. The shape of the curve of  $d\mu/d\sigma$  with respect to  $n_s$  is strongly dependent on  $n_v$  for a given dataset of constant  $n_v$ .

In contrast, Fig. 3.2 shows a clear decrease in  $d\mu/d\sigma$  as the number of vacuum layers increases. In addition, the relationship is nearly linear. The slopes of the lines differ but are relatively similar, in contrast to the significant difference in curve shape between the two constant  $n_v$  datasets in Fig. 3.1. The magnitude of the change in  $d\mu/d\sigma$  with increasing  $n_v$  is significantly larger than the change with increasing  $n_s$ . The addition of 20 layers of vacuum decreases  $d\mu/d\sigma$  by  $500 \text{ eV } \text{\AA}^2 e^{-1}$  whereas in Fig. 3.1  $d\mu/d\sigma$  increases by  $150 \text{ eV } \text{\AA}^2 e^{-1}$  when 20 layers of slab are added in the  $n_s + 18$  dataset.

As can be observed in Figs. 3.1 and 3.2, the denominator of local softness as calculated from the CASTEP value of the Fermi level scales approximately linearly with vacuum thickness and exponentially with slab thickness. This suggests that the denominator of local softness is not constant with supercell dimensions. There is no physical reason to expect this. It can therefore be deduced that the strong relationship between  $d\mu/d\sigma$  and supercell dimensions is due to the way in which CASTEP defines the reference energy, and also due to the way in which CASTEP applies a potential to balance the applied charge. This would match the predictions made in Section 2.10.2.

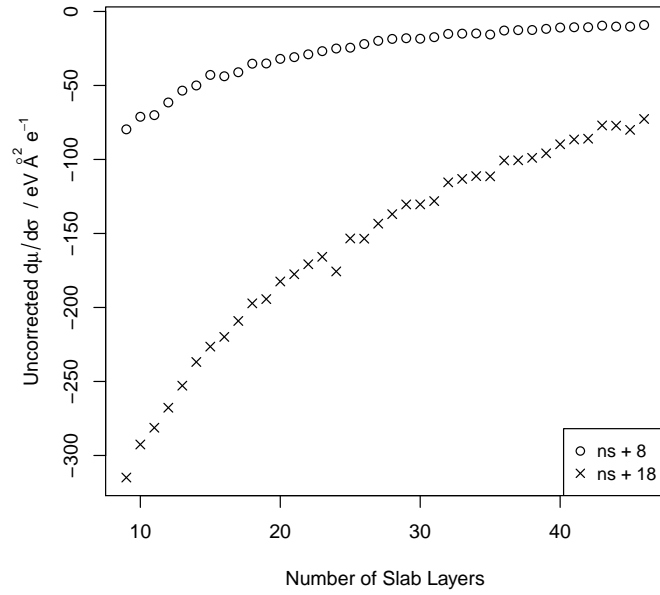


**Figure 3.1:** Convergence of Uncorrected  $\frac{d\mu}{d\sigma}$  with Number of Slab Layers for Cu{100}

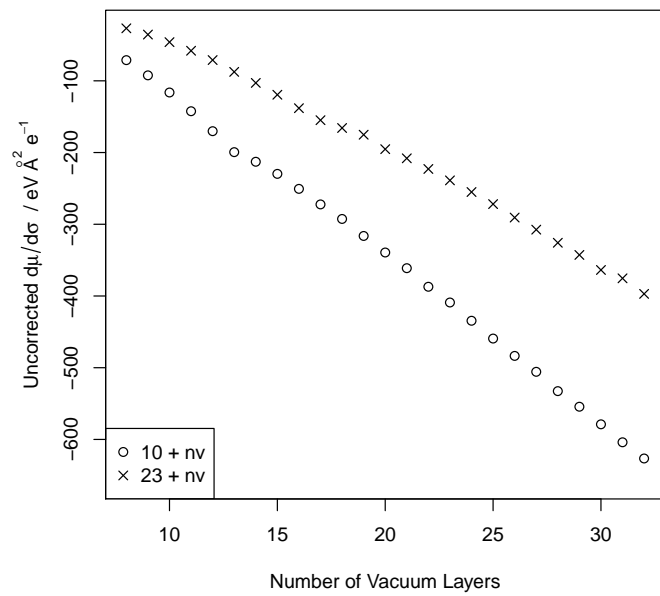


**Figure 3.2:** Convergence of Uncorrected  $d\mu/d\sigma$  with Number of Vacuum Layers for Cu{100}

### 3.1.3 Convergence of $\mu$ and slab average potential

As the surface charge will be constant with respect to surface-normal supercell dimensions, the variation of  $d\mu/d\sigma$  with different slab and vacuum thickness must be due to changes in the chemical potential. Therefore it would be helpful to look at the convergence of  $\mu$  with respect to supercell dimensions. The uncorrected chemical potential was calculated for the Cu{100} surface. The  $10 + n_v$ ,  $23 + n_v$ ,  $n_s + 8$  and  $n_s + 18$  datasets were studied. It would be helpful to test the hypothesis that the variation in the energies obtained with different charge and supercell dimensions was partly due to a change in the supercell average potential and therefore the energy reference. This hypothesis could be tested by looking at the convergence of an energy as calculated by CASTEP that should be constant with supercell dimensions, as discussed in Section 2.10.2. An example of an energy that should be suitable for this purpose is the average potential in the slab,  $V_{\text{slab}}$ . If the hypothesis about the impact of the changing reference potential were correct, then one would expect to see the same shape in the convergence of  $\mu$  as of  $V_{\text{slab}}$  with respect to supercell dimensions. This hypothesis was tested by comparing the convergence of  $\mu$  with that of  $V_{\text{slab}}$  in Figs. 3.3-3.10 below.

In order to test the dependence of properties calculated by CASTEP upon the CASTEP reference energy, it would be helpful to consider a system that has neutral charge. This will mean that CASTEP will not need to add a compensating external potential, so the potential will be constant with changing geometry. Figures 3.3-3.6 show the convergence of the uncorrected chemical potential (in the upper panels) and the slab average potential (in the lower panels). Figures 3.3 and 3.4 show the convergence with respect to the number of slab layers for supercells with a constant vacuum thickness with  $n_v = 8$ . Figures 3.5 and 3.6 show the convergence with respect to  $n_v$  for supercells with a constant slab thickness of 10 layers of Cu{100}.

Figures 3.3 and 3.4 have shapes that are very similar to each other. Therefore the convergence with respect to the number of slab layers is very similar for the chemical potential and the slab average potential. Both  $\mu$  and  $V_{\text{slab}}$

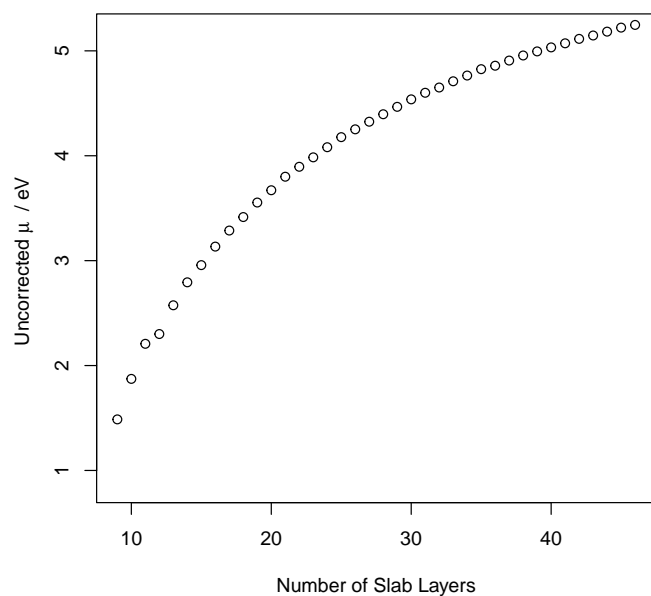


**Figure 3.3:** Convergence of Uncorrected  $\mu$  with Number of Slab Layers for the Cu{100}  $n_s + 8$  zero-charge dataset

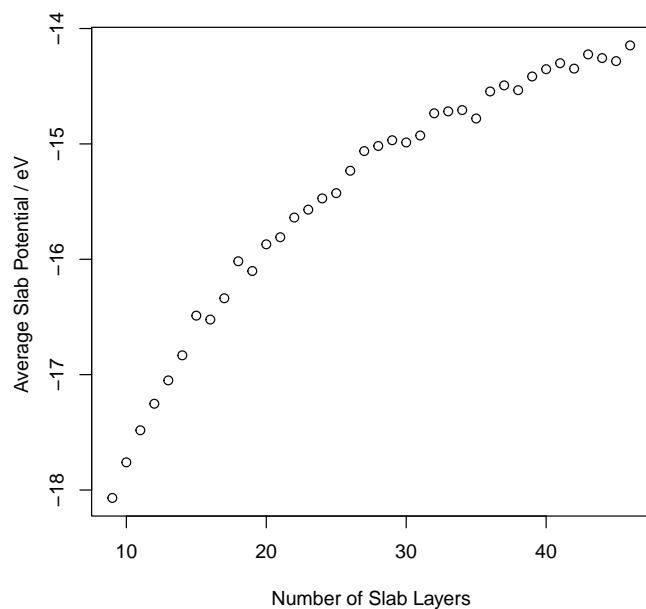


**Figure 3.4:** Convergence of Average Slab Potential with Number of Slab Layers for the Cu{100}  $n_s + 8$  zero-charge dataset

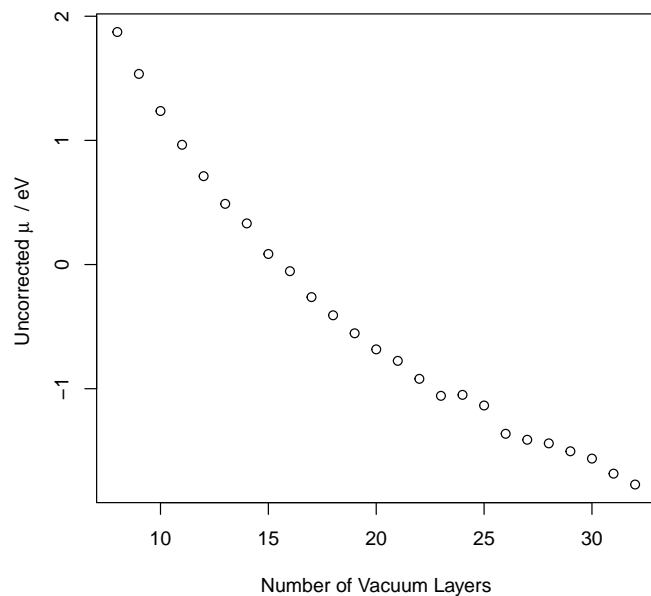


**Figure 3.5:** Convergence of Uncorrected  $\mu$  with Number of Vacuum Layers for the Cu{100}  $10 + n_v$  zero-charge dataset

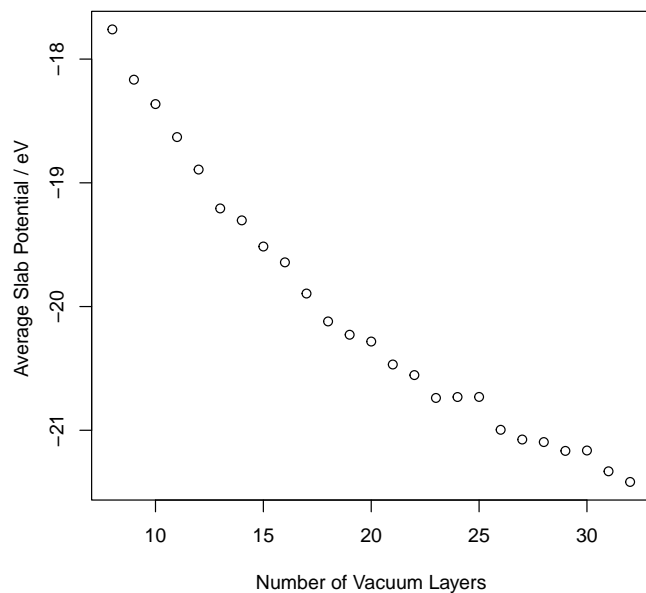


**Figure 3.6:** Convergence of Average Slab Potential with Number of Vacuum Layers for the Cu{100}  $10 + n_v$  zero-charge dataset

increase exponentially with increasing slab thickness towards a plateau. The main difference between the two is that there is more numerical noise in the plot of the average slab potential. This increased amount of noise is probably due to the averaging process.

Figures 3.5 and 3.6 also have shapes that are similar to each other, though different from the shape of the convergence with slab thickness in Figs. 3.3 and 3.4. In particular, the chemical potential and slab average potential decrease with increasing vacuum thickness. The shape of the curve is quasi-linear in both cases, which may simply be noise around a linear trend. Alternatively, it may just be a very slowly changing exponential, which would mean that eventually for large enough vacuum thickness the chemical potential and slab average potential would converge to a constant value.

For the zero-charge case it appears that most of the change in the chemical potential with varying supercell dimensions is because of a change in the CASTEP reference energy. It would be interesting to see how the picture changes with added charge. Also it would be interesting to see whether datasets with different constant values of slab or vacuum thickness would fall on the same curve. Therefore the convergence of  $\mu$  and  $V_{\text{slab}}$  was compared for different charges in Figs. 3.7-3.10.

Figures 3.7 and 3.8 show the convergence with respect to slab thickness for supercells with a constant  $n_v$  of 8 (circles) and 18 (crosses). The upper panel shows the convergence of the chemical potential and the lower panel that of the slab average potential. As for the zero-charge calculation, the chemical potential and slab average potential show very similar convergence with respect to the slab thickness. Irrespective of charge and whether  $n_v$  is 8 or 18 layers, the curves in both panels increase with increasing slab thickness towards a constant value for high slab thickness. Therefore both the slab average potential and the uncorrected chemical potential,  $\mu$ , increase with  $n_s$  for a dataset of constant  $n_v$ . Negatively-charged supercells have a higher uncorrected chemical potential. This is to be expected as the chemical potential is essentially a measure of the highest filled energy level at a temperature of 0 K. Interestingly, the increase in uncorrected  $\mu$  with charge is much larger

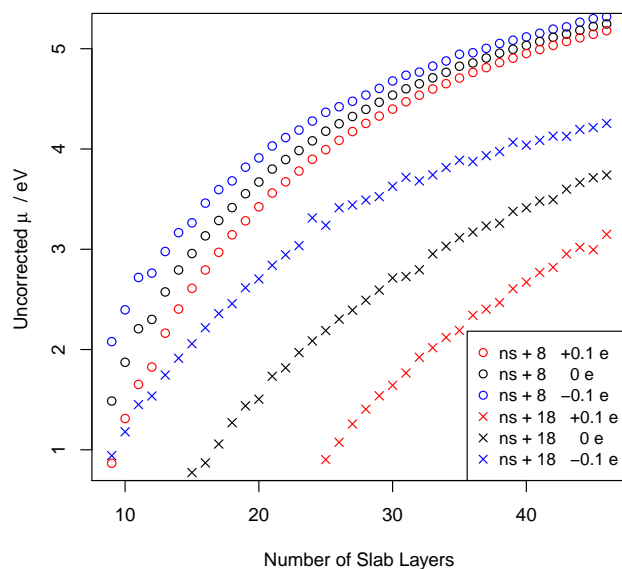
in magnitude for the dataset with a larger number of vacuum layers.

In general as  $n_s$  increases the chemical potential increases towards an asymptotic value of approximately 6 eV for the  $n_s + 8$  dataset and 4.5 eV for the  $n_s + 18$  dataset. The energy difference between the curves with positive and negative charge decreases with increasing  $n_s$ , especially for the dataset with a larger number of vacuum layers. This matches the trend in Fig. 3.1 where the denominator takes a larger magnitude (more negative value) for 18 vacuum layers compared with that for 8 vacuum layers.

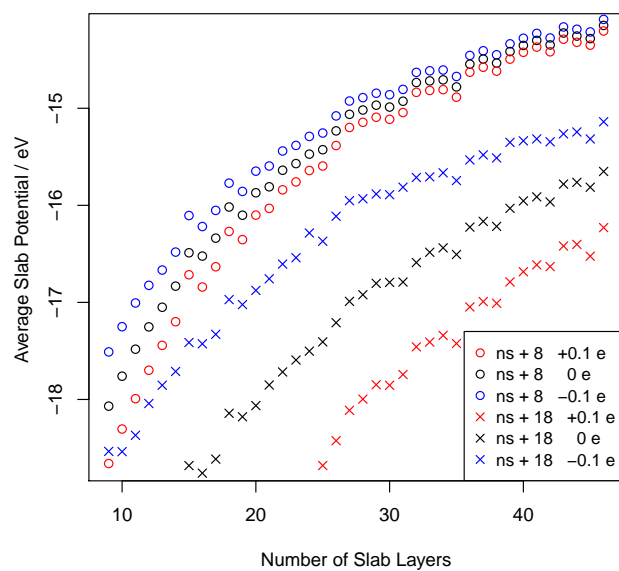
Figure 3.8 shows a remarkably similar convergence of the average slab potential with  $n_s$  to that shown in Fig. 3.7. The average slab potential increases with increasing  $n_s$  and also appears to have an exponential relationship. For  $n_s \rightarrow \infty$  the slab average potential approaches a constant value of approximately  $-13$  eV for the  $n_s + 8$  dataset and  $-15$  eV for the  $n_s + 18$  dataset. There is a very strong relationship between the shapes of the  $V_{\text{slab}}$  curves and the uncorrected  $\mu$  curves. This suggests that the reason for most of the change in both  $V_{\text{slab}}$  and uncorrected  $\mu$  is the change in the CASTEP reference potential with supercell dimensions. This is consistent with the argument put forth in the previous chapter in Section 2.10.2.

Figure 3.9 shows a clear decrease in uncorrected  $\mu$  with increasing  $n_v$ . However, the mathematical form of the relationship differs markedly between differently-charged supercells. The uncharged and negatively-charged calculations show an exponential decay towards a constant value of approximately 0 eV for the  $10 + n_v$  dataset and -3 eV for the  $23 + n_v$  dataset. In contrast, the positively-charged supercell shows a very strong linear dependence for both datasets. This is very interesting as the difference in charge is not very great. In addition this implies that if  $d\mu/d\sigma$  is calculated using the uncorrected chemical potential then  $d\mu/d\sigma$  would never converge with supercell dimensions. This is the trend observed in Fig. 3.2. This suggests that using the CASTEP raw value of  $\mu$  to calculate  $d\mu/d\sigma$  will not enable the calculation of the denominator of local softness.

Figure 3.10 shows a similar dependence on  $n_v$  as that seen in Fig. 3.9. In



**Figure 3.7:** Convergence of Uncorrected  $\mu$  with Number of Slab Layers for Cu{100}



**Figure 3.8:** Convergence of Average Slab Potential with Number of Slab Layers for Cu{100}

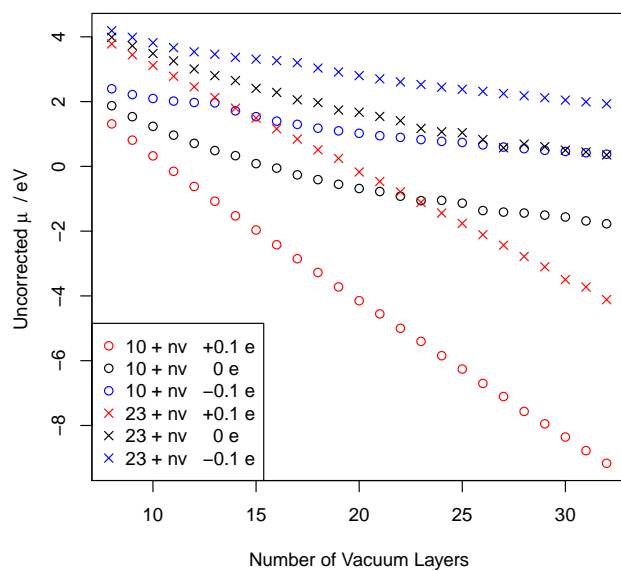


**Figure 3.9:** Convergence of Uncorrected  $\mu$  with Number of Vacuum Layers for Cu{100}

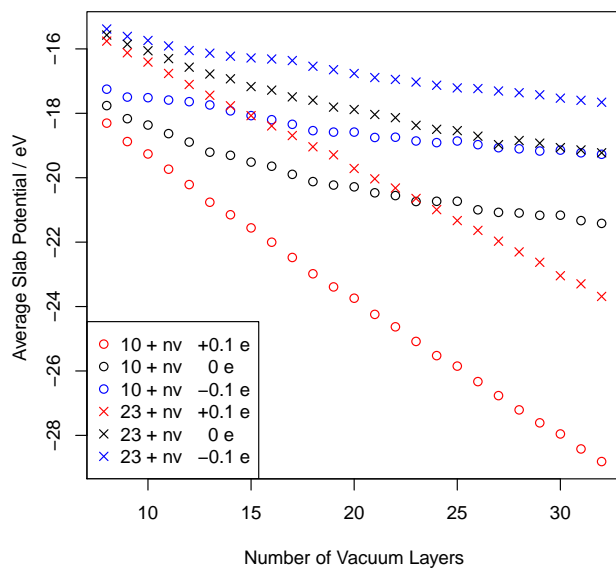


**Figure 3.10:** Convergence of the Average Slab Potential with the Number of Vacuum Layers for Cu{100}

particular,  $V_{\text{slab}}$  decays exponentially towards a constant value for neutral or negatively-charged supercells. As for Fig. 3.9, the slab average potential decreases linearly with  $n_v$  for positively-charged supercells in both datasets. The curve shapes and gradients in Figs. 3.9 and 3.10 are very strongly correlated. Combined with the similarity of the behaviour with increasing  $n_s$  this is strong evidence that the main change in both uncorrected  $\mu$  and  $V_{\text{slab}}$  is due to the change in the CASTEP reference potential, as suggested in the previous subsection.

### 3.1.4 Implications for the method of calculating $\mu$

The correlation of curve shape and slope between uncorrected  $\mu$  and  $V_{\text{slab}}$  is strong evidence in favour of using the correction procedure of Eqns. 2.42. It can be expected that the resultant values of  $\mu_{\text{corr}}$  will be independent of the CASTEP reference potential. This method can therefore be expected to produce a value of  $d\mu/d\sigma$  that will vary with supercell dimensions only due to physical reasons or changes in the CASTEP applied potential. The convergence of the denominator that was corrected by subtracting the slab average potential from the chemical potential will be discussed in the next section.

## 3.2 Slab average potential correction

Having established that correcting the chemical potential is advisable, the corrected denominator of local softness was calculated. This involved correcting the chemical potential for changes in the CASTEP energy reference by subtracting the slab average potential. The convergence with respect to the supercell dimensions was analysed. As explained earlier in the chapter, there is no physical reason to expect that the denominator of local softness should depend on supercell dimensions, provided that the vacuum and slab layers are thick enough to prevent self-image interactions and finite-size effects. However, it can be predicted that as CASTEP applies a fictitious potential to correct for charged calculations this could have an impact on

convergence. The convergence of the corrected denominator of local softness with slab thickness, vacuum thickness and overall surface-normal supercell dimension was evaluated.

### 3.2.1 Convergence with slab thickness

Figure 3.11 shows the convergence of  $\frac{d\mu}{d\sigma}$  (corrected by the slab average potential) with respect to slab thickness. The two datasets in the figure have different constant vacuum thickness, with either eight or eighteen vacuum layers. There is a similar convergence with slab thickness for both the 8 vacuum layer and 18 vacuum layer datasets. In both datasets the denominator of local softness increases with slab thickness and seems to tend towards a constant value for infinite slab thickness. However, the asymptotic limits of the curves differ, being higher for a larger vacuum thickness. Also it seems that the errors increase with vacuum thickness, as the dataset with 18 vacuum layers is significantly more noisy than that with 8 vacuum layers.

One interesting feature of the datasets in Fig. 3.11 is that there is a great deal of oscillation for small slab thickness. These oscillations occur for both vacuum thicknesses where the slab thickness is  $\lesssim 25$  Å. As the layer spacing for Cu{100} is about 1.81 Å, this slab thickness is equivalent to 14 slab layers. The oscillations decay quickly with increasing slab thickness, becoming negligible for  $n_s \gtrsim 18$ , or slab thickness  $\gtrsim 33$  Å. Figure 3.12 shows a zoomed-in view of the oscillations for  $n_s = 10 - 13$ , which is equivalent to a thickness of 18-23.5 Å. There are eleven datasets in the figure, each with a different constant vacuum thickness. For all datasets, there is the same trend that with increasing slab thickness the corrected denominator first decreases and then increases again. It is clear from Fig. 3.12 that oscillations with slab thickness dominate over the differences between series with different vacuum thickness. For example, adding one layer of atoms from 10 to 11 decreases  $d\mu/d\sigma$  by  $3.5 \text{ eV } \text{Å}^2 e^{-1}$  whereas adding ten layers of vacuum from 8 to 18 changes  $d\mu/d\sigma$  by only  $1 \text{ eV } \text{Å}^2 e^{-1}$ .

The eleven series in Fig. 3.12, each with different vacuum thickness, have

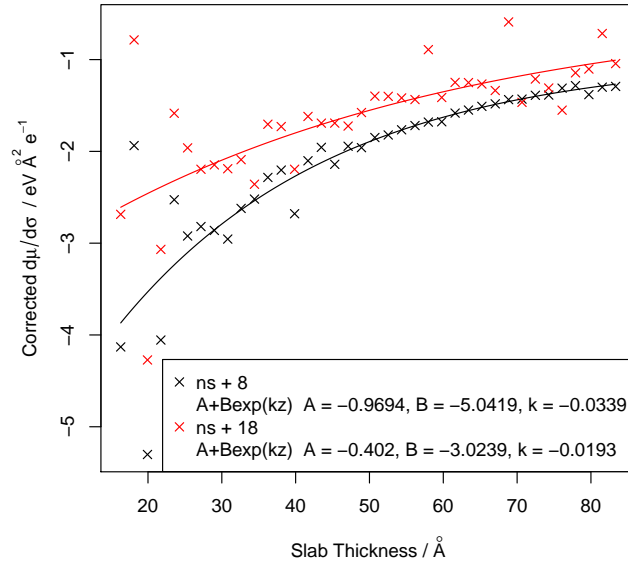


**Figure 3.11:** Convergence of corrected  $\frac{d\mu}{d\sigma}$  with slab thickness for Cu{100}

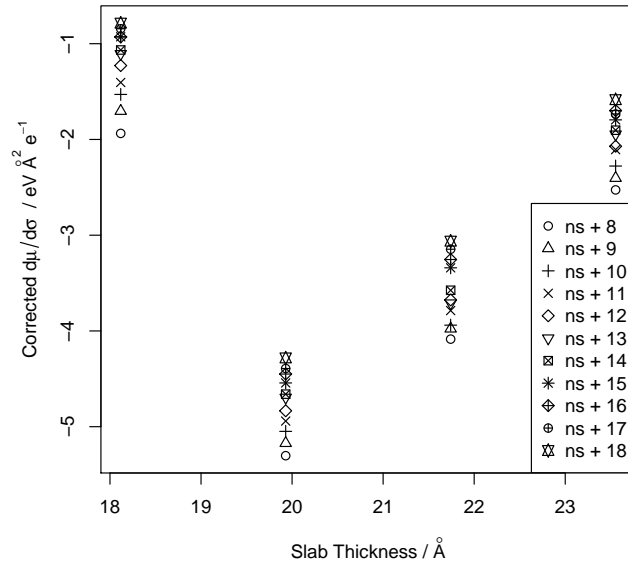


**Figure 3.12:** Oscillations of corrected  $\frac{d\mu}{d\sigma}$  with slab thickness for thin slabs for Cu{100}

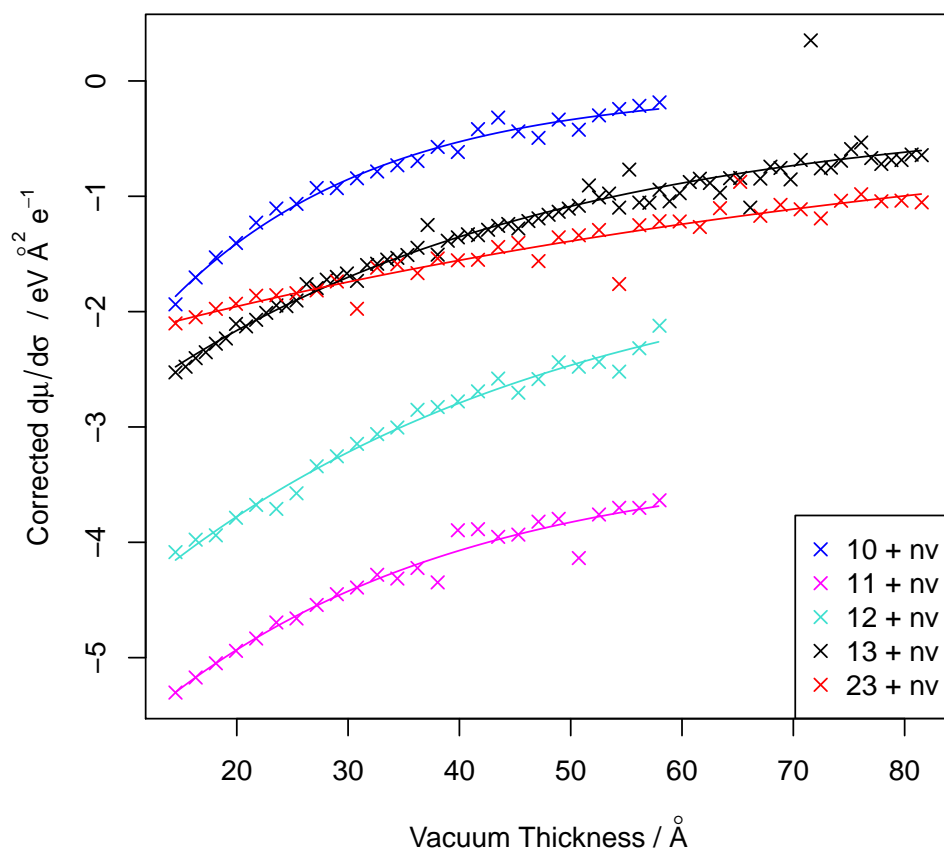


**Figure 3.13:** Convergence of Corrected  $\frac{d\mu}{d\sigma}$  with Vacuum Thickness for Cu{100}

the same oscillatory ‘V’ shape with increasing slab thickness. This ‘V’ shape is rigidly displaced to higher  $\frac{d\mu}{d\sigma}$  for each dataset with larger vacuum thickness. The magnitude of the oscillations with increasing slab thickness is the same for all series in Fig. 3.12. This suggests the slab and vacuum degrees of freedom are not strongly coupled in this region. The oscillations with slab thickness decay rapidly to become negligible for  $n_s \gtrsim 18$ . They are independent of the vacuum thickness. This suggests that the oscillations may arise due to electrostatic coupling between the charged surfaces through the slab. The rapid oscillations as the slab thickness increases is typical of finite-size effects, which have been observed, for example, in thin aluminium films by Aballe and co-workers.<sup>108</sup> The physical cause of these is likely to be the coupling of surface resonances across the slab.<sup>109–111</sup>

### 3.2.2 Convergence with vacuum thickness

Figure 3.13 shows the convergence of the denominator (corrected using the slab average potential) with respect to the vacuum thickness. There are five datasets in the graph, each with a different fixed number of slab layers, from 10-23. As observed earlier in Figs. 3.11 and 3.12 corrected  $d\mu/d\sigma$  increases with increasing vacuum thickness. In Fig. 3.13 it is clear that the corrected  $d\mu/d\sigma$  increases towards a maximum with increasing vacuum thickness. This is similar to the behaviour with increasing slab thickness but without the oscillatory behaviour for thin layers that is so marked in Figs. 3.11 and 3.12.

Four of the datasets have a small enough number of slab layers (10-13) that finite-size effects can be expected to be significant, based on the discussion in the previous subsection. In Fig. 3.12 the convergence of corrected  $d\mu/d\sigma$  with respect to the number of slab layers forms a ‘V’ shape where for 10 slab layers the denominator is very high, then for 11 slab layers it is very low. The denominator then increases for 12 and then 13 slab layers. These trends in the denominator with respect to slab thickness are the case for all the curves with varying vacuum thickness. As noted before in Section 3.2.1 the oscillations for small slab thickness are much greater in magnitude than the

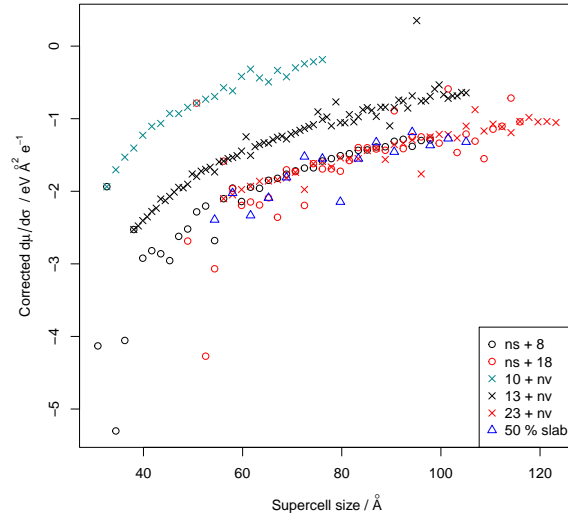
magnitude of variation with increasing vacuum thickness. The curves of the denominator with increasing vacuum thickness are rigidly shifted and appear to be converging to different values where the finite-size effects apply. The datasets with a constant  $n_s \lesssim 15$  appear to be converging to very different values for infinite vacuum thickness. This effect is especially pronounced for 10, 11 and 12 slab layers in Fig. 3.13.

The converged value of  $d\mu/d\sigma$  with vacuum thickness is very sensitive to slab thickness for  $n_s \lesssim 15$  in Fig. 3.13. Also as noted in Section 3.2.1 the magnitude of oscillations with slab thickness is the same for all  $n_v$  series in Fig. 3.12. This has implications for how meaningful extrapolating  $\frac{d\mu}{d\sigma}$  to large vacuum thickness is if this is done for finite slab thickness. In particular, the extrapolated value would be very far from the true converged value of  $\frac{d\mu}{d\sigma}$  if this was done for a constant slab thickness that was in the oscillatory region.

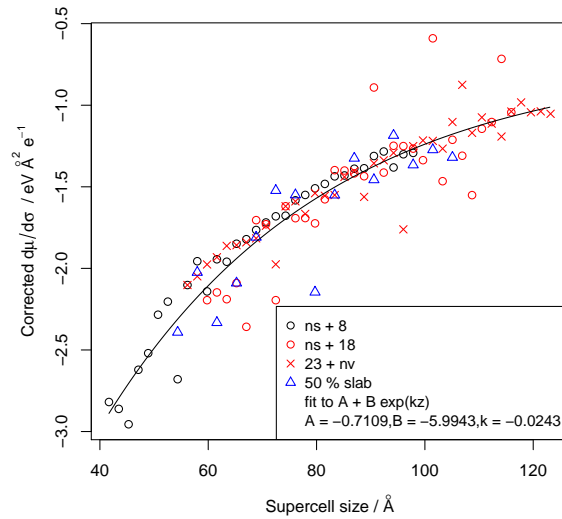
### 3.2.3 Convergence with surface-normal supercell dimension

Figure 3.14 shows the convergence of the corrected denominator of local softness with the surface-normal supercell dimension. The datasets either have a constant fixed slab thickness and varying vacuum, constant fixed vacuum thickness and varying slab thickness, or a constant ratio of slab to vacuum and varying total supercell thickness. It can be seen from Fig. 3.14 that the corrected denominator of local softness increases as the total surface-normal supercell size,  $c$ , increases for all datasets. The gradient decreases with increasing supercell size and it appears that the datasets in all cases are converging to a constant value. However, there is quite a lot of noise in the graph, which makes it difficult to know this for certain.

As long as the slab layer thickness is larger than about 32 Å the data points for all datasets appear to lie on the same curve and be converging to the same constant value. This can be seen more clearly in Fig. 3.15. Once the physical effect of insufficient slab thickness is excluded there should be no physical



**Figure 3.14:** Convergence of corrected  $\frac{d\mu}{d\sigma}$  with surface-normal supercell dimension for Cu{100}



**Figure 3.15:** Convergence of corrected  $\frac{d\mu}{d\sigma}$  with surface-normal supercell dimension for Cu{100}. This graph consists of a subset of the data for the previous graph, with large enough  $n_{\text{slab}}$  to avoid finite-size effects

reason for the size of the supercell to change the electronic properties of the system. The remaining curve, which fits all the data, depends only on the surface-normal repeat length, not the composition of the supercell itself. The surface-normal repeat length ( $c$ ) is the length governing the strength of self-image interactions between repeats of the supercell. In particular, this will be the length scale over which a charged surface will interact electrostatically with its images.

This suggests that while the method of correcting the chemical potential by subtracting the average slab potential works well at removing the effect of the CASTEP reference potential, there is a weak interaction between each surface and its repeat images that remains even after this correction has been made. This interaction decays for increasing supercell size  $c$  which gives some hope that, at least for Cu{100}, the denominator may converge in a well-behaved manner. However, it will be shown later in Section 3.3 that this is not always guaranteed. However, it was assumed that it was possible to extrapolate to infinite supercell surface-normal dimensions for Cu{100}. The denominator of local softness for Cu{100} was estimated from the fitted parameter  $A$  in Fig. 3.15. The denominator of local softness for the Cu{100} surface was therefore calculated as  $-0.71 \text{ eV \AA}^2 e^{-1}$ .

### 3.2.4 Problems with slab average potential correction

In Section 3.2.3 the denominator was corrected using the slab average potential, followed by an extrapolation to infinite surface-normal supercell size. The slab average potential was calculated between the outermost minima in the xy-average potential, as shown in Fig. 2.5. However, there were several problems with this approach, particularly that there was a lot of numerical noise.

In addition, the basis for correcting the chemical potential as in Eqns. 2.38 and 2.42 is in order to remove the dependence on the CASTEP variable energy reference. This only works if the quantity used to correct the chemical potential is itself invariant with charge. The charge on a metal slab accumu-

lates at the surface. Therefore an average potential between the outermost minima in the  $xy$ -average potential would include this charged surface region. An alternative approach was tried that would alleviate this problem, by calculating the average over a region that excludes a certain number of minima from the  $xy$ -average potential. This would mean that the charged surface region was excluded from the slab average potential, which should mean that  $V_{\text{slab}}$  was independent of charge. In this case, Eqn. 2.41 can be used to calculate the denominator of local softness.

While this approach of excluding several of the outermost minima from the slab average potential is more theoretically justifiable, it does not solve the problem of numerical noise. Also there were Friedel oscillations in the  $xy$ -average potential for some surfaces.<sup>78</sup> This made it difficult to have a systematic way of choosing the region over which to calculate the slab average potential.

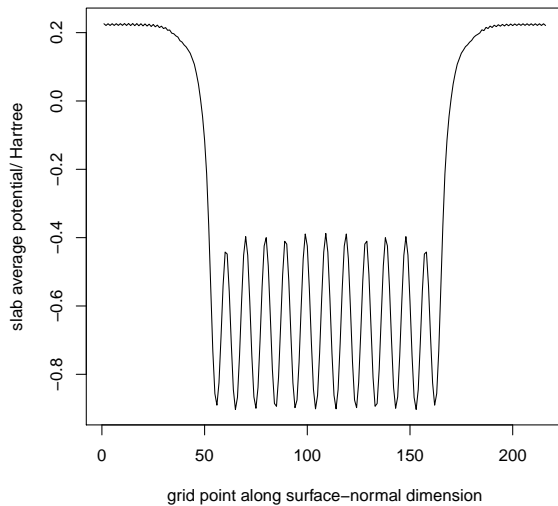


**Figure 3.16:**  $xy$ -average potential as a function of surface-normal supercell index  $k$  for the Cu{100} 12 + 10 supercell

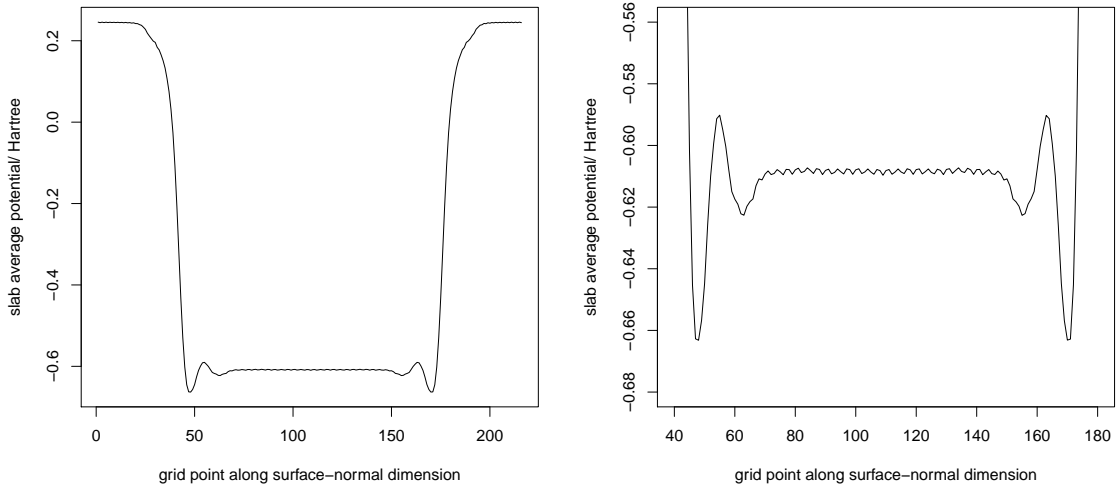


**Figure 3.17:**  $xy$ -average potential as a function of surface-normal supercell index  $k$  for a  $\text{Cu}\{531\}$   $41 + 24$  supercell. Panels show progressively more zoomed-in versions of the same data.

### 3.2.5 Friedel oscillations in the $xy$ -average potential

The method of calculating the slab average potential detailed in Section 2.10.3 involves averaging over the region between the outermost minima in the  $xy$ -average potential. This method can be expected to work well where the bulk average potential is very similar to the average potential near the surface. For the  $\text{Cu}\{100\}$  surface this is the case, as shown in Fig. 3.16. In Fig. 3.16, there are twelve minima in the  $xy$ -average potential that correspond with the twelve layers of atoms in the surface-normal dimension. These minima all have similar energy values. Excluding the outermost minima from the region over which the average is conducted would result in a slab average potential that would be very similar to that obtained from the method in Section 2.10.3. In contrast, in Fig. 3.17, calculated for the  $\text{Cu}\{531\}$   $41 + 24$  supercell, there are 29 minima, fewer minima than layers of atoms. This is because of Friedel oscillations that affect the surface region.<sup>78</sup> The outermost minima are very low in energy compared with the bulk region. Excluding the outermost minima from the region to be averaged over would affect the

slab average potential significantly.

To conclude, there are two main problems with using the slab average potential to correct the denominator of local softness. These are numerical noise and Friedel oscillations. The effect of these issues is that while a converged value for the denominator can be obtained using this correction method, there is considerable uncertainty in its value. A different method of correcting the chemical potential is desirable, particularly if it could result in less noise. This would allow a more reliable measure of the converged corrected denominator of local softness.

### 3.3 DOS cross-correlation correction

As discussed in Section 2.10.5, the DOS below the Fermi level can be expected to be constant with respect to different charge and supercell dimensions. Therefore a cross-correlation of the DOS obtained for positive charge with the DOS obtained for negative charge should give the shift in energy reference between a positively-charged calculation and a negatively-charged calculation. This can then be used to correct the difference in chemical potential, which allows the denominator to be calculated in a way that should be independent of the energy reference, as expressed in Eqn. 2.41. This method of correcting the denominator was tested for a range of surfaces.

There are various options for how to calculate the band structure and how to perform the cross-correlation of the DOS. The DOS was calculated both by `bands2dos` and `OptaDOS`. The former was found to produce a DOS that did not have enough detail to perform an accurate cross-correlation, whereas `OptaDOS` produces a DOS with plenty of detail to fit a cross-correlation and find an accurate shift. Therefore `OptaDOS` was used. However, there are several options within `OptaDOS` that were investigated. In particular, `OptaDOS` has an option to use adaptive, linear or fixed broadening. The broadening is required to obtain the DOS by integrating over the eigenfunctions, which are approximated at a set of discrete  $\mathbf{k}$  points in the Brillouin zone. There are various different methods which `OptaDOS` can use in order

to solve this problem and approximate the broadening.

Fixed broadening is the simplest method, where band dispersion is accounted for by using a Gaussian broadening function of fixed width  $\omega$ .<sup>102</sup> This does not require an optics spectral task, but does require a large number of  $\mathbf{k}$  points in order to obtain an accurate result.<sup>102</sup> Linear broadening divides reciprocal space into a series of tetrahedra, and calculates the broadening based on a linear interpolation. This approach results in a DOS that retains sharp features, which is more accurate, and is also helpful from a point of view of cross-correlating the DOS.<sup>102</sup> However, linear broadening requires the optical matrix elements, which need to be calculated in an expensive CASTEP optics spectral task. The third option is adaptive broadening, which was developed in order to try to combine the advantages of the linear and fixed broadening.<sup>102</sup> The convergence of the denominator calculated using different types of broadening was compared. This required a spectral task followed by an OptaDOS calculation. The computational details for the spectral task and OptaDOS calculations are described in Section 2.10.6.

### 3.3.1 Comparing OptaDOS broadening methods

OptaDOS calculates the density of states based on an integration over the Brillouin zone.<sup>102</sup> This integration is performed for data recorded at a finite set of  $\mathbf{k}$  points. Therefore in order to find the integral, some kind of broadening function must be used at each  $\mathbf{k}$  point. It is well established to use Gaussian functions for this. As discussed above, there are three possible broadening methods, fixed, linear or adaptive. The three types of broadening were compared and it was found that the linear and adaptive broadening were much more expensive. This is because they require a CASTEP optics spectral task.

There was also a problem with some of the CASTEP output files needed for linear or adaptive broadening. The optical matrix elements file sometimes contained entries which were ‘not a number’ (NaN). This probably implies that at some point in the CASTEP code a number was divided by zero.

This error caused some spectral tasks to fail completely. In other cases, even though the spectral task appeared to succeed, there were NaN entries in the optical matrix elements CASTEP output file, which meant OptaDOS then failed to calculate the DOS. These problems arose due to a ghost peak in the unoccupied region of the DOS. A ghost peak is a non-physical, extremely sharp peak that arises due to the pseudopotential. These problems affected the optics spectral tasks that were required for linear or adaptive broadening.

Fixed broadening avoids the problem of the ghost peak, which meant that all the spectral tasks and OptaDOS jobs succeeded. It requires a DOS spectral task that was computationally simpler and cheaper than the optics spectral task required for linear or adaptive broadening. There was also less noise in the DOS and the denominator of local softness obtained using fixed broadening compared with linear broadening. However, one of the disadvantages of using fixed broadening was that as the broadening width is specified, the DOS produced was a function of the broadening width. This had an effect on the value of the corrected denominator. In order to give a qualitative indication of the uncertainty in the corrected denominator of local softness, the fixed broadening was computed for four different broadening widths of 0.1, 0.2, 0.3 and 0.4 eV. For more details see Section 2.10.6. In the figures that follow, the average was plotted, with the standard deviation plotted as an error bar. It should be noted that this is a qualitative measure and not intended to be read as the actual error, which may be greater. As fixed broadening was more reliable and cheaper, this method was chosen for all calculations reported below.

### **3.3.2 Convergence with surface-normal supercell dimension**

The denominator was calculated using fixed broadening. As mentioned above, it was unclear what value of the smearing width should be used, so four different values of 0.1, 0.2, 0.3 and 0.4 eV were used and the mean was calculated between all four. This mean is plotted against surface-normal

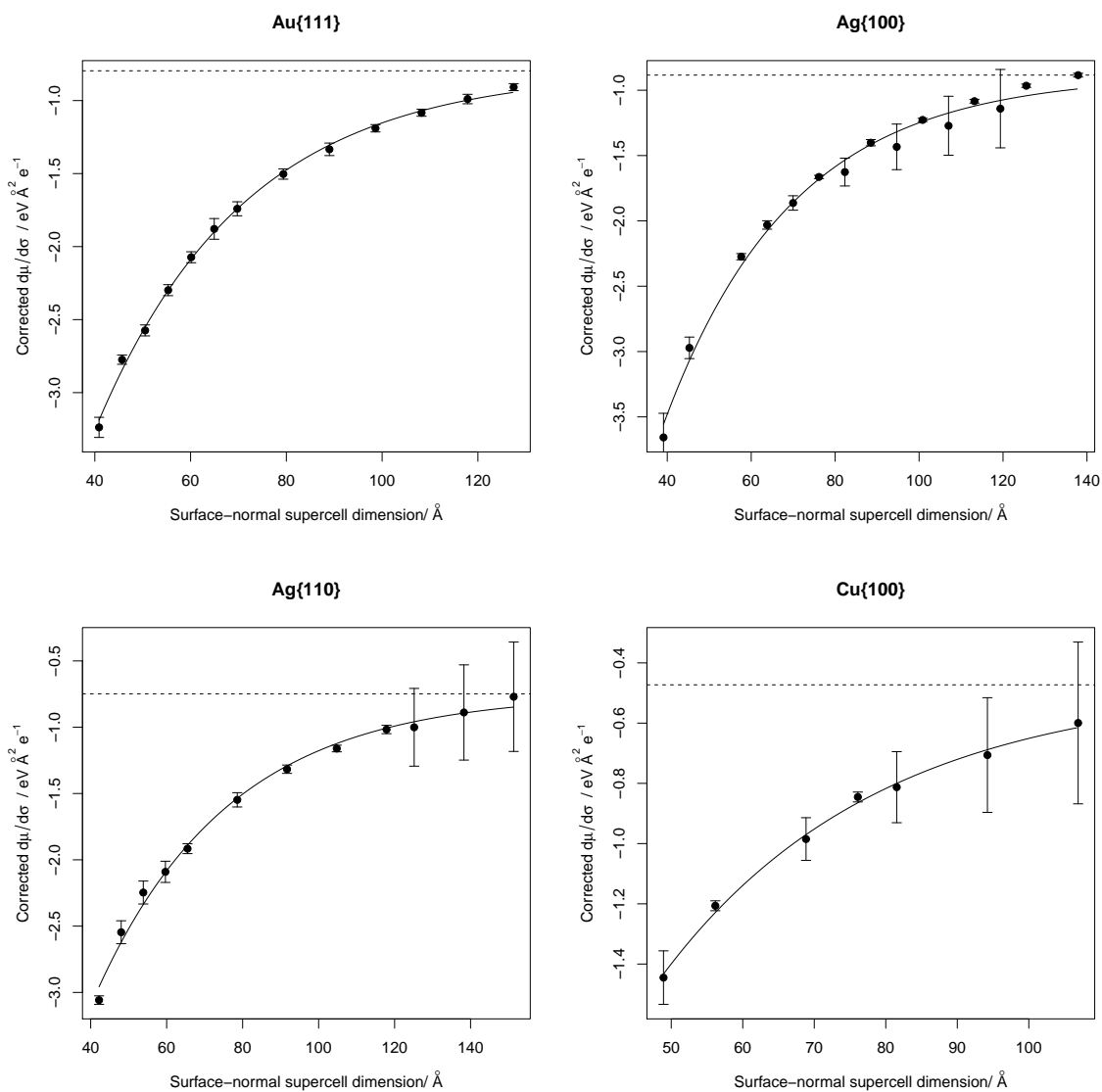


**Figure 3.18:** Graphs of the denominator of local softness obtained using fixed broadening for four different coinage-metal surfaces. Data was plotted for a variety of slab to vacuum ratios. The dotted line shows the extrapolated denominator at infinite supercell surface-normal dimension

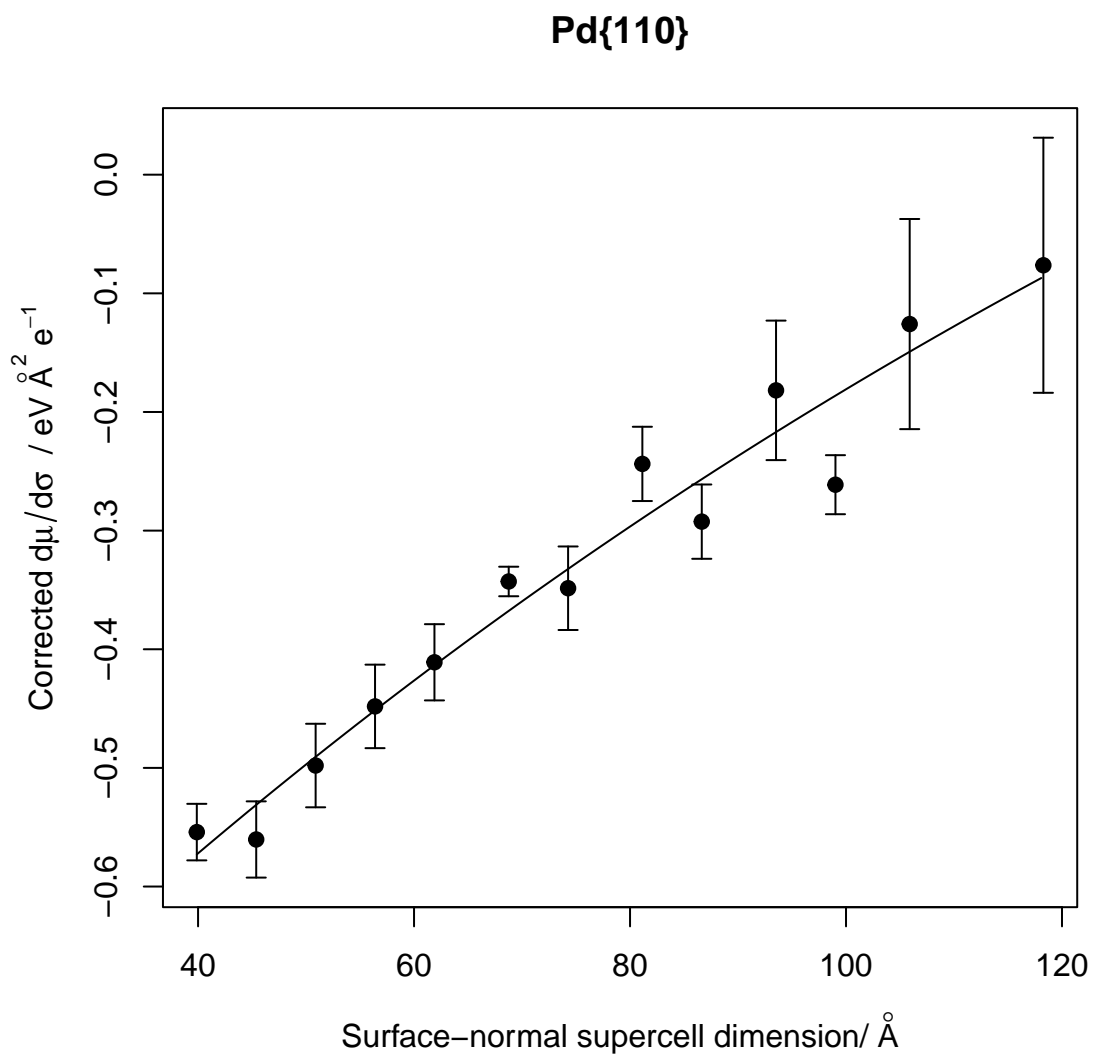


**Figure 3.19:** Graph of the denominator of local softness obtained using fixed broadening for Pd{110}.

supercell dimension in Fig. 3.18. Error bars in Fig. 3.18 are from the standard deviation of the denominator for each smearing width. They reflect the uncertainty in the denominator due to the choice of smearing width.

As earlier results for the denominator corrected by the slab average potential had suggested that the ratio of slab to vacuum thickness was not important once the slab thickness was great enough, a variety of slab to vacuum ratios were used. The error bars were much larger for datapoints with a large vacuum thickness. This means that for a large vacuum thickness the denominator of local softness is more dependent on the choice of smearing width. For small vacuum thickness there is very little difference between the smearing widths. For example, all the data in the Au{111} dataset is for a small vacuum thickness, and the data points were very similar for all the different smearing widths, so the resulting error bars are small.

Convergence with supercell surface-normal dimension was analysed for a variety of metal surfaces. The convergence of the corrected denominator of local softness was plotted as a function of the surface-normal dimension of the supercell. Generally for coinage metals it was found that it was possible to fit an exponential to the total supercell surface-normal dimension and that it did not matter if slab or vacuum thickness was varied. This is similar to the results obtained for Cu{100} with the slab average potential correction method, as discussed in Section 3.2.3. In contrast, this was less frequently the case for transition-metal surfaces, where the ratio of slab to vacuum thickness appeared to matter a great deal. This is shown in Fig. 3.19 where the curve bifurcates to form two separate exponentials for increasing slab versus increasing vacuum. As a result of this, the effect of changing the ratio of slab to vacuum was investigated directly and the results of this are shown in Fig. 3.20

In Fig. 3.18, there are a variety of datasets which have all been plotted with respect to surface-normal supercell dimension. These datasets may have a variety of ratios of slab to vacuum thickness. For example, the Au{111} dataset consists only of the  $n_s + 7$  dataset (vacuum thickness was constant and only slab thickness was varied). In contrast, for Ag{100} a mixture of

the  $n_s + 8$  and  $23 + n_v$  datasets were plotted. The latter datapoints were observed to have larger error bars at higher vacuum thickness. Similarly in the figure obtained for Ag{110}, the first nine datapoints are the  $n_s + 12$  series and the last three the  $33 + n_v$  data series. The latter three datapoints have much larger error bars, as well as large vacuum thickness. Likewise for Cu{100}, the third and the last three datapoints are in the  $23 + n_v$  series and have much larger error bars than the other datapoints, which are in the  $n_s + 8$  series.

Implicit in the choice of plotting Fig. 3.18 as a function of surface-normal dimension rather than making separate graphs of convergence with  $n_s$  and  $n_v$  is an assumption that increasing  $n_s$  or  $n_v$  by the same amount will be equivalent. As the previous paragraph mentioned that the amount of vacuum had an effect on the spread for different smearing widths, this may not be the case. The effect of adding a layer of vacuum may be different from the effect of adding a layer of slab. Also, if the effect of adding a layer of vacuum is not equivalent to adding a layer of slab, then  $n_s$  and  $n_v$  may or may not be independent of each other. In other words, the convergence with slab thickness may be dependent on what the vacuum thickness is. It appears based on the results for Pd{110} that slab and vacuum thickness cannot be decoupled. Based on this, it is necessary to vary both together in order to reach a meaningful converged denominator. However, it is worth checking if the convergence is conditional on the ratio of slab to vacuum thickness.

### 3.3.3 Varying ratio of slab to vacuum thickness

Figure 3.20 shows the convergence of Pd{110} and Au{111} for three different series with different ratios of slab to vacuum thickness. In Fig. 3.20 there is a difference between the convergence for Au{111} and Pd{110}. The former appears to converge absolutely to about -0.5 eV regardless of the choice of ratio. In comparison, the convergence of Pd{110} is conditional on the ratio of slab to vacuum thickness. As in Fig. 3.18, the error bars show the standard deviation and are a measure of the uncertainty due to the choice of smearing width. As was previously observed in Fig. 3.18, these error bars

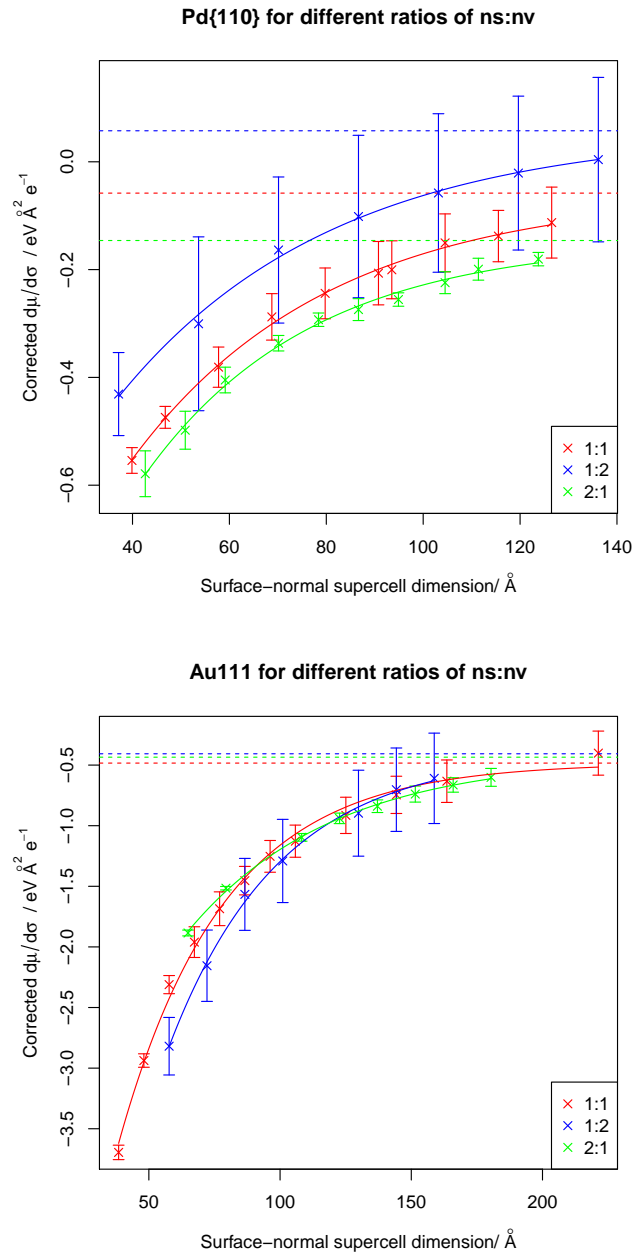


**Figure 3.20:** Comparison of convergence with different ratios of slab to vacuum thickness for Pd{110} and Au{111}. The cross-correlation of the DOS was calculated using a Fermi-Dirac function at the Fermi level.

are larger for larger vacuum thickness.

The difference between the two metals might be due to gold being a coinage metal with low DOS at the Fermi level, whereas palladium is a transition metal with higher DOS at the Fermi level. The correction method involved cross-correlation of the occupied DOS. This should be the same shape for states well below the Fermi level, and will simply be shifted rigidly. However, close to the Fermi level there may be a small change in shape of the DOS with increased charge. This means that the cross-correlation may leave some dependence on the potential. This would have more of an effect where the DOS at the Fermi level is higher. In order to test this hypothesis, it would be helpful to plot the fixed-broadening DOS for a transition metal and a coinage metal and see how these are aligned using the cross-correlation method. Also it would be interesting to compare how well aligned the curves are based on where the DOS is shifted based on a cross-correlation over a DOS region below the Fermi level or for a DOS region substantially lower in energy than the Fermi level. This was investigated in Section 3.3.4.

### 3.3.4 Varying the DOS range for cross-correlation

Figures 3.21-3.22 show the DOS for Au{111} and Pd{110} as shifted by the cross-correlation of the whole occupied DOS. This cross-correlation was done after the DOS was multiplied by a Fermi-Dirac function with a width of 2.2 eV, positioned at the Fermi level. In Fig. 3.21 the graphs for positive and negative charge are well aligned by the cross-correlation of the DOS below the Fermi level. Even in Fig. 3.21 d the two curves are almost completely superimposed. As Au is a coinage metal, the DOS at the Fermi level is low (see Fig. 3.21 a). This means that the region close to the Fermi level will have a small effect on the cross-correlation. This might be one reason that the lower edge of the DOS is so well aligned.

In contrast, in Fig. 3.22 a it can be seen that the DOS at the Fermi level is high for Pd{110}. Palladium is a transition metal and the Fermi level lies in the d band. This means that if the region for the cross-correlation is the

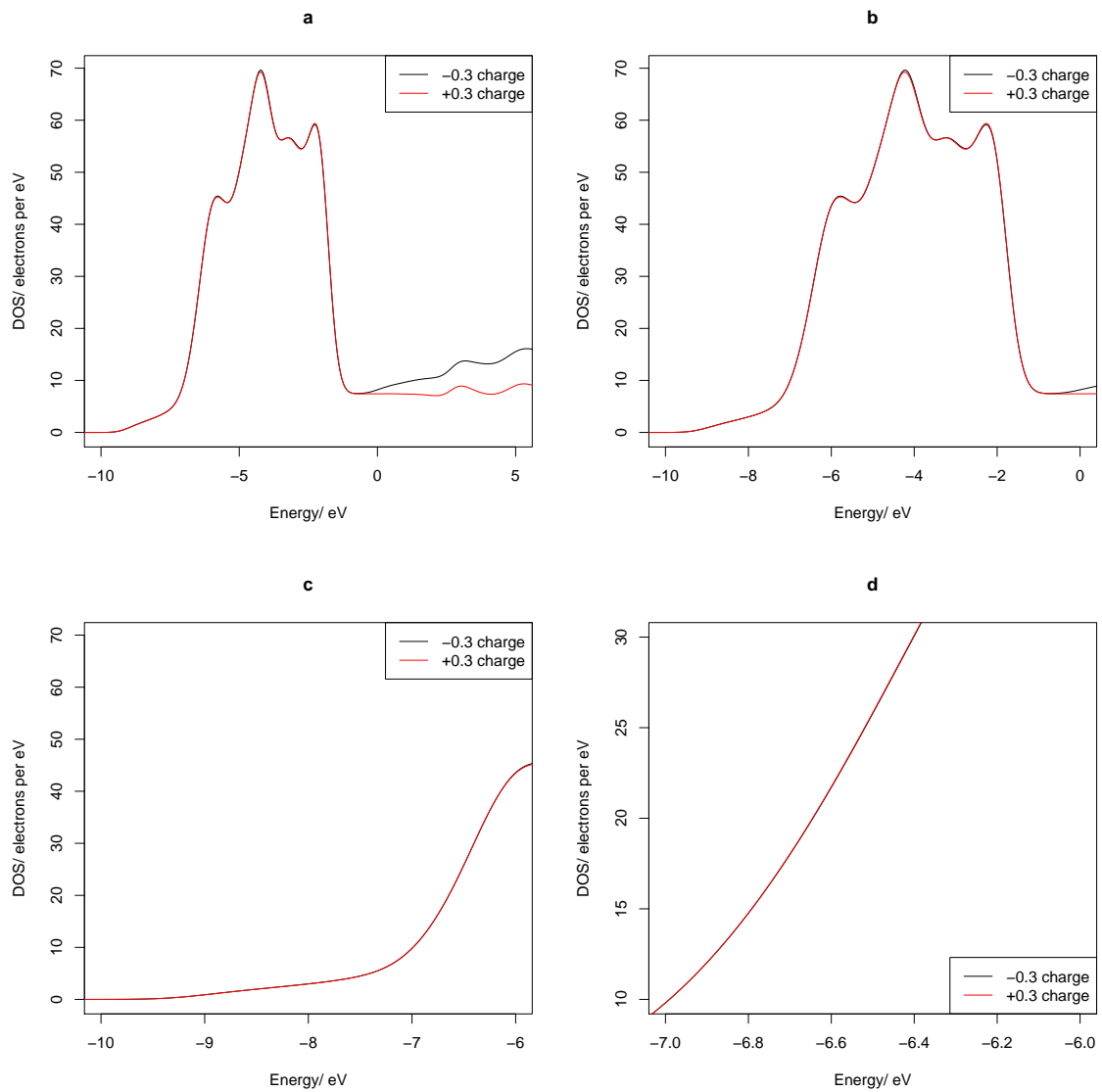


**Figure 3.21:** Graphs of the DOS for Au{111} for positive and negative charge, shifted by the energy corresponding to the maximum in the cross-correlation over the whole occupied DOS. The graphs are shifted so that the average of the negative and positive Fermi levels is zero. Panels a-d show progressively more zoomed-in versions of the same data.

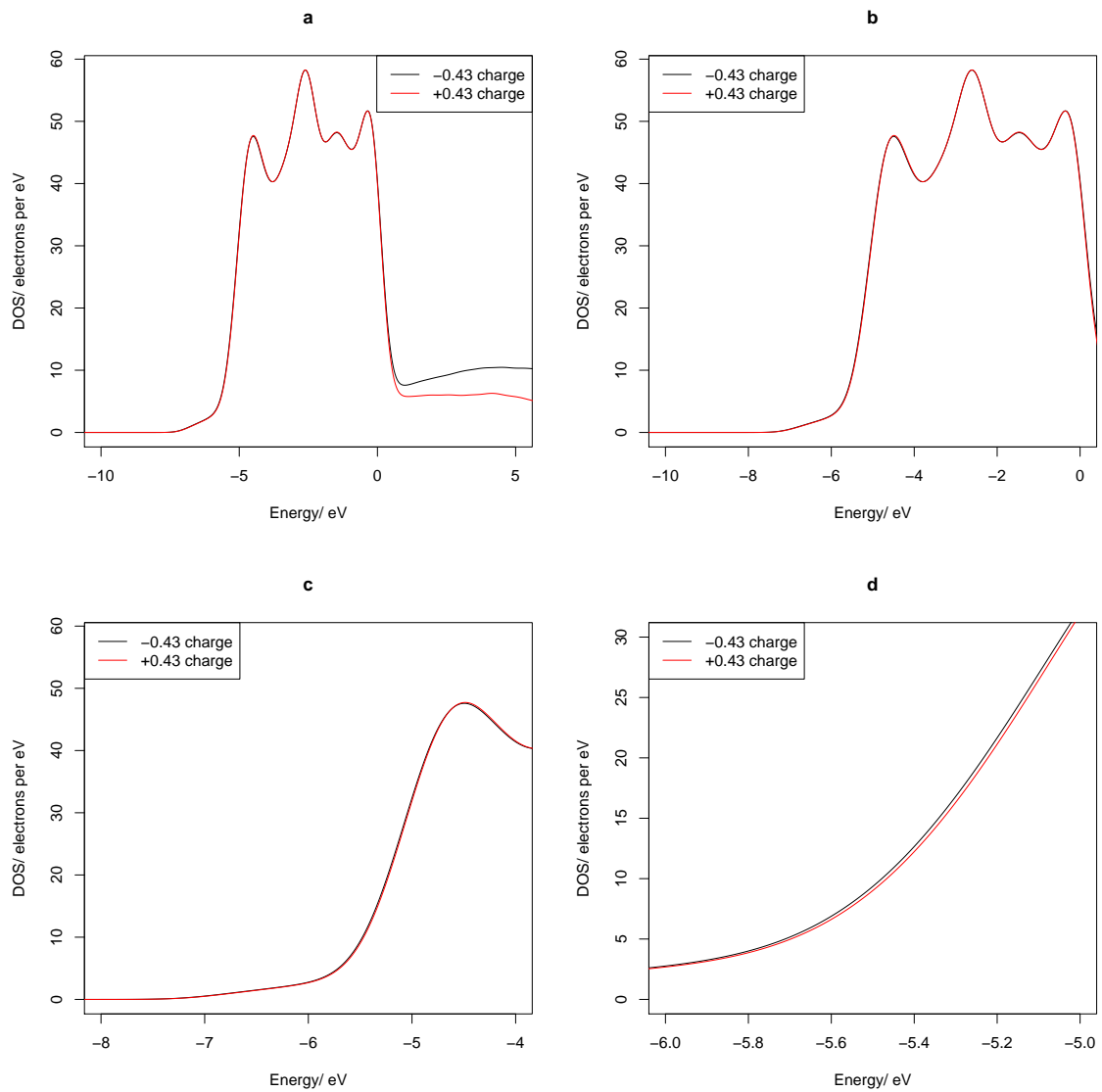


**Figure 3.22:** Graphs of the DOS for Pd{110} for positive and negative charge, shifted by the energy corresponding to the maximum in the cross-correlation over the whole occupied DOS. The graphs are shifted so that the average of the negative and positive Fermi levels is zero. Panels a-d show progressively more zoomed-in versions of the same data.

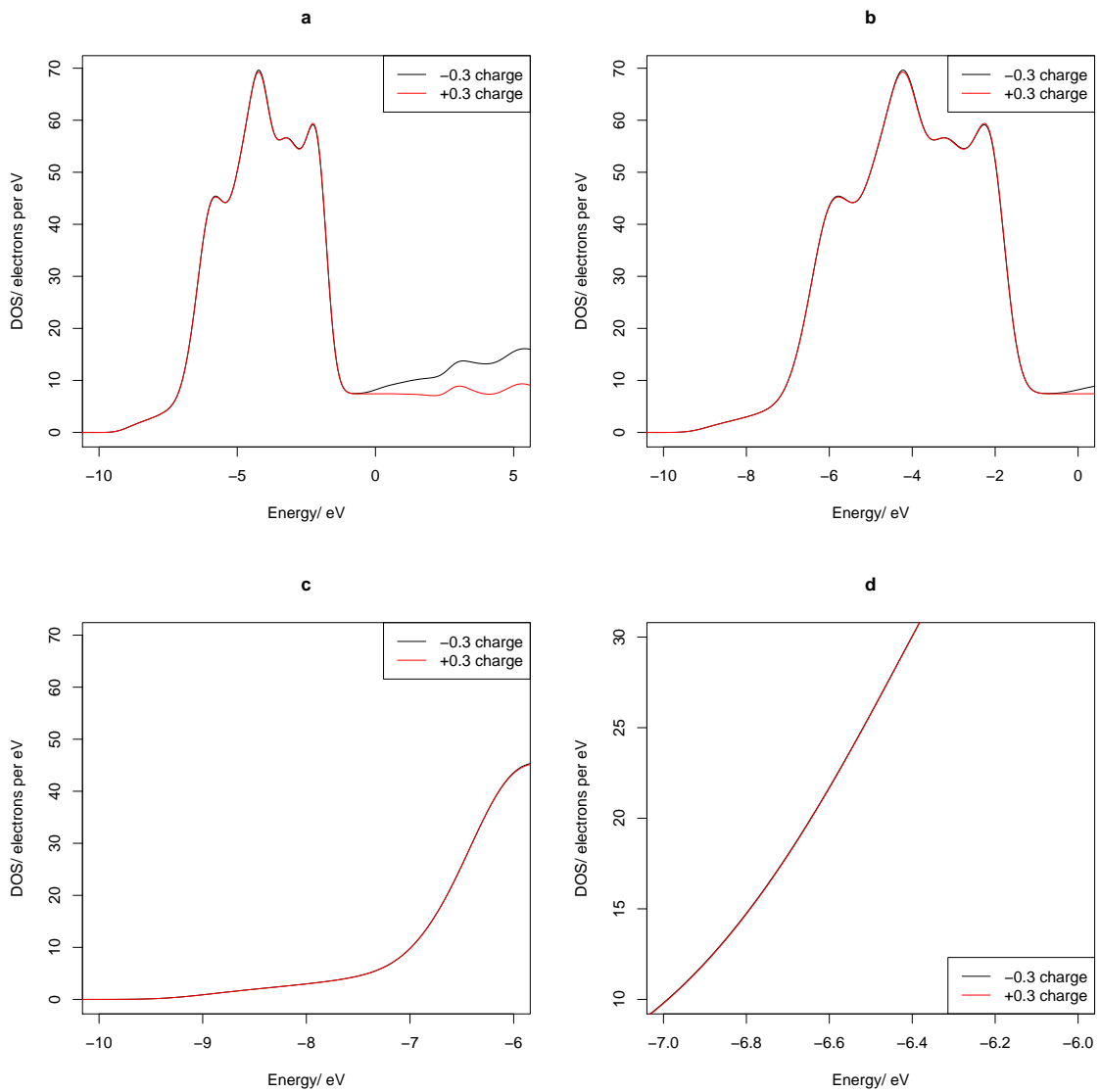


**Figure 3.23:** Graphs of the DOS for Au{111} for positive and negative charge, shifted by the energy corresponding to the maximum in the cross-correlation over the lowest 5 eV of the DOS. The graphs are shifted so that the average of the negative and positive Fermi levels is zero. Panels a-d show progressively more zoomed-in versions of the same data.

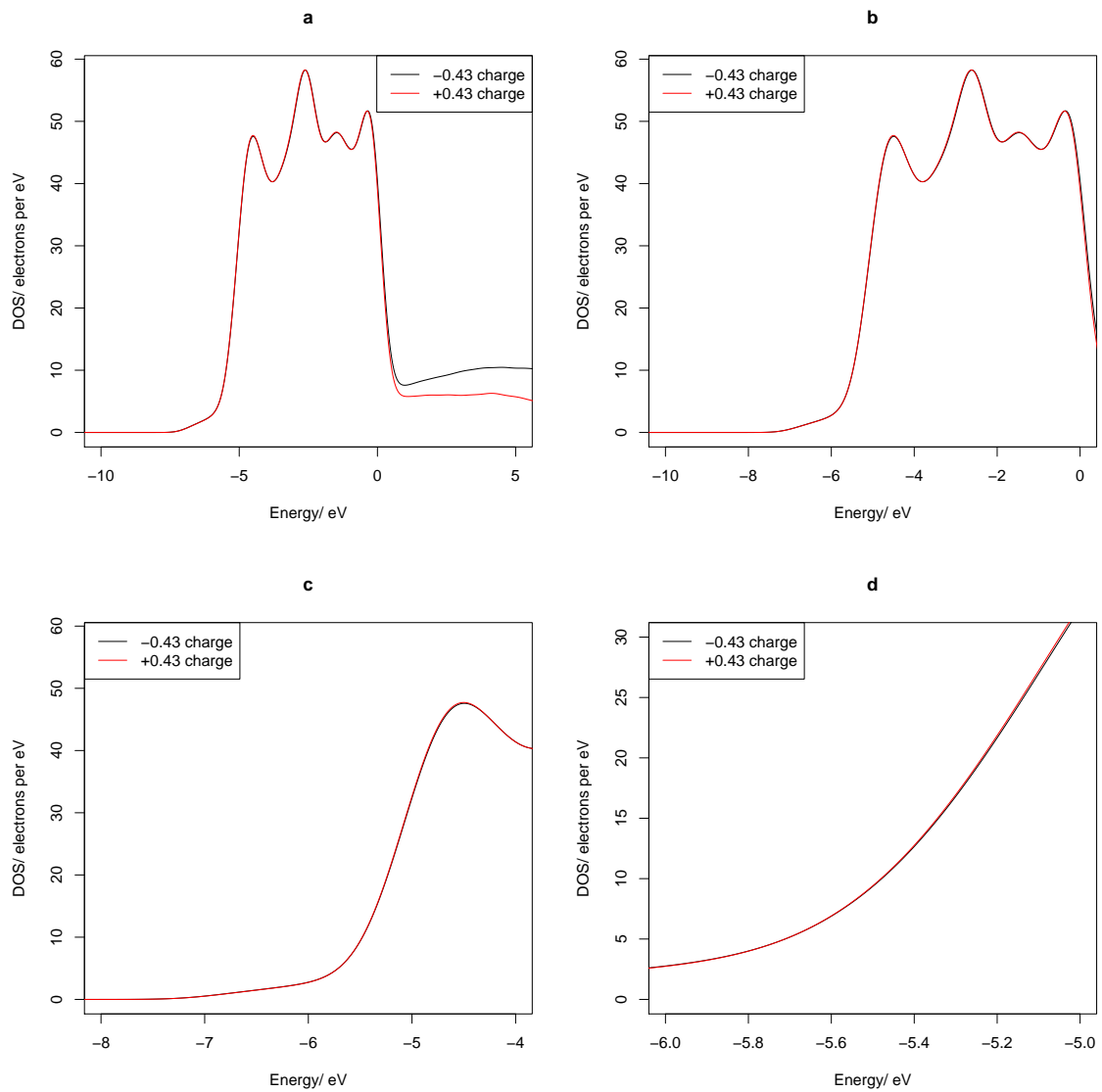


**Figure 3.24:** Graphs of the DOS for Pd{110} for positive and negative charge, shifted by the energy corresponding to the maximum in the cross-correlation over the lowest 5 eV of the DOS. The graphs are shifted so that the average of the negative and positive Fermi levels is zero. Panels a-d show progressively more zoomed-in versions of the same data.

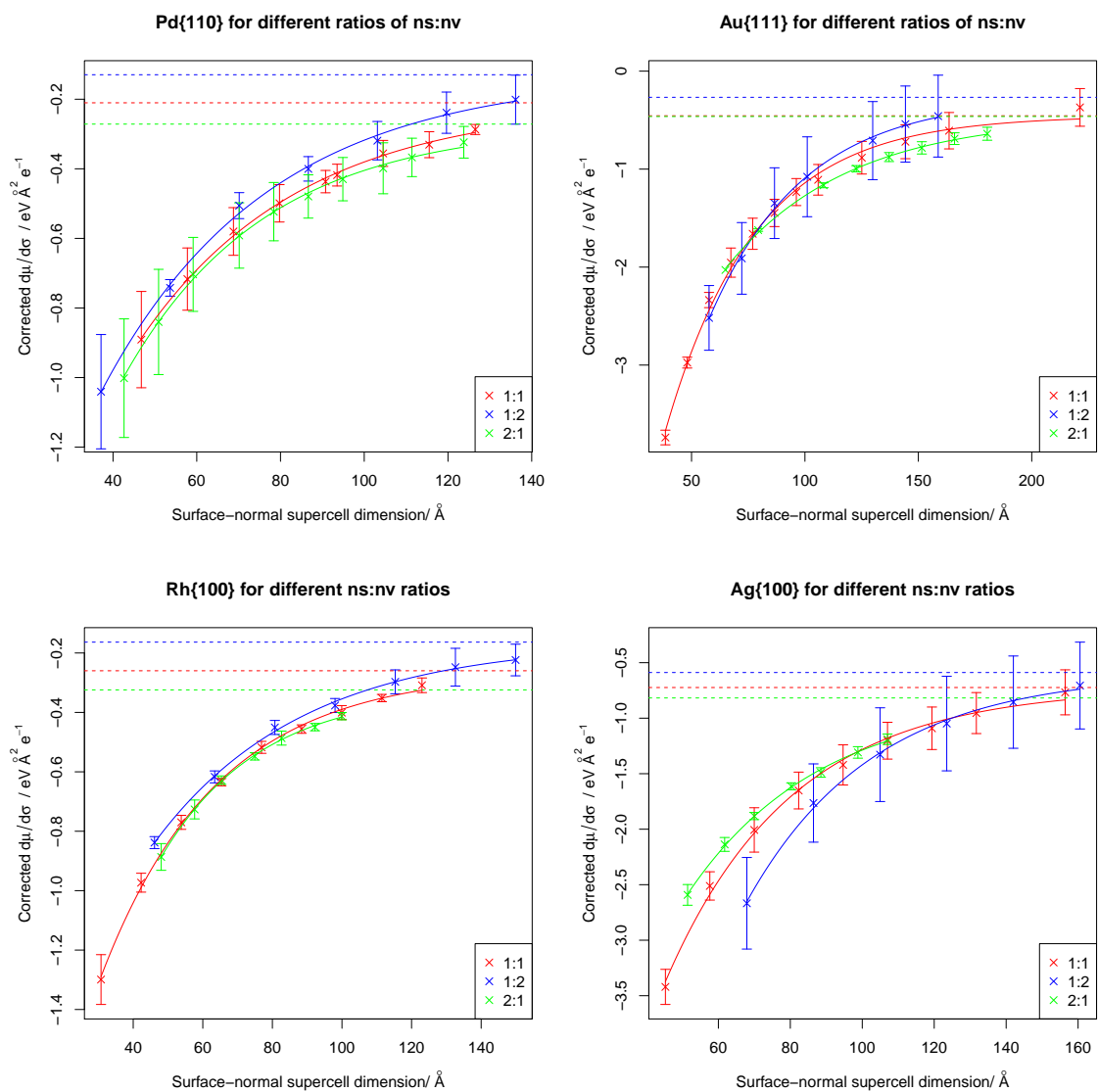


**Figure 3.25:** Comparison of convergence with different ratios of slab to vacuum thickness for four different metals. Correction method involved cross-correlation over the lowest 5 eV of the DOS.

whole of the occupied d band then the region close to the Fermi level will have a large effect on the cross-correlation. The effect of this can be seen in Fig. 3.22 d, which shows that the lower band edge is not very well aligned by cross-correlation over the whole occupied DOS. There are two ways in which the DOS will change when the charge is varied. First, there will be a change in Fermi level and some states near the Fermi level will change. Second, the whole DOS will be rigidly shifted due to the change in potential. For coinage metals, the DOS close to the Fermi level was different for different charge, but the DOS close to the Fermi level was small so these differences did not affect the cross-correlation much. However, for transition metals the DOS at the Fermi level is higher and the DOS close to the Fermi level is more different. This affects the value of the denominator.

As the DOS close to the Fermi level changes with different charge, it would be better to perform the cross-correlation over a region of the DOS that is well below the Fermi level. I tried using a Fermi-Dirac function that instead of being positioned at the Fermi level, was instead positioned 5 eV above the lowest energy band. The results for Au and Pd can be seen in Fig. 3.23 and Fig. 3.24 respectively. Figure 3.23 is very similar to Fig. 3.21. In Fig. 3.23 d the curves are well aligned. However, the effect of moving the Fermi-Dirac function to 5 eV above the lowest energy band is more pronounced for Palladium as it is a transition metal. In Fig. 3.24 the DOS are well aligned even in the close up in Fig. 3.24 d. Therefore, shifting the position of the Fermi-Dirac function improves the performance of the cross-correlation for transition metals. Based on this, it is best to position the Fermi-Dirac function 5 eV above the lowest band energy rather than at the Fermi level, especially for transition metals. As a result, this method was used from here on.

Figure 3.25 shows the convergence with the surface-normal supercell dimension of the denominator. The denominator was corrected using the cross-correlation of the DOS up to 5 eV above the lowest band energy. The results are somewhat similar to those obtained by cross-correlation over the whole DOS, which are shown in Fig. 3.20. There are similar trends, in that the

denominator is less negative for larger vacuum thickness. Also the error bars are larger for larger vacuum thickness. However, the extrapolated value of the denominator is always negative in Fig. 3.25, whereas for Fig. 3.20 it is positive for the 1:2 ratio of Pd{110}. A negative value of the denominator corresponds with a positive value of the local softness and is more physically reasonable. Also there is less variation between different ratios for Pd{110} in Fig. 3.25 than in Fig. 3.20. Overall, the cross-correlation over a restricted range of the DOS seems to lead to better results compared with using the whole occupied DOS. Therefore this approach was used for the rest of the surfaces considered in this thesis.

It should be noted that even with the new location of the Fermi-Dirac function, the converged value of the denominator of local softness still varies in response to a change in the ratio of slab to vacuum. This result is disappointing as it shows that rather than being absolutely convergent, the denominator of local softness is conditionally convergent on the composition of the supercell. In order to have a consistent way of defining the denominator of local softness it would be helpful to have a standard choice of slab to vacuum ratio. An arbitrary choice of a 1:1 slab to vacuum ratio was made, and this was used for all the following results.

### 3.4 Denominator convergence for eighteen metal surfaces

Figures 3.26, 3.27 and 3.28 show the convergence of the corrected denominator with surface-normal supercell dimension  $c$  for 18 different metal surfaces. As mentioned above, this was carried out for a 1:1 slab to vacuum ratio. All the graphs show an exponential trend where the corrected denominator of the local softness approaches a constant negative value. In comparison to previous methods of correcting the denominator of local softness, this method results in less numerical noise. There seems to be a trend where as the metal becomes more reactive the denominator becomes a smaller, less negative, number. Table 3.1 shows the parameters which were used for the

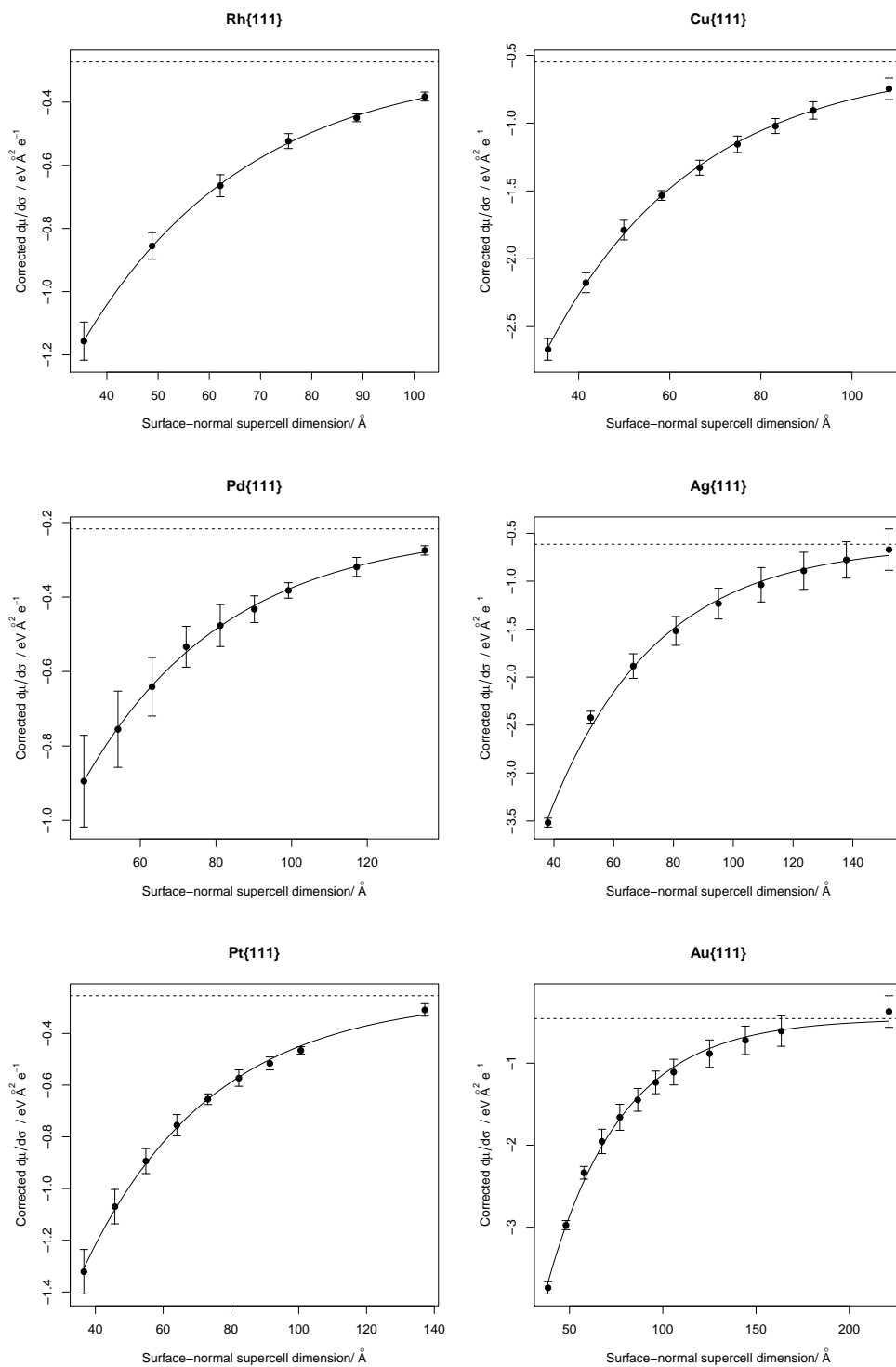


**Figure 3.26:** Comparison of denominator convergence for {111} surfaces of different metals. A constant 1:1 slab to vacuum ratio was used.

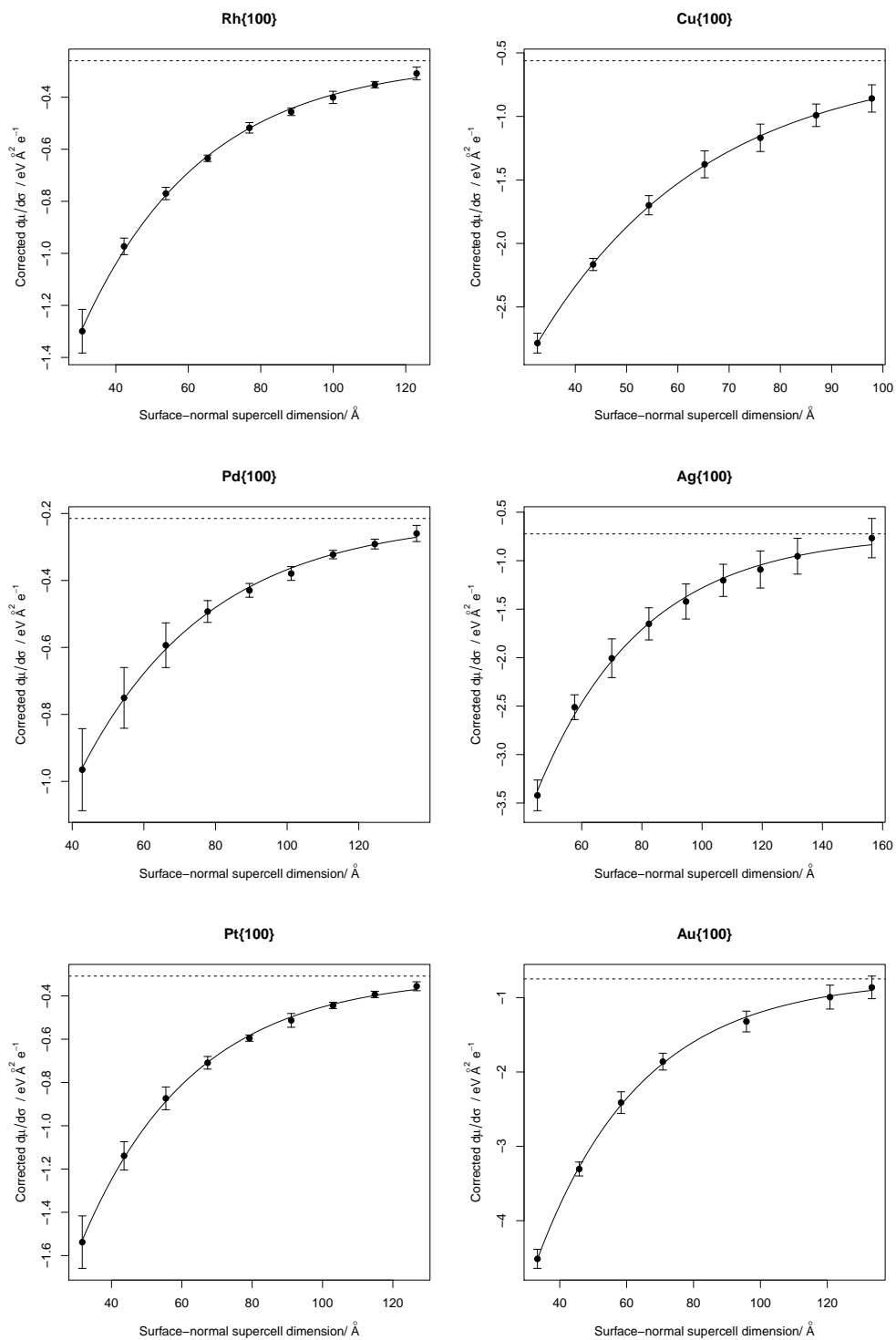


**Figure 3.27:** Comparison of denominator convergence for {100} surfaces of different metals. A constant 1:1 slab to vacuum ratio was used.

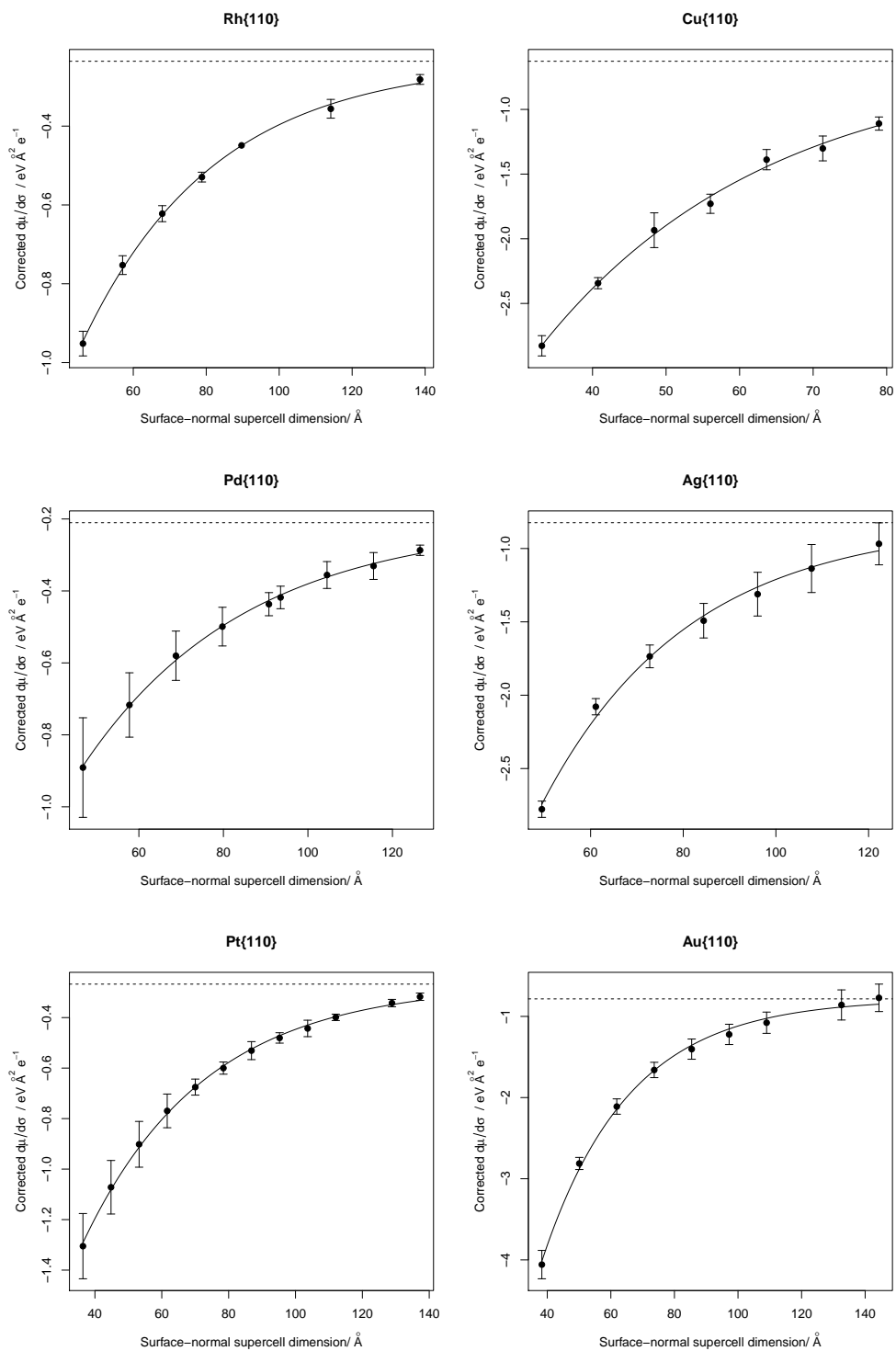


**Figure 3.28:** Comparison of denominator convergence for {110} surfaces of different metals. A constant 1:1 slab to vacuum ratio was used.

fitted curves in Figs. 3.26, 3.27 and 3.28. The table shows a smaller magnitude of fitted parameter  $A$  for the three transition metals compared with the coinage metals. This makes sense as the local softness is inversely proportional to the denominator of local softness. Therefore if the numerator of local softness remains constant, as the denominator becomes smaller, the local softness would become larger.

Surface	$A / \text{eV } \text{\AA}^2 e^{-1}$	$B / \text{eV } \text{\AA}^2 e^{-1}$	$k / \text{\AA}^{-1}$
Rh{111}	-0.273	-2.65	-0.0309
Rh{100}	-0.260	-2.58	-0.0299
Rh{110}	-0.235	-2.54	-0.0276
Pd{111}	-0.217	-2.24	-0.0265
Pd{100}	-0.215	-2.44	-0.0277
Pd{110}	-0.210	-2.28	-0.0259
Pt{111}	-0.254	-2.77	-0.0265
Pt{100}	-0.308	-3.30	-0.0314
Pt{110}	-0.267	-2.78	-0.0274
Cu{111}	-0.549	-5.80	-0.0305
Cu{100}	-0.562	-6.00	-0.0305
Cu{110}	-0.628	-6.43	-0.0324
Ag{111}	-0.615	-8.26	-0.0280
Ag{100}	-0.724	-9.62	-0.0285
Ag{110}	-0.824	-9.21	-0.0317
Au{111}	-0.456	-8.46	-0.0251
Au{100}	-0.748	-10.9	-0.0319
Au{110}	-0.784	-13.2	-0.0368

**Table 3.1:** Table of parameters fitted to the  $A + B \exp(kc)$  exponential curves shown in Figs. 3.26, 3.27 and 3.28. The value of fitted parameter  $A$  was used as the converged value of the denominator of local softness.

### 3.5 Summary

It was established in Section 3.1 that there are two problems with the chemical potential and other energies as outputted by CASTEP. Firstly, energies are reported relative to the supercell average potential, which will vary with supercell size and composition. Secondly, there is a problem with CASTEP adding a compensatory potential to help the charged calculations converge,

and that this potential affects the energies. Several approaches of correcting for the change in reference energy were considered in Sections 3.2 and 3.3.

In Section 3.2, the method of subtracting the slab average potential was investigated. This method worked relatively well but had several issues. There was a lot of numerical noise and also there were problems with Friedel oscillations in the average potential along the surface-normal dimension. This made it difficult to define a consistent region of space over which to calculate the slab average potential. As there were several drawbacks to the slab average potential method, a different method of correcting the chemical potential was needed. By cross-correlating the DOS below the Fermi level obtained for positive and negative charge, the shift in energy due to the change in charge can be found. This method was evaluated in Section 3.3. Several variants of the method were investigated in order to generate the DOS, and it was concluded that the best results were found using OptaDOS with fixed broadening.

The cross-correlation of the occupied DOS was calculated after multiplying the DOS by a Fermi-Dirac function. Initially this Fermi-Dirac function was located at the Fermi level, which worked well for coinage metals but less well for transition metals. This was due to transition metals having a higher DOS at the Fermi level. Positioning the Fermi-Dirac function 5 eV above the lowest energy band was found to improve the cross-correlation. Therefore this method was used to correct for the change in reference energy with different charge and supercell geometry. Once the change in reference energy was corrected, the denominator of local softness could be calculated for a range of supercell dimensions, and extrapolated to infinite supercell dimensions.

This extrapolation to infinite supercell dimensions was initially done based on an assumption that adding a layer of slab would be equivalent to adding a layer of vacuum. This was found to be a reasonable assumption for coinage metals but not for transition metals. Datasets with different ratios of slab to vacuum converged to slightly different values for large surface-normal supercell dimension. The convergence was not absolute but was conditional on

the ratio of slab to vacuum thickness. To avoid this conditionality, it was decided to standardise upon an arbitrarily chosen ratio of 1:1 for all subsequent calculations. This approach was used to calculate the denominator of local softness for eighteen different metal surfaces in Section 3.4. An exponential  $A + B \exp(kc)$  was used to fit the data and the resulting converged values of the denominator of local softness, fitted parameter  $A$ , are summarised in Table 3.1. These values of the converged denominator of local softness were then used to calculate the local softness, which will be discussed in the next chapter.

## Chapter 4

# Visualising the Local Softness of Clean Metal Surfaces

Using the methods described in Section 2.9 and Section 2.10.5, the numerator and denominator of local softness were calculated for a range of copper and other surfaces. Isosurfaces of the local softness were plotted for three copper surfaces using Jmol: an open-source java viewer for chemical structures in three dimensions. <http://www.jmol.org/> The threshold values for the positive and negative isosurfaces were  $+0.75$  and  $-0.075 \text{ eV}^{-1} \text{ \AA}^{-3}$  respectively. The shape of the positive and negative isosurfaces of local softness was then compared. This analysis can be found in Section 4.1. Isosurfaces were also plotted of the local softness with an isosurface threshold of  $0.6 \text{ eV}^{-1} \text{ \AA}^{-3}$  in order to display the regions of large local softness. Isosurfaces were compared for three different copper surfaces, the  $\{111\}$ ,  $\{100\}$  and  $\{110\}$ . These surfaces are all relatively low index. Based on the analysis by Pratt and Jenkins they can be categorised as flat (two or more close-packed rows in the top layer) or stepped (one close-packed row in the top layer).<sup>96</sup> Based on this analysis the  $\{100\}$  and  $\{111\}$  surfaces are flat and the  $\{110\}$  surface is stepped.

Isosurfaces are a good way of obtaining insight into the shape of regions of space above a given value of the local softness. However, they are restricted

to a particular threshold value so do not give information about the range of values of the local softness in space. It is not easy to make a volume-filling three-dimensional view, so it seems sensible to plot values of the local softness on a two-dimensional surface. A sensible choice of a two-dimensional surface might be an isosurface of constant electron density. This then raises the question of what threshold to plot the electron density isosurface for. This is by nature an arbitrary choice, but some fraction of the bulk valence-electron density would be a reasonable choice, as it would vary proportionately when going from one metal to another. What fraction to use is another relatively arbitrary decision. Having tried several fractions of the bulk valence-electron density,  $1/3$  and  $1/5$  fractions of the bulk valence-electron density seemed to look good, so these were chosen for the following colourplots, which will be analysed in Section 4.2. However, for the moment, let us return to isosurfaces of the local softness itself, which will be discussed in Section 4.1.

## 4.1 Isosurfaces of local softness for copper

### 4.1.1 Cu{100}

Figures 4.1 and 4.2 show isosurfaces of the local softness of Cu{100} plotted with threshold values of  $+0.75$  and  $-0.075 \text{ eV}^{-1} \text{ \AA}^{-3}$ . In these figures the regions of large positive values of local softness are centred above the top layer of atoms. It is important to bear in mind that the isosurfaces of the positive and negative local softness have a threshold that differs by an order of magnitude. Therefore, although the positive and negative isosurfaces appear to contain a similar volume of space, in fact the regions of positive local softness contain values that are an order of magnitude larger.

Positive local softness implies a region where electrons accumulate in response to an overall increase in chemical potential. Negative local softness indicates a region where electrons are depleted in response to an overall increase in chemical potential. Therefore in most regions the electrons accumulate in response to a global increase in  $\mu$ . There are clearly defined, roughly p-orbital-shaped regions centred roughly on the atoms where electrons are depleted in

response to a global increase in  $\mu$ . The regions of large positive local softness are centred above the top layer of atoms. Their shape is roughly that of an oblate spheroid, with more flattening on the surface closer to the atoms. The regions of maximum local softness appear to be situated quite far from the atom centres. However, comparison with Fig. 4.4 makes it clear that in fact the regions of maximum local softness are centred only just above the atoms when the atoms are visualised at a touching-sphere radius.

Figures 4.3 and 4.4 show the local softness of Cu{100} with an isosurface threshold of  $0.6 \text{ eV}^{-1} \text{ \AA}^{-3}$ . In these diagrams the atoms were rendered at a touching-sphere radius. At the isosurface setting of  $0.6 \text{ eV}^{-1} \text{ \AA}^{-3}$  and  $-0.6 \text{ eV}^{-1} \text{ \AA}^{-3}$ , only the positive local softness isosurface would be visible at either of the atomic radius settings considered. Therefore only the positive local softness isosurface was plotted. In Fig. 4.3 it appears that regions of maximum local softness have a roughly square shape when viewed from above the surface. It seems that regions of higher local softness run along rows of close-packed atoms in the top layer of the Cu{100} surface. Figure 4.4 allows the shape of the side-section through the local softness isosurface to be evaluated. It would seem that the surface-normal cross-section of the local softness at this isosurface is similar to that at the higher threshold value of  $0.75 \text{ eV}^{-1} \text{ \AA}^{-3}$ . Predictions can be made from this study for soft adsorbates on Cu{100} where the governing effect was electronic. These, based on this study, would be predicted to adsorb preferentially on atop sites on the top layer of the Cu{100} surface. After this the preference would be probably for the bridge sites along close-packed rows. This could be tested using a range of experimental techniques, including STM and LEED.

### 4.1.2 Cu{111}

In Figs. 4.5 and 4.6 the local softness is shown as isosurfaces with a threshold of  $0.75 \text{ eV}^{-1} \text{ \AA}^{-3}$  and  $-0.075 \text{ eV}^{-1} \text{ \AA}^{-3}$ . The regions of positive local softness are oblate-spheroid shapes centred above the top-layer atoms. The regions of negative local softness are have a roughly p-orbital shape centred on top-layer atoms. Viewed from above, these regions of negative local softness have

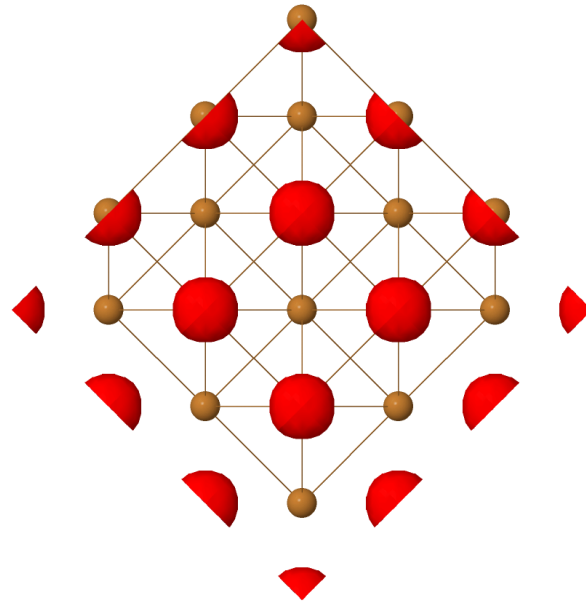


**Figure 4.1:** Isosurface plot of local softness for the Cu{100} surface viewed from above. Positive isosurface is red with a threshold of  $0.75 \text{ eV}^{-1} \text{ \AA}^{-3}$ . Negative isosurface is blue with a threshold of  $-0.075 \text{ eV}^{-1} \text{ \AA}^{-3}$ .

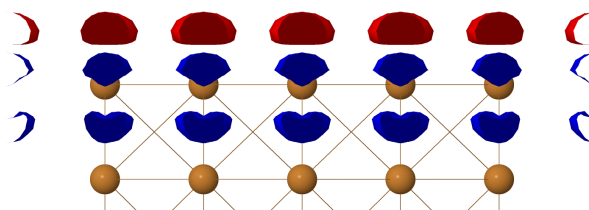


**Figure 4.2:** Isosurface plot of local softness for the surface viewed from the side. Isosurface colours and threshold values as for Fig. 4.1.

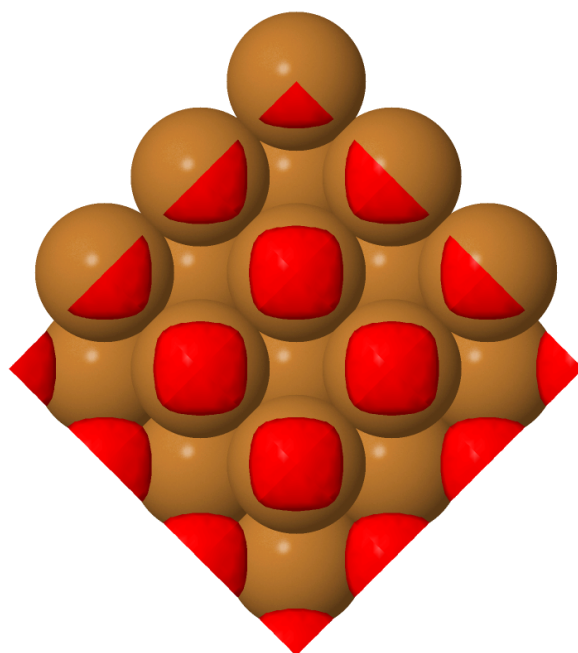


**Figure 4.3:** Isosurface plot of local softness for the Cu{100} surface viewed from above. Isosurface has a threshold of  $0.6 \text{ eV}^{-1} \text{ \AA}^{-3}$

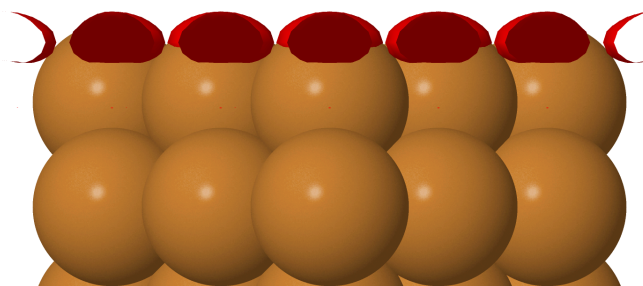


**Figure 4.4:** Isosurface plot of local softness for the surface viewed from the side. Isosurface has a threshold of  $0.6 \text{ eV}^{-1} \text{ \AA}^{-3}$ .

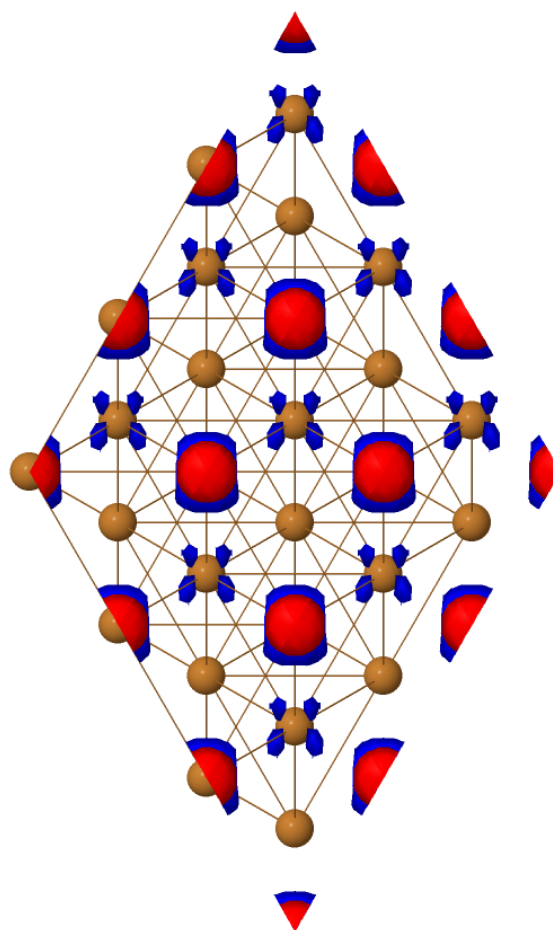


**Figure 4.5:** Isosurface plot showing the local softness for the Cu{111} surface viewed from above. Positive isosurface is red with a threshold of  $0.75 \text{ eV}^{-1} \text{ \AA}^{-3}$ . Negative isosurface is blue with a threshold of  $-0.075 \text{ eV}^{-1} \text{ \AA}^{-3}$ .

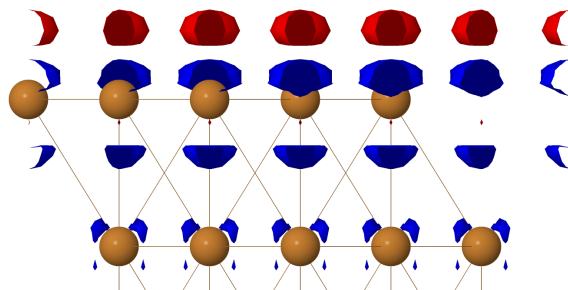


**Figure 4.6:** Isosurface plot showing the local softness for the surface viewed from the side. Isosurface colours and threshold as for Fig. 4.5.

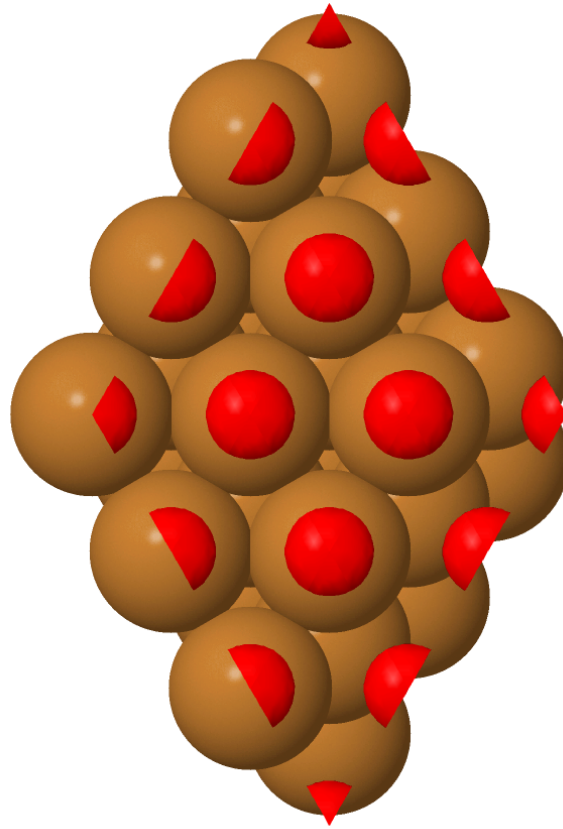


**Figure 4.7:** Isosurface plot of local softness for the Cu{111} surface viewed from above. Isosurface has a threshold of  $0.6 \text{ eV}^{-1} \text{ \AA}^{-3}$

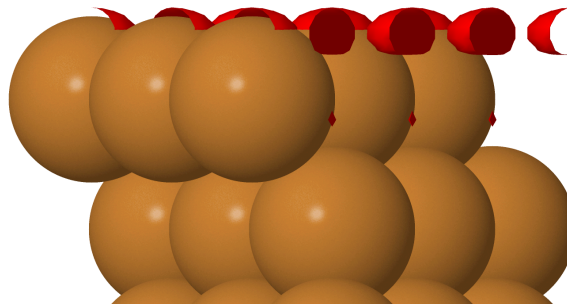


**Figure 4.8:** Isosurface plot of the local softness for the surface viewed from the side. Isosurface threshold as for Fig. 4.7.

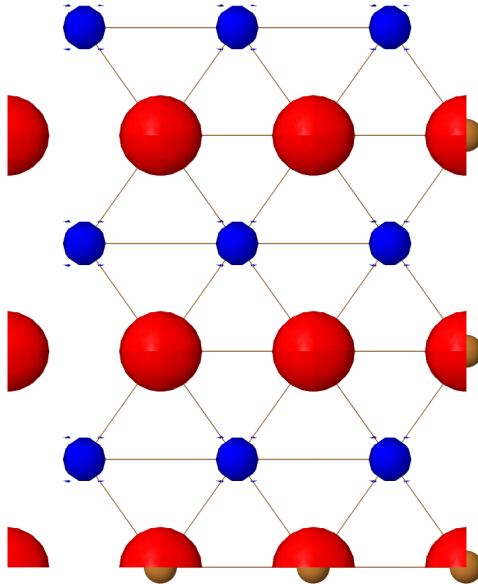


**Figure 4.9:** Isosurface plot showing the local softness for the Cu{110} surface viewed from above. Positive isosurface is red with a threshold of  $0.75 \text{ eV}^{-1} \text{ \AA}^{-3}$ . Negative isosurface is blue with a threshold of  $-0.075 \text{ eV}^{-1} \text{ \AA}^{-3}$ .

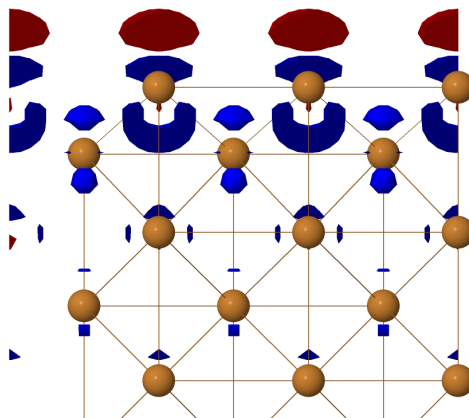


**Figure 4.10:** Isosurface plot showing the local softness for the surface viewed from the side. Isosurface threshold as for Fig. 4.9.

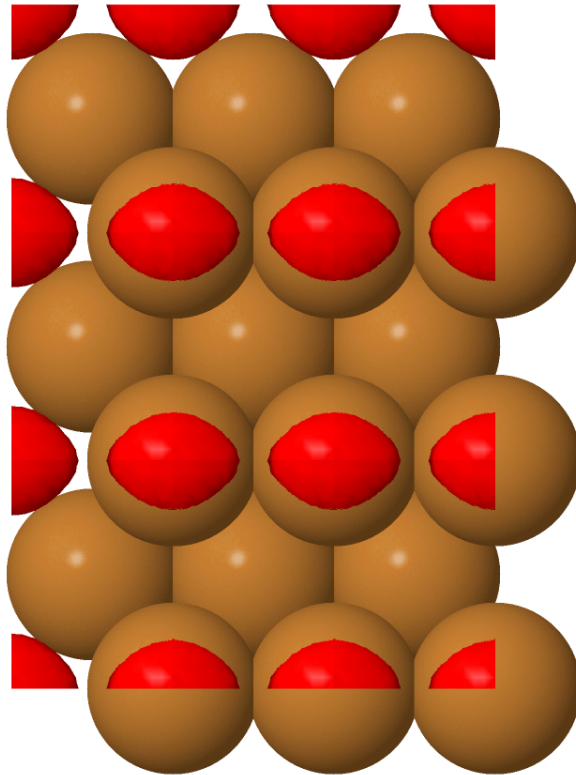


**Figure 4.11:** Isosurface plot of local softness for the Cu{110} surface viewed from above. Isosurface has a threshold of  $0.6 \text{ eV}^{-1} \text{ \AA}^{-3}$

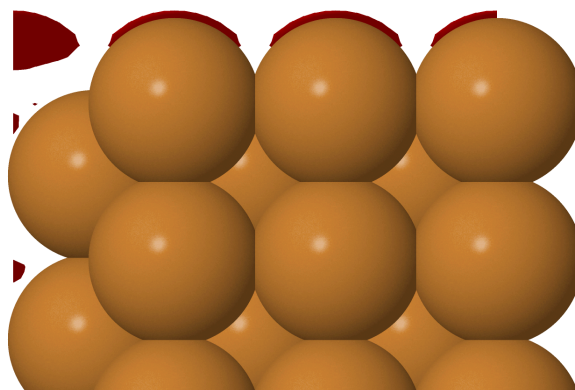


**Figure 4.12:** Isosurface plot of the local softness for the surface viewed from the side. Isosurface threshold as for Fig. 4.11.

a roughly rectangular shape. This is surprising as it breaks the three-fold symmetry of the surface. On the next layer down there are smaller regions of negative local softness, which have a roughly d-orbital shape, centred above second-layer atoms.

The threshold is an order of magnitude smaller for the negative isosurface compared to the positive isosurface. This allows the relative size of regions of positive and negative local softness to be compared. For the  $\{111\}$  surface, unlike the  $\{100\}$ , the regions of negative local softness at a threshold of  $-0.075 \text{ eV}^{-1} \text{ \AA}^{-3}$  are larger than the regions of positive local softness at a threshold of  $0.75 \text{ eV}^{-1} \text{ \AA}^{-3}$ . This was not the case for the  $\{100\}$  surface or the  $\{110\}$  surface, and is probably a measure of the softness being lower for  $\{111\}$  than for the other surfaces.

The positive isosurface with threshold of  $0.75 \text{ eV}^{-1} \text{ \AA}^{-3}$  for  $\text{Cu}\{111\}$  fills slightly less volume than for the  $\text{Cu}\{100\}$  surface at the same threshold. The fact that the regions of high positive local softness are larger for  $\text{Cu}\{100\}$  suggests that the local softness is larger for  $\text{Cu}\{100\}$  than for  $\text{Cu}\{111\}$ . In Chapter 5 the softness of individual atoms on the surfaces were compared in Table 5.3, and this was found to be the case. Figures 4.7 and 4.8 show the local softness at a threshold of  $0.6 \text{ eV}^{-1} \text{ \AA}^{-3}$ . For these diagrams, atoms were rendered using a touching-sphere radius. As for the higher threshold, the regions of positive local softness are roughly oblate-spheroid and centred above top-layer atoms. At this threshold the regions of high positive local softness are smaller than those for the  $\{100\}$  surface, which take larger values along close-packed rows. This is in keeping with the greater atomic softness for the  $\{100\}$  surface as opposed to the  $\{111\}$  surface (see Chapter 5).

### 4.1.3 $\text{Cu}\{110\}$

Figures 4.9 and 4.10 show the local softness isosurfaces of threshold  $0.75 \text{ eV}^{-1} \text{ \AA}^{-3}$  and  $-0.075 \text{ eV}^{-1} \text{ \AA}^{-3}$ . The regions of positive local softness above  $0.75 \text{ eV}^{-1} \text{ \AA}^{-3}$  form oblate-spheroid shapes above the step-edge atoms. This is similar behaviour to that found for the same threshold on the  $\text{Cu}\{100\}$  surface, but the

volume of space bounded by the isosurface is slightly larger for the Cu{110} surface. This suggests that the local softness is larger for the Cu{110} surface than for the Cu{100} surface, which is in fact borne out by the softness of individual top-layer atoms, which is compared in Chapter 5.

Viewed from the side, it can be seen that there are also tiny regions of positive local softness below top-layer atoms. The regions of negative local softness form roughly oblate-spheroid shapes above top-layer atoms and banana-shaped regions below the top-layer atoms. This is somewhat similar to the shapes of the negative regions of local softness obtained for the Cu{100} and Cu{111} surfaces. There are also roughly p-orbital-shaped regions of negative local softness centred on second-layer atoms. The isosurface for a lower threshold of  $0.6 \text{ eV}^{-1} \text{ \AA}^{-3}$  is shown in Figs. 4.11 and 4.12. The regions of local softness above  $0.6 \text{ eV}^{-1} \text{ \AA}^{-3}$  form roughly prolate-spheroid shapes centred above top-layer, step-edge atoms. The longest axes of these spheroids are oriented along the close-packed row of the step edge.

It can be predicted based on the local softness that adsorbates would preferentially adsorb atop on step-edge atoms or on the bridge sites along the step edge. The experimentally determined binding site for CO on Cu{110} corresponds with this prediction, as CO binds atop on step-edge atoms, as will be discussed further in Chapter 5.<sup>112</sup>

## 4.2 Colourplots of the local softness for eighteen surfaces

The isosurfaces in Section 4.1.1 give an impression of the shape of regions of high local softness but they are by necessity only plotted at one local softness threshold value. Therefore they do not give much information about the range of values taken by the local softness in three dimensions. Another graphical method of plotting the local softness would be useful, in order to provide some complementary information to the isosurfaces. In order to get an impression of what a molecule would experience when approaching

a surface, it would be interesting to visualise what values the local softness takes upon an isosurface of constant density. This approach was taken and the softness was plotted on density isosurfaces. It was found that the range of softness values was different based on what value of threshold was used for the density isosurface. This could be expected, as at a different density threshold, the density isosurface will cut through different regions of space, which are likely to have different values of the local softness.

In order to plot a top-down view, the colourplot will be clearer if the density isosurface is continuous. Therefore, it is helpful if the density threshold is relatively small, so that the density over the whole of the metal surface is greater than the threshold. Therefore a threshold of  $1/5$  of the bulk valence-electron density was chosen. Colourplots of the local softness plotted on these density isosurfaces and viewed from above are shown in Figs. 4.13-4.15. This approach of making colourplots to illustrate a local reactivity index at various positions on a density isosurface was also used by Huang and co-workers<sup>59</sup>. They used this method to plot their approximate measure of the local softness, the local Fermi softness. The Fermi softness and how it relates to the local softness was discussed earlier in Section 1.8. In their Fig. 2 the authors presented colourplots of the local Fermi softness for  $\{111\}$  facets of Rh, Pd, Pt, Cu, Ag and Au. The colourplots in this work and in the paper by Huang et al have a similar distribution of regions of higher values, which are above the atom centres, and regions of lower values, at the three-fold-hollow sites. This is as might be expected as the Fermi softness is an approximation to the local softness.

At a density threshold of  $1/5$  of the bulk valence-electron density, the density isosurface forms a continuous corrugated surface above the top layer of atoms. In order to look at how the softness changes as a function of depth within a supercell, it is helpful to also plot the density isosurface at a higher threshold. In Figs. 4.16-4.18 the local softness was plotted as a colourmap on a density isosurface with a threshold of  $1/3$  of the bulk valence-electron density. For most of the metal surfaces this results in an isosurface forming a semi-atomistic, continuous network through the cell.

The same colour range of  $-0.1-3.7 \text{ eV}^{-1} \text{ \AA}^{-3}$  was used for all colourplots. The maximum in this range was chosen to be greater than the largest value of the local softness found on any of the density isosurfaces. The minimum was chosen to be lower than the local softness in the middle of the slab, which was in all cases within  $0.1 \text{ eV}^{-1} \text{ \AA}^{-3}$  of zero. Using the same range for all colourplots meant that different metals and facets plotted at different density thresholds could be quantitatively compared. There was a greater range of values of the local softness over the density isosurface with a threshold of  $1/3$  of the bulk valence-electron density compared with the threshold of  $1/5$ . For the maximum values of the local softness along the density isosurface at both thresholds, see Table 4.1. A range of  $-0.1-3.7 \text{ eV}^{-1} \text{ \AA}^{-3}$  contains all the values along the isosurfaces for both density thresholds.

The threshold of  $1/3$  of the bulk valence-electron density resulted in the largest value ( $3.675 \text{ eV}^{-1} \text{ \AA}^{-3}$  for the Pd{110} surface). The minimum values for all isosurfaces were similar irrespective of density threshold, therefore the range was greater for the larger density threshold. This greater range for the local softness at the larger density threshold can be explained in terms of the density isosurface cutting closer to the ion cores, where the local softness can be expected to vary more. As shown in Figs. 4.2, 4.6 and 4.10, there are regions of large positive local softness near the nuclei, so these regions will be cut by a density isosurface that is nearer the centre of the atoms.

### 4.2.1 Top-down views

Top-down views of the local softness mapped onto the density isosurface with a density threshold of  $1/5$  the bulk valence-electron density are shown in Figs. 4.13-4.15. All these figures show an increase in local softness going from the coinage metals to the transition metals. The range of colours for the coinage metals is between dark blue and teal ( $0-1.12 \text{ eV}^{-1} \text{ \AA}^{-3}$ ), whereas the transition metals have a range between dark blue and orange ( $0-3.05 \text{ eV}^{-1} \text{ \AA}^{-3}$ ). This trend in the local softness for coinage as opposed to transition metals matches the generally observed reactivity trends for these metals<sup>113</sup>. The overall range of the local softness for all surfaces at this den-

Surface	$\rho/5 / \text{\AA}^{-3}$	$s_{\max}(\mathbf{r})/ \text{eV}^{-1} \text{\AA}^{-3}$	$\rho/3 / \text{\AA}^{-3}$	$s_{\max}(\mathbf{r})/ \text{eV}^{-1} \text{\AA}^{-3}$
Rh{111}	0.127	2.106	0.211	2.639
Rh{100}	0.127	2.270	0.211	2.705
Rh{110}	0.127	2.542	0.211	3.061
Pd{111}	0.135	2.749	0.224	3.236
Pd{100}	0.135	2.817	0.224	3.217
Pd{110}	0.135	3.051	0.224	3.675
Pt{111}	0.129	2.362	0.215	2.964
Pt{100}	0.129	2.016	0.215	2.431
Pt{110}	0.129	2.927	0.215	3.562
Cu{111}	0.188	0.857	0.314	0.937
Cu{100}	0.188	0.963	0.314	1.050
Cu{110}	0.188	1.048	0.314	1.175
Ag{111}	0.126	0.740	0.210	0.835
Ag{100}	0.126	0.663	0.210	0.751
Ag{110}	0.126	0.587	0.210	0.644
Au{111}	0.122	1.115	0.203	1.330
Au{100}	0.122	0.739	0.203	0.870
Au{110}	0.122	0.808	0.203	0.956

**Table 4.1:** Table showing the maximum values of local softness along a density isosurface with a threshold of a fifth and a third of the bulk valence-electron density.

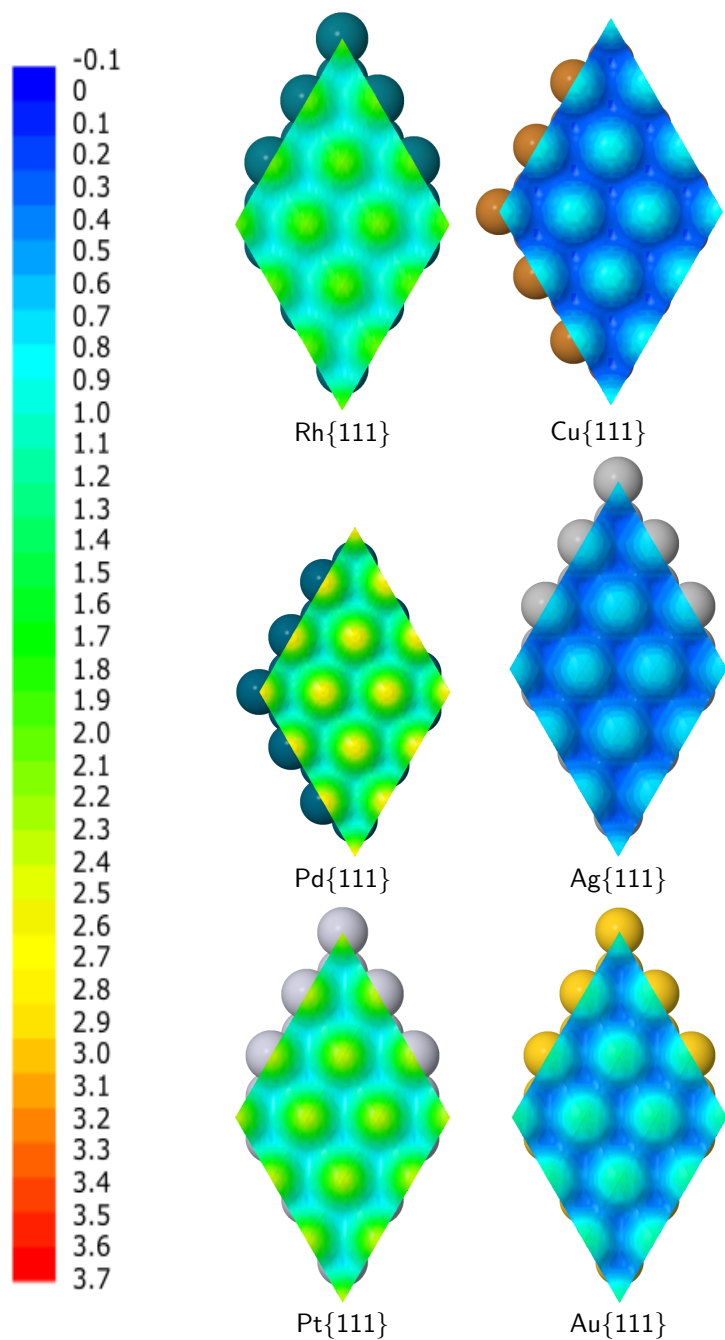


**Figure 4.13:** Colourplots of the local softness for {111} surfaces viewed from above. The plots consist of isosurfaces of the density with a threshold of 1/5 of the bulk valence-electron density. The isosurface is coloured based on the local softness. The range of the colourplots was between -0.1 and 3.7 eV<sup>-1</sup> Å<sup>-3</sup>.

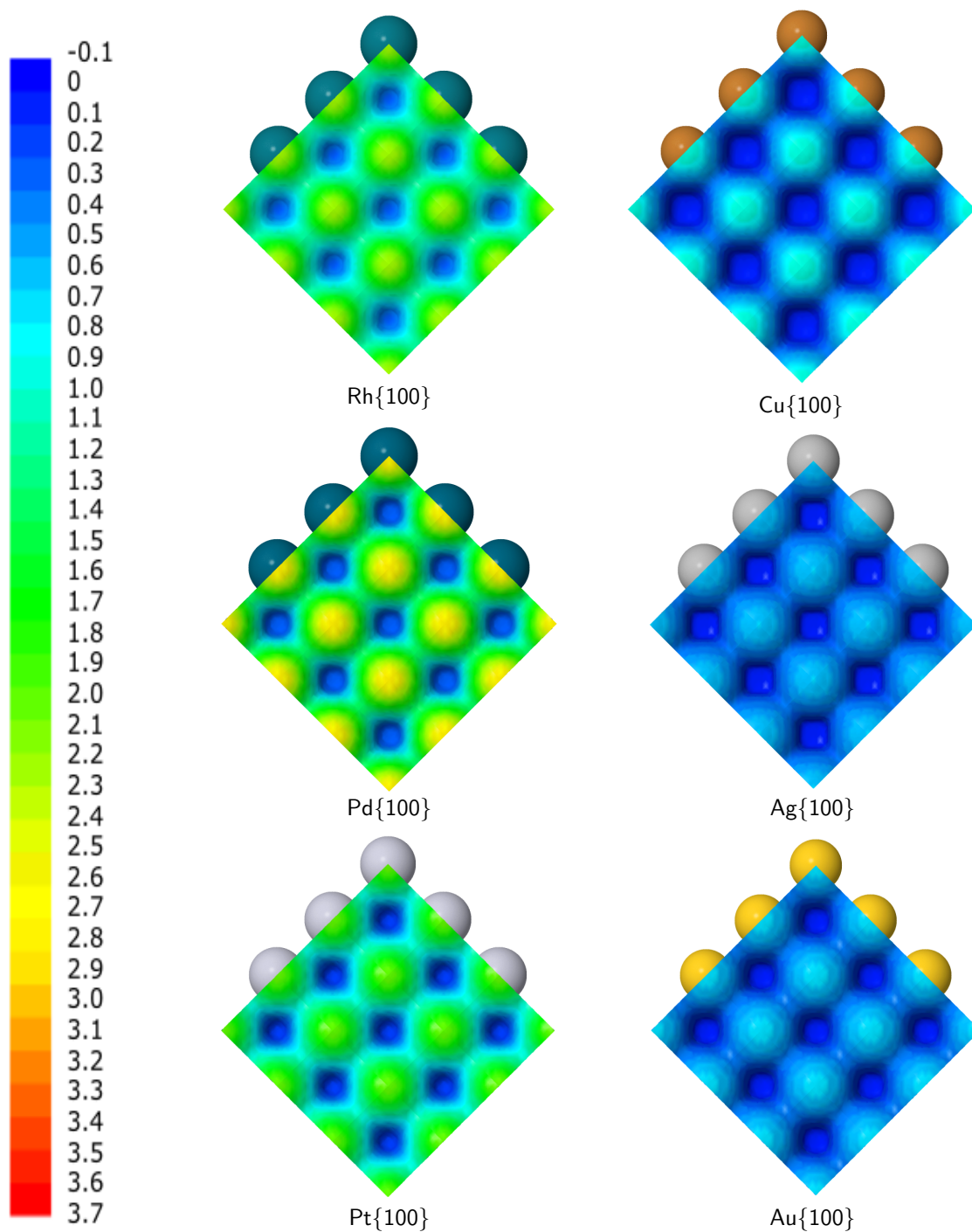


**Figure 4.14:** Colourplots of the local softness for {100} surfaces viewed from above. The plots consist of isosurfaces of the density with a threshold of 1/5 of the bulk valence-electron density. The isosurface is coloured based on the local softness. The range of the colourplots was between -0.1 and 3.7 eV<sup>-1</sup> Å<sup>-3</sup>.

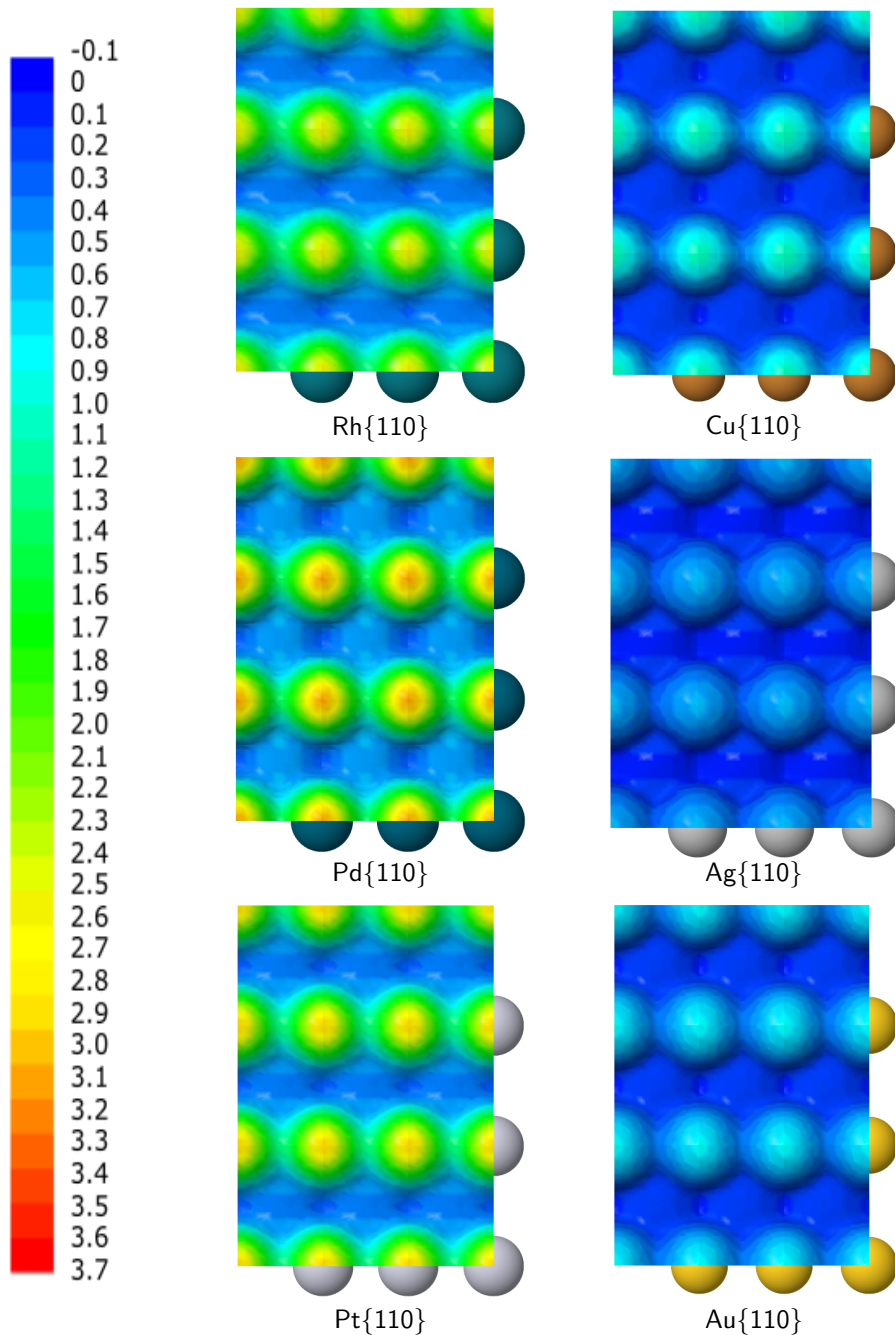


**Figure 4.15:** Colourplots of the local softness for {110} surfaces viewed from above. The plots consist of isosurfaces of the density with a threshold of 1/5 of the bulk valence-electron density. The isosurface is coloured based on the local softness. The range of the colourplots was between -0.1 and 3.7 eV<sup>-1</sup> Å<sup>-3</sup>.

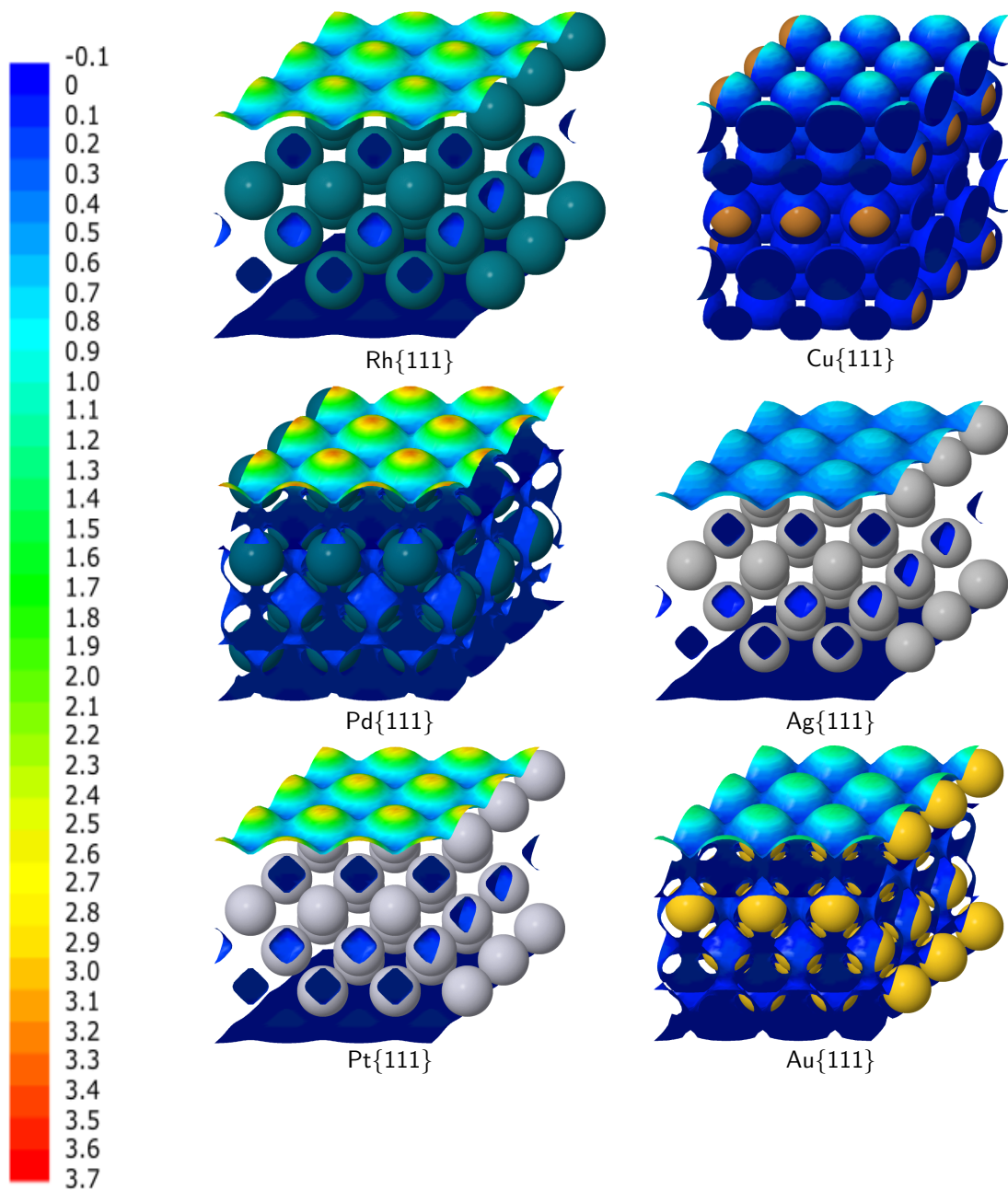


**Figure 4.16:** Colourplots of the local softness for  $\{111\}$  surfaces viewed from the side. The plots consist of isosurfaces of the density with a threshold of  $1/3$  of the bulk valence-electron density. The isosurface is coloured based on the local softness. The range of the colourplots was between  $-0.1$  and  $3.7 \text{ eV}^{-1} \text{ \AA}^{-3}$ .

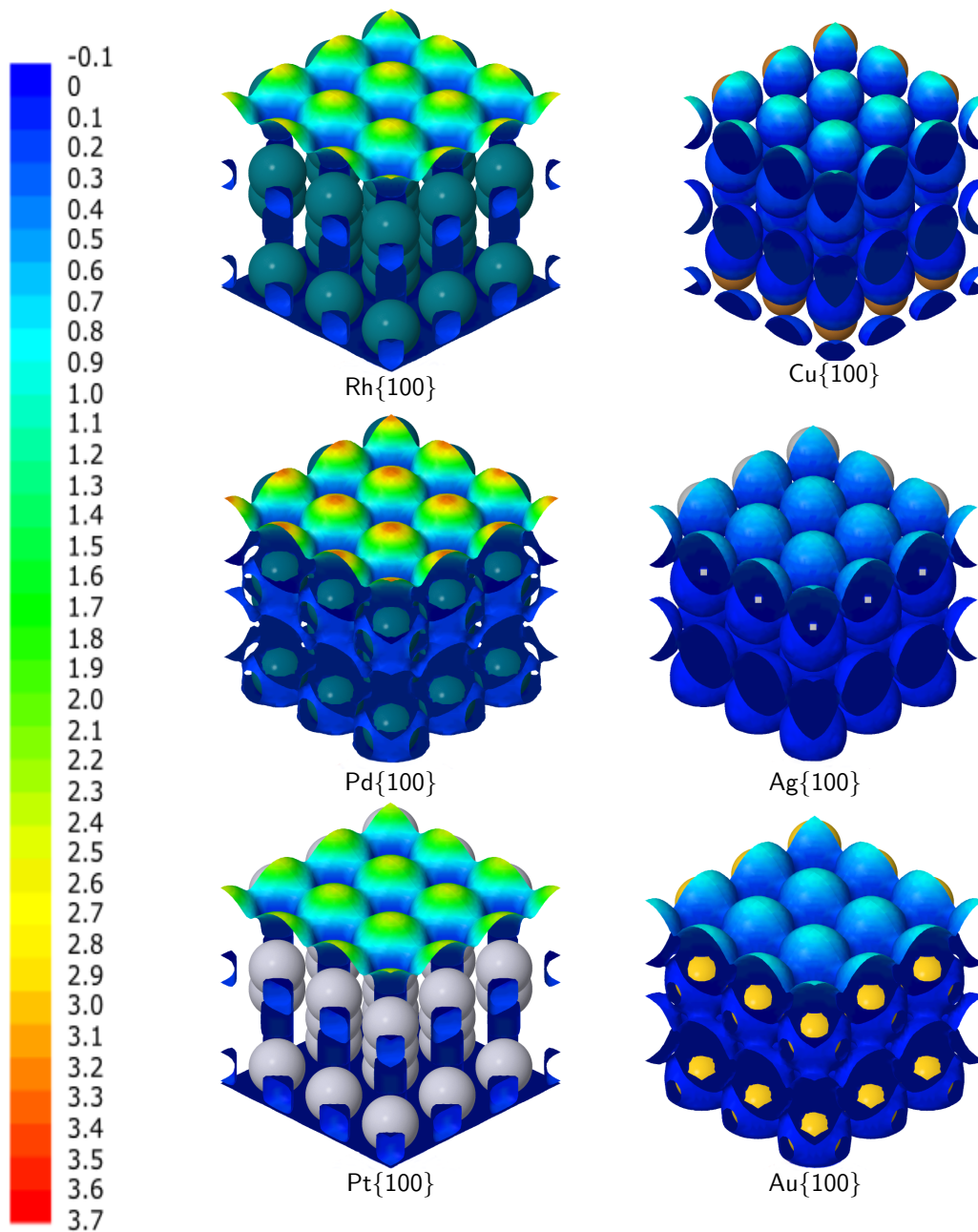


**Figure 4.17:** Colourplots of the local softness for  $\{100\}$  surfaces viewed from the side. The plots consist of isosurfaces of the density with a threshold of  $1/3$  of the bulk valence-electron density. The isosurface is coloured based on the local softness. The range of the colourplots was between  $-0.1$  and  $3.7 \text{ eV}^{-1} \text{ \AA}^{-3}$ .

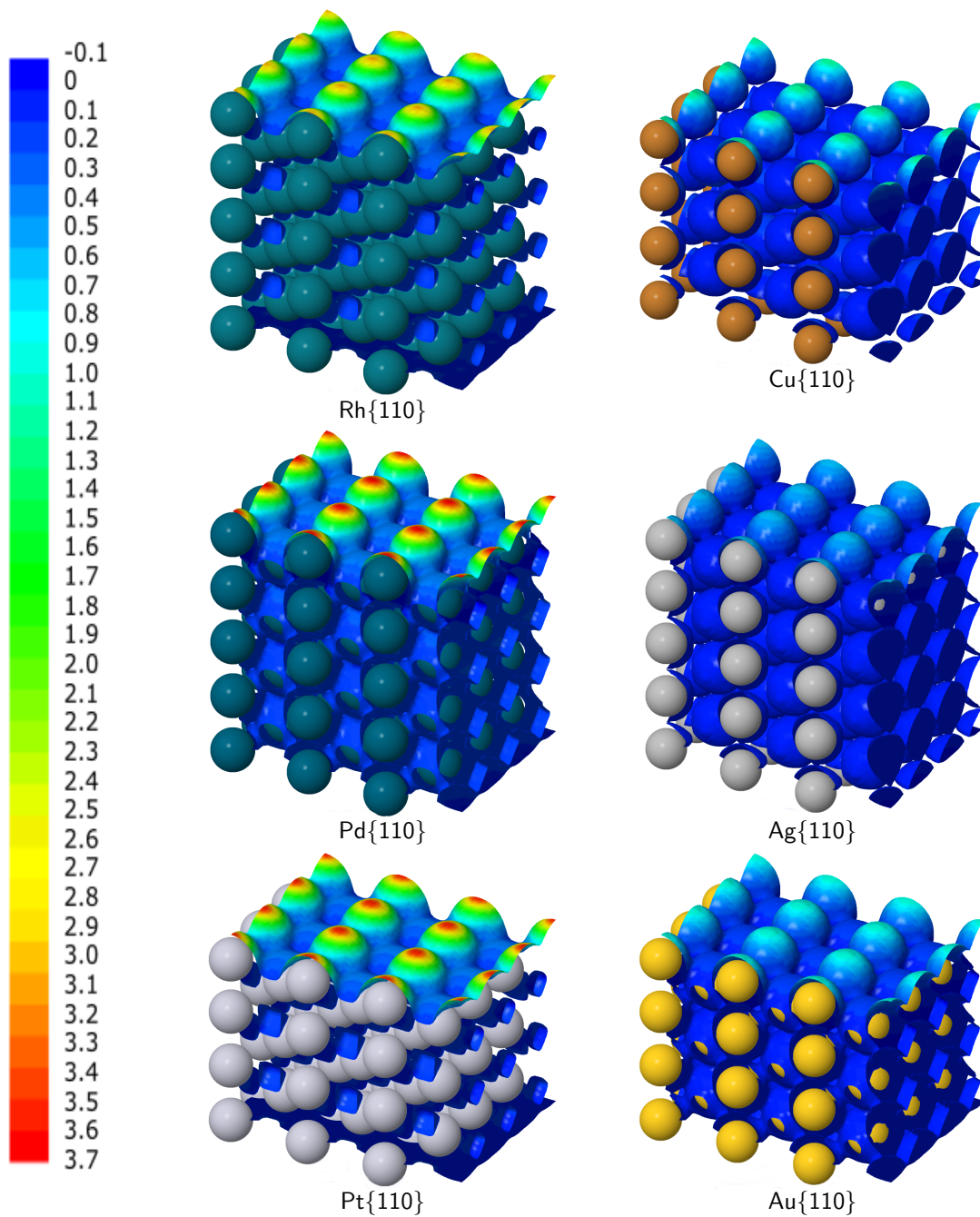


**Figure 4.18:** Colourplots of the local softness for {110} surfaces viewed from the side. The plots consist of isosurfaces of the density with a threshold of 1/3 of the bulk valence-electron density. The isosurface is coloured based on the local softness. The range of the colourplots was between  $-0.1$  and  $3.7 \text{ eV}^{-1} \text{ \AA}^{-3}$ .

sity threshold was from about zero to  $3.05 \text{ eV}^{-1} \text{ \AA}^{-3}$ . This was smaller than the range of local softness for the higher density threshold.

There is a clear distinction between the values of the local softness for coinage metals as opposed to the transition metals for all facets. For both flat and stepped surfaces, the local softness for coinage metals, in the right hand panels, takes values close to or below  $1 \text{ eV}^{-1} \text{ \AA}^{-3}$ . There is much more variety in the values of local softness for the transition metals. This was particularly pronounced for the stepped surfaces. For the transition metals, the stepped surfaces show more variation in the level of reactivity within each surface than the flat surfaces. For example Pd{110} had the greatest range of values, from about zero to  $3.05 \text{ eV}^{-1} \text{ \AA}^{-3}$ . Palladium can be predicted to be the most reactive metal of those studied, as for both density threshold values and all three facets the local softness is higher for Pd than for any other metal. Conversely, silver can be predicted to be the least reactive metal of those studied, as for both density threshold values and all three facets the local softness is lower for Ag than for any other metal.

The shape of regions of high local softness varies between different surface facets. The local softness generally seems to be higher along close-packed rows for all surfaces and to reach a maximum above top-layer atom centres. This is consistent with the shape of the local softness isosurfaces in Figs. 4.2-4.12. For the transition metals, the {111} surfaces have the smallest range at the surface, from cyan to yellow, or about  $0.8\text{-}2.7 \text{ eV}^{-1} \text{ \AA}^{-3}$ . The {100} transition-metal surfaces, which exhibit a fourfold-hollow site, have a greater range of local softness values, from zero to  $2.8 \text{ eV}^{-1} \text{ \AA}^{-3}$ . The lower reactivity of the fourfold hollow on the {100} surfaces as opposed to the three-fold hollow on the {111} surfaces suggests that the larger the hollow site, the lower the hollow-site local softness.

It should be noted that the local softness was calculated for slabs where the outermost layers were allowed to relax. Where the outermost layers were constrained to have the same coordinates as those in the bulk, the local softness was a little higher for those constrained atoms. This was a very

small difference of about 0.4%. This difference can be understood as the atoms being forced into a higher energy position, which therefore causes them to be more reactive.

### 4.2.2 Side views

Figures 4.16-4.18 show side views of the local softness mapped onto a density isosurface with a threshold of 1/3 of the bulk valence-electron density. This density isosurface has a larger threshold than that for the previous section and therefore cuts through space closer to the ion cores. As a result, the range of local softness values are greater. As for the lower density isosurface threshold, in these figures the local softness is lower for the coinage metals than for the transition metals. The coinage metals have a local softness from about zero (dark blue) to about 1.3 (teal). In contrast the local softness at the surface of the transition metals ranges from about 0.1 (dark blue) to about 3.7 (red). The ‘hot spots’ are found on top of the top-layer atoms for all surfaces.

The side view allows the local softness of the surface to be compared with that of the bulk region. The local softness decreases rapidly as one goes further down from the surface. The local softness of second-layer atoms for the {110} surface (fourfold-hollow sites) is much lower than that for the top-layer, step-edge atoms. For the coinage metals there is no visible difference between the colour of the second layer and the lower layers. In contrast, for the transition-metal {110} surfaces the second layer of atoms is slightly more reactive than for the third layer of atoms and below, with a difference of about  $0.1 \text{ eV}^{-1} \text{ \AA}^{-3}$ .

## 4.3 Summary

In this chapter, the local softness was visualised in two ways. First, in Section 4.1, isosurfaces of the local softness were plotted at a variety of threshold values. This approach had the advantages of being relatively simple and giving a qualitative understanding of the shapes of regions of large local softness.

However, no information was given about the distribution of regions of local softness which were above or below the threshold. An alternative, complementary approach was used to make colourplots of the local softness, as described in Section 4.2. This method involved plotting an isosurface of the electron density at a threshold which is a fraction of the bulk valence-electron density. This will form a corrugated surface which can be coloured according to the value of the local softness at each position on the two-dimensional electron density isosurface. Both of the methods of visualising the local softness yielded chemical insight which could be used to make predictions about reactivity.

The local softness above a metal surface is related to reactivity and could be used to predict how strongly an adsorbate might stick to the surface at different positions. The colourplots suggest that the most reactive site on the  $\{110\}$  surfaces would be the atop step-edge site, followed by the short bridge sites along the step edges. Likewise for the  $\{100\}$  surface, the colourplots suggest that the most reactive sites would be the atop site, followed closely by the bridge site. CO is a good example of a small adsorbate which can be used to model adsorption on metal surfaces. The preference for atop binding which can be predicted from the local softness matches that found in the literature for the CO molecule.<sup>112</sup> For the  $\{111\}$  surfaces, the atop site has the highest softness but there is less difference between the softness of the bridge sites compared to the three-fold-hollow sites. Therefore, while the atop site is predicted to be the most favourable for all the facets, if an adsorbate was found to bind on the hollow site, it would be most likely to happen on a transition-metal  $\{111\}$  facet. In the next chapter, the adsorption site of CO on the same eighteen surfaces will be discussed (see Table 5.1). The only hollow-site binding on all eighteen surfaces was observed for Pd $\{111\}$ , which is in line with the predictions which could be made from the local softness.<sup>112</sup> The local softness is a useful measure but it would be helpful to have a more granular index of reactivity, which could be used to predict the adsorption energy at different sites. In the next chapter, the softness of top-layer atoms will be used to predict CO adsorption energy.

## Chapter 5

# Atomic Softness: Predicting CO Adsorption Energy

As mentioned in Section 1.4, there is a need in surface science and catalysis for the comparison of the properties of sites on different metals and facets. For example, it would be helpful to be able to compare a step-edge site on Pd{110} with a terrace site on Rh{111}. A useful contribution towards this site-specific picture would be to calculate the softness of individual atoms on a surface. This atomic softness would be a measure of the reactivity at specific locations and could be quantitatively compared between surfaces and metals. The atomic softness of an atom  $i$  was defined in Eqn. 1.17 as the integral of the local softness over the volume element  $\mathbf{r}_i$ , which contains atom  $i$ . In order to integrate the local softness over the volume of an atom, a method of assigning regions of space to different atoms is needed. One particularly successful and established method of partitioning space is Bader's theory of atoms in molecules.<sup>114,115</sup>

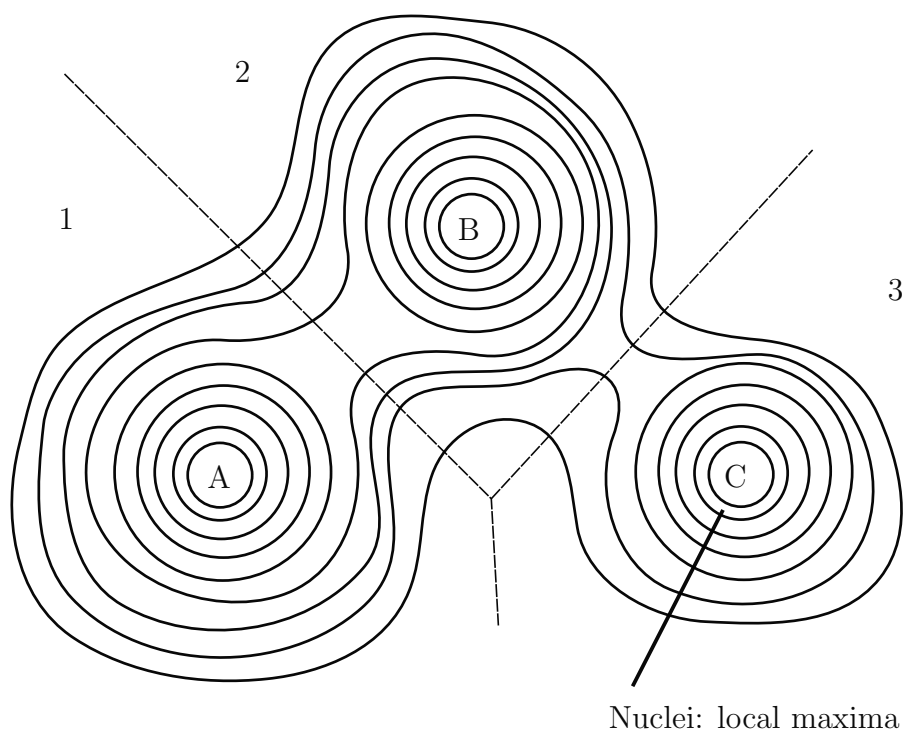


**Figure 5.1:** An illustration of Bader theory for an ABC triatomic. The black lines are contours of electron density as measured in a plane cutting through all three atoms. Space is partitioned by into three regions, labelled 1, 2 and 3, that contain nuclei A, B and C respectively.

## 5.1 Bader's theory of atoms in molecules

Bader's theory is a method of partitioning space within a molecule, solid or surface based on the electron density. The main principle is that the electron density can be expected to reach maxima at atomic centres and decrease away from atoms. In a simple AB diatomic, for example, the electron density would reach maxima at the centres of atoms A and B. In cartesian coordinates chosen with dimension  $z$  parallel to the bond, the bond between A and B would represent a maximum in electron density along the  $x$  and  $y$  coordinates. However, the electron density travelling along the bond from A to B would reach a minima - in other words, the centre of the bond would be a saddle point. The position of the minimum electron density along the bond can be used to assign points in space between atoms A and B.

Figure 5.1 shows the electron density for a simple ABC triatomic. Here the atom centres show as local maxima in the electron density. The bonds will represent the paths of highest electron density between nuclei. Somewhere along each bond will be a minimum along the bond coordinate. As moving perpendicularly to the bond would result in a decrease in electron density this is a saddle point. The saddle point can be seen as the boundary between space associated with atoms A and B. More generally, there will be a surface between atoms A and B over which the normal component of the density gradient is zero. One-dimensional cuts through this surface are shown in Fig. 5.1. By finding the location of the two-dimensional surface, the volume can be partitioned between atoms.

## 5.2 Calculating atomic softness

CASTEP outputs the electron density as a matrix with three indices. The indices correspond to the position within the three-dimensional cell at which density and other volumetric data were recorded. This can be used in conjunction with code adapted from the Jenkins group topology code (Stephen Jenkins, personal communication, Feb. 16th, 2016) in order to find which locations correspond to which atoms. The local softness was calculated at the same grid of points within the cell as that used for the density. This set of values at discrete points was then interpolated and integrated over the volume of individual atoms to give the atomic softness. The atomic softness of top-layer atoms,  $s_1$ , was calculated using this method for eighteen metal surfaces. These were the  $\{111\}$ ,  $\{100\}$  and  $\{110\}$  facets of gold, silver, copper, platinum, palladium and rhodium.

## 5.3 Calculating CO adsorption energy

### 5.3.1 Literature review of CO binding sites

Table 5.1 summarises the experimental literature reports on the structure of the surfaces, both with and without a CO overlayer. Figure 5.2 illustrates

the geometry at which CO was assumed to adsorb in this study. For most cases, there was consensus in the literature about the structures, but for some surfaces there was less agreement.<sup>112</sup>

There is some uncertainty about the adsorption site for CO on Rh{110}.<sup>112</sup> While it is known that CO adsorbs on the short bridge site with a p2mg ( $2 \times 1$ ) structure at 1 ML coverage, there is little consensus in the literature about whether CO adsorbs at the same site or atop in the 0.5 ML coverage c( $2 \times 2$ ) structure.<sup>112,116</sup> An early study by Marbrow and Lambert<sup>117</sup> found that the temperature programmed desorption (TPD) spectra had a single peak. They suggested from this that the adsorption site at 0.5 ML must match that for 1 ML. As Batteas<sup>116</sup> and others<sup>112</sup> found that the adsorption site for 1 ML of CO on Rh{110} is the short bridge, this suggests that the 0.5 ML adsorption site must be the same. However, Dhanak and co-workers<sup>118</sup> performed an X-ray photoelectron spectroscopy (XPS) study that suggested that CO adsorbs atop at 0.5 ML and transitions to the short bridge site at higher coverages. Wei and co-workers<sup>112</sup> made a thorough review of the literature prior to 1997 and said that while no firm conclusion could be made, the evidence better supported the short bridge site at 0.5 ML.

CO adsorbs on the Pd{110} surface to form an ordered overlayer with a distinctive LEED pattern indicating a ( $2 \times 1$ ) cell with p2mg symmetry.<sup>112</sup> The glide symmetry arises from CO having alternating tilts along the close-packed rows. The Pt{110} surface exhibits a missing row reconstruction under UHV conditions, which is lifted in the presence of CO.<sup>119</sup> Comrie and Lambert<sup>119</sup> found that this overlayer was analogous to that formed on Pd{110}.

There are not many literature reports on CO adsorption on gold and silver and what reports there are often disagree.<sup>128,134</sup> The adsorption heat is small, and for some surfaces there may be no ordered overlayer.<sup>125</sup> Interestingly, the adsorption heat for CO on silver was found by several studies to be lower than that for gold, in contradiction to conventional wisdom regarding the relative reactivities of these metals.<sup>134</sup> For the purposes of this thesis I have assumed CO adsorbs on the {111}, {100} and {110} gold and silver surfaces

Surface	Clean structure	Adsorption site	Adsorption structure	$\theta$ / ML	References
Rh{111}	(1 × 1)	atop	( $\sqrt{3} \times \sqrt{3}$ ) R30°	1/3	[112]
Rh{100}	(1 × 1)	atop	c(2 × 2)	1/2	[112, 116, 117]
Rh{110}	(1 × 1)	short bridge	c(2 × 2)	1/2	[112]
Pd{111}	(1 × 1)	fcc hollow	( $\sqrt{3} \times \sqrt{3}$ ) R30°	1/3	[112]
Pd{100}	(1 × 1)	bridge	( $2\sqrt{2} \times \sqrt{2}$ ) R45°	1/2	[112, 120, 121]
Pd{110}	(1 × 1)	atop	(2 × 1)	1 *	[112, 122]
Pt{111}	(1 × 1)	atop	( $\sqrt{3} \times \sqrt{3}$ ) R30°	1/3	[112]
Pt{100}	hexagonal	atop	c(2 × 2)	1/2	[123, 124]
Pt{110}	(1 × 2)	atop	(2 × 1)	1	[119]
Cu{111}	(1 × 1)	atop	( $\sqrt{3} \times \sqrt{3}$ ) R30°	1/3	[112]
Cu{100}	(1 × 1)	atop	c(2 × 2)	1/2	[112]
Cu{110}	(1 × 1)	atop	(2 × 1)	1/2	[112]
Ag{111}	(1 × 1)	atop			[113, 125, 126]
Ag{100}	(1 × 1)				[127]
Ag{110}	(1 × 1)				[128]
Au{111}	( $23 \times \sqrt{3}$ )	atop	(1 × 1)	†	[129, 130]
Au{100}	hexagonal	atop	(1 × 1)	†	[129, 131, 132]
Au{110}	(1 × 2)	atop	(1 × 1)	†	[129, 133]

**Table 5.1:** Table showing the geometry of metal surfaces with and without CO adsorbed. Where the clean surfaces exhibited a reconstruction, the coverage of CO was chosen such as lifted the reconstruction, for example for Au{111} and Au{110}. The results for all three facets of Rh, Cu and Pd as well as the {111} facet of Pt were taken from Table 2 in an article by Wei and co-workers.<sup>112</sup>

\* = The Pd{110}-CO system exhibits a reconstruction between coverages of 0.3-0.75 ML.<sup>112,122</sup>

†= For these surfaces I could not find a literature reference for the coverage or adsorption structure. The references I could find said the reconstruction was lifted with CO adsorption to form a (1 × 1) LEED pattern. However, this does not mean that there was necessarily an ordered CO overlayer with (1 × 1) periodicity. There may have been a disordered layer of CO that would not be evident in the LEED pattern.

Surface	Clean structure	Adsorption site	Adsorption structure	$\theta$ / ML
Rh{111}	(1 × 1)	atop	( $\sqrt{3} \times \sqrt{3}$ ) R30°	1/3
Rh{100}	(1 × 1)	atop	c(2 × 2)	1/2
Rh{110}	(1 × 1)	short bridge	c(2 × 2)	1/2
Pd{111}	(1 × 1)	fcc hollow	( $\sqrt{3} \times \sqrt{3}$ ) R30°	1/3
Pd{100}	(1 × 1)	bridge	( $2\sqrt{2} \times \sqrt{2}$ ) R45°	1/2
Pd{110}	(1 × 1)	atop	(2 × 1)	1
Pt{111}	(1 × 1)	atop	( $\sqrt{3} \times \sqrt{3}$ ) R30°	1/3
Pt{100}	hexagonal	atop	c(2 × 2)	1/2
Pt{110}	(1 × 2)	atop	(2 × 1)	1
Cu{111}	(1 × 1)	atop	( $\sqrt{3} \times \sqrt{3}$ ) R30°	1/3
Cu{100}	(1 × 1)	atop	c(2 × 2)	1/2
Cu{110}	(1 × 1)	atop	(2 × 1)	1/2
Ag{111}	(1 × 1)	atop	( $\sqrt{3} \times \sqrt{3}$ ) R30° †	1/3
Ag{100}	(1 × 1)	atop	c(2 × 2) †	1/2
Ag{110}	(1 × 1)	atop	(2 × 1) †	1/2
Au{111}	(1 × 1)*	atop	( $\sqrt{3} \times \sqrt{3}$ ) R30° †	1/3
Au{100}	(1 × 1)*	atop	c(2 × 2) †	1/2
Au{110}	(1 × 1)*	atop	(2 × 1) †	1/2

**Table 5.2:** Table showing the geometry of metal surfaces with and without CO adsorbed that I used in order to calculate the CO adsorption energy. \* = For these surfaces the clean surface exhibits a reconstruction, but for ease of computation I instead used a (1 × 1) bulk termination. † = as above for Table 5.1

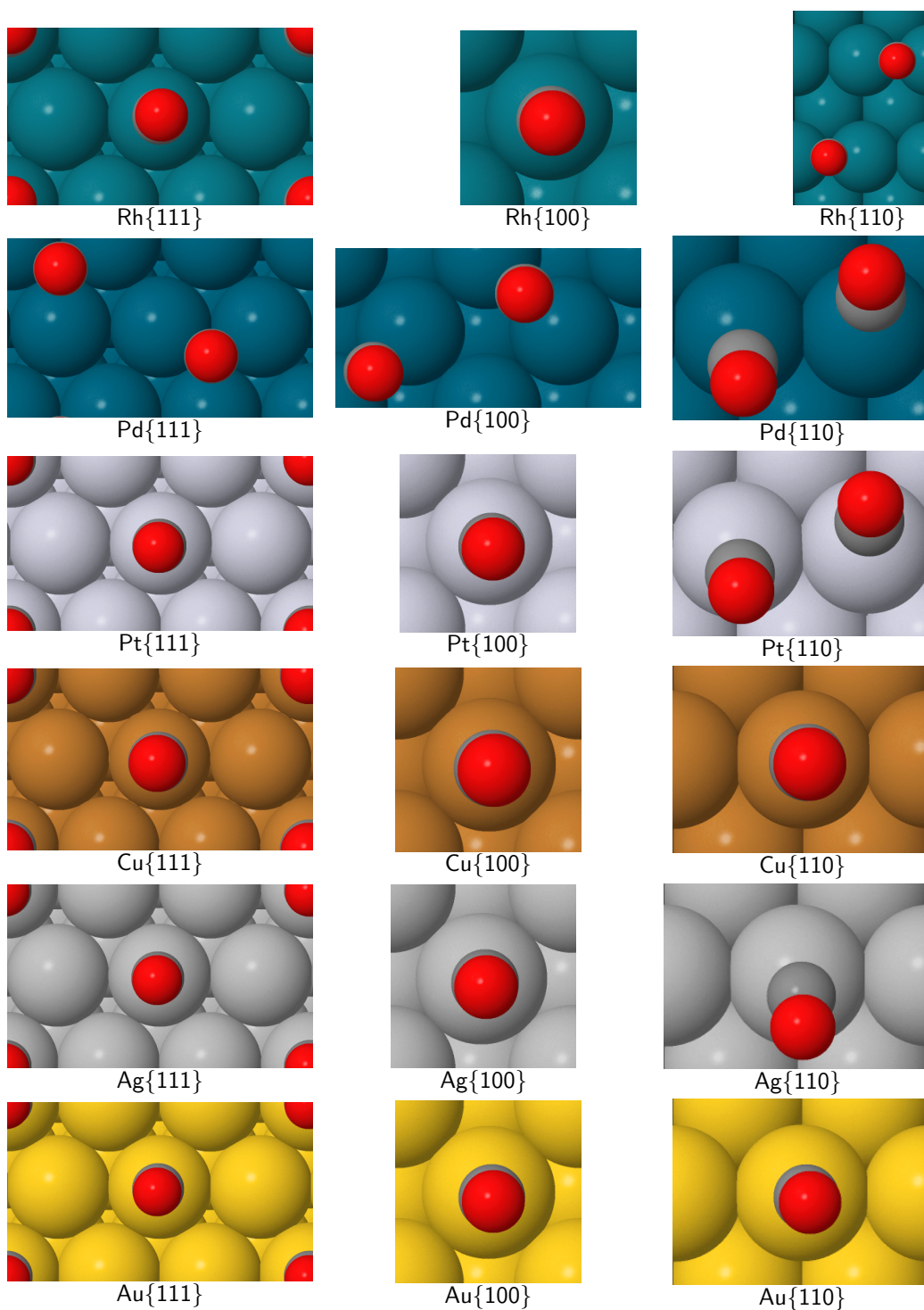


**Figure 5.2:** Figures showing the CO adsorption geometries for each surface, calculated using DFT (with CO starting positions based on the literature).

in an ordered overlayer. I have further assumed that this ordered overlayer has the same structure as the overlayer of CO on the equivalent copper surface. These assumptions are summarised in Table 5.2, and illustrated in Fig. 5.2.

Concerning adsorption of CO on the Au{110} surface, some studies suggest an ordered CO overlayer and a lifting of the reconstruction, whereas others differed.<sup>129,135</sup> One study, by Gottfried and co-workers<sup>136</sup>, found no long-range order to the CO overlayer on Au{110}. They also did some angle-resolved ultra-violet photoemission spectroscopy (ARUPS) measurements that suggested that CO may adsorb parallel to the surface. Meyer et al<sup>135</sup> report that for a wide range of temperatures and pressures of CO the reconstruction was not lifted. In contrast to these findings, Jugnet et al<sup>133</sup> suggest that CO lifts the reconstruction to result in a  $(1 \times 1)$  cell. The same authors thought that CO linearly chemisorbs in an atop position.<sup>133</sup> However, it should be noted that just because the reconstruction was lifted to form a  $(1 \times 1)$  cell in the presence of CO, that does not necessarily mean that an ordered overlayer of CO formed with  $(1 \times 1)$  symmetry.<sup>119</sup> LEED is a diffraction technique and therefore only shows ordered surface structure. A disordered overlayer would therefore be invisible to LEED, other than contributing to a diffuse background.

In a similar case to Au{110}, early studies of Au{100} found no ordered CO overlayer.<sup>135</sup> However, later studies by Pierce and co-workers have found that at higher pressures of CO there is a stable overlayer formed.<sup>129,131</sup> The same authors also found that CO adsorption lifted the hexagonal reconstruction of Au{100} to a  $(1 \times 1)$  structure.<sup>131</sup> Pierce et al<sup>131</sup> did not report an adsorption site for CO on Au{100}, but Nakamura and co-workers<sup>132</sup> found that their polarization modulation infrared reflection absorption spectroscopy (PM-IRAS) results were consistent with CO adsorbing atop Au atoms.

Similarly, for Au{111}, early studies found that adsorption of CO lifted the herringbone ( $23 \times \sqrt{3}$ ) reconstruction and (under certain conditions of high temperature and CO pressure) restored the  $(1 \times 1)$  structure.<sup>135,137</sup> However, they also found that the surface might not form an ordered  $(1 \times 1)$

overlayer.<sup>135,137</sup> In contrast, while later authors agreed with Peters et al in finding that CO lifted the herringbone reconstruction, they also found that the reconstruction was completely lifted at 250 Torr, resulting in a  $(1 \times 1)$  structure, with CO adsorbed atop.<sup>130</sup> For the purposes of this thesis I have assumed that CO forms an ordered overlayer on Au{111} that has the same structure as that formed by CO on Cu{111}.

In terms of CO adsorption on Ag{111}, Abild-Pedersen and co-workers report that CO adsorbs atop.<sup>113</sup> However, other literature reports suggest that there is no ordered overlayer for CO on Ag{111}.<sup>125,126</sup> Work by Hansen and co-workers<sup>126</sup> suggests the CO molecules have a random orientation on Ag{111}. For the Ag{110} surface, the literature suggests the CO is very weakly bound, and may even be bound with a random orientation, or with the CO bond parallel to the surface.<sup>128</sup> I was unable to find any literature reference for the adsorption of CO on a clean Ag{100} surface. However, work by Burghaus and co-workers<sup>127</sup> suggests that the clean surface does not reconstruct.

### 5.3.2 Slab and vacuum thickness

In making supercells for CO adsorption calculations, there are some restrictions on which combinations of slab and vacuum thickness are possible. In particular, it is not possible to have a non-integer number of slab layers, therefore the slab thickness must be an integer multiple of the layer spacing,  $d_{hkl}$ . Therefore I could not use exactly the same slab thickness for all calculations as different surfaces have a different layer spacing,  $d_{hkl}$ . I used the first integer multiple of  $d_{hkl}$  that exceeded 18 Å. In addition, the code I used in order to make cell files for CASTEP calculations makes cell files with an integer number of vacuum layers. Although it is not necessary to make the vacuum thickness an integer multiple of  $d_{hkl}$ , doing so made the process of making cell files simpler. For this reason I decided to make the vacuum thickness for CO adsorption calculations the first integer multiple of  $d_{hkl}$  that exceeded 18 Å. For a summary of the numbers of slab and vacuum layers and the resulting slab and vacuum thickness see Section A.2. I arranged the cell files so that the slab was more or less centred in the middle of the cell.

This makes it easier to be sure that the CO molecule will not be near the edge of the supercell. It should be noted that whilst having the molecule cross the supercell boundary would be no problem for the CASTEP calculation, it would make the output of the Bader analysis code more awkward to interpret.

### 5.3.3 Adsorption energy calculation methodology

The adsorption energy of an adsorbate A,  $E_{\text{ads}}$ , is defined as

$$E_{\text{ads}} = E_{\text{sys}} - E_{\text{surf}} - nE_{\text{A}} \quad (5.1)$$

Where  $E_{\text{sys}}$  is the energy of the system with  $n$  adsorbed molecules of A,  $E_{\text{surf}}$  is the energy of the clean surface and  $E_{\text{A}}$  is the energy of a single molecule of A in a vacuum. These vacuum calculations were performed in a large cubic cell (where the length of each of the three axes of the supercell was 10 Å) Due to the large size of the real-space unit cell, the reciprocal unit cell was small, and therefore one  $\mathbf{k}$  point was used. In each case energies were obtained for the optimised atomic positions.

## 5.4 Predicting CO adsorption energy from atomic softness

### 5.4.1 Predicting CO adsorption: experimental sites

Table 5.3 compares the atomic softness of top-layer atoms with the CO adsorption energy calculated by DFT at the preferred adsorption sites from the experimental literature. The geometry of these literature-preferred sites was illustrated in Fig. 5.2, above. The data in Table 5.3 is also displayed in graphical form in Fig. 5.3. Figure 5.3 shows the correlation between the top-layer atomic softness and the minimum CO adsorption energy (i.e. strongest binding to the surface). There is a linear trend with a large amount of scatter. In each case the data falls into two main groups, with coinage metals (copper,

silver and gold) in the top left and with transition metals (rhodium, platinum and Palladium) in the bottom right. The different colours show whether the facets were {111}, {100} or {110}. While there is a linear trend overall, there is a large amount of scatter and there is not a strong linear trend within the two individual sets of data for coinage and transition metals, which suggests that the atomic softness is not strongly correlated with CO adsorption energy when compared between very similar metals and surfaces.

The adsorption energies in Table 5.3 were obtained by DFT calculations. They should be compared with accurate experimental data to see how much confidence can be placed in the trends in Fig. 5.3. One of the most accurate methods of finding the experimental adsorption energy is single crystal adsorption calorimetry (SCAC).<sup>138</sup> The DFT values of the adsorption energy were compared with the integral adsorption heats listed in Table 1 of the review by Ge and co-workers.<sup>139</sup> For the Pd{100} surface, the experimental integral adsorption energy was -1.27 eV whereas from Table 5.3 it was found to be -2.10 eV. This is a difference of 49%. Similarly for the Rh{100} surface the DFT adsorption energy of -2.00 eV was much more negative than the SCAC integral value of -1.19 eV, with a percentage difference of 51%. In contrast the DFT adsorption energy for Pt{110} only had a difference of 19% between the theoretical value of -2.20 eV and the SCAC integral value of -1.81 eV. For the Pt{111} surface, there was no integral heat listed in the review by Ge and co-workers.<sup>139</sup> However, it is possible to estimate the experimental heat from an integral of their graph of the differential heat. My estimate was based on SCAC differential adsorption heats listed in the review by Brown and co-workers.<sup>138</sup> I estimated that the integral adsorption heat for Pt{111} was about 1.8 eV, which is very similar to my DFT value of -1.74 eV, with a percentage difference of 2%.

I generally found that the DFT result was more negative than the experimental result. This is what could be predicted as DFT tends to over-bind adsorbates on transition metals.<sup>139,140</sup> For example, of the theoretical and experimental values listed in Ge and co-workers' review, the theoretical values are almost always more negative than the experimental values.<sup>139</sup>

Surface	$s_1 s_1 / \text{eV}^{-1}$	CO Adsorption Energy/ eV	Coverage/ ML
Cu{111}	5.573	-1.099	1/3
Ag{110}	6.541	-0.625	1/2
Ag{100}	6.605	-0.548	1/2
Au{100}	7.039	-0.621	1/2
Cu{100}	7.104	-1.288	1/2
Ag{111}	7.288	-0.479	1/3
Cu{110}	7.981	-1.323	1/2
Au{110}	8.304	-0.843	1/2
Au{111}	9.697	-0.481	1/3
Pd{100}	11.222	-2.101	1/2
Rh{111}	14.558	-1.960	1/3
Pt{100}	15.517	-2.050	1/2
Rh{100}	16.058	-1.998	1/2
Pt{111}	16.443	-1.736	1/3
Pd{111}	18.827	-2.219	1/3
Rh{110}	20.058	-2.098	1/2
Pt{110}	22.388	-1.981	1
Pd{110}	26.723	-1.491	1

**Table 5.3:** Table showing the top-layer atomic softness,  $s_1$ , and calculated CO adsorption energy at the literature adsorption site for eighteen different metal surfaces. The adsorption energies are all for the most favourable site based on the experimental literature.

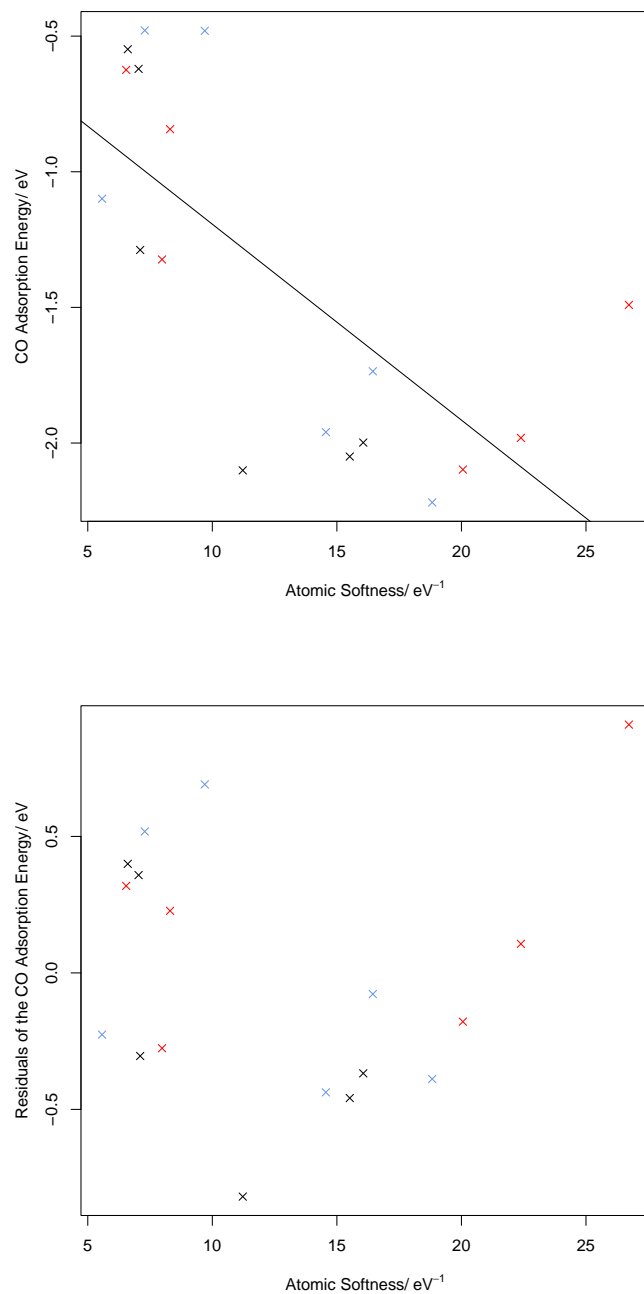


**Figure 5.3:** Upper panel shows the correlation between top-layer atomic softness and the calculated CO adsorption energy at the adsorption site favoured in the experimental literature. Lower panel shows the residuals. In both panels the black data points refer to {111} surfaces, the blue data points to the {100} surfaces and the red data points to the {110} surfaces. The fitted equation was  $E_{\text{ads}} = -0.0722s_1 - 0.471$  and the  $R^2$  value was 0.497.

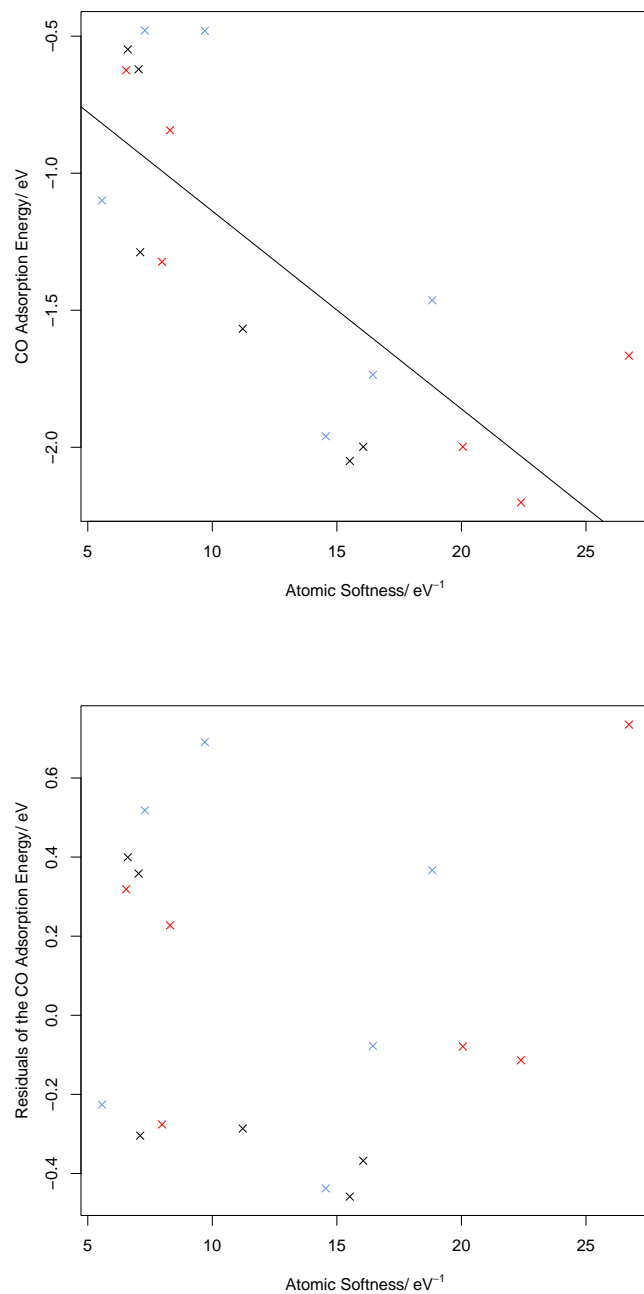
### 5.4.2 Predicting CO adsorption: atop sites

Table 5.3 in the previous section describes the trend between the atomic softness of top-layer atoms and the adsorption energy of CO at the preferred adsorption sites from the literature. On the other hand, for ease of comparison between surfaces, unencumbered by possible changes in adsorption site, the data in Table 5.4 only uses the atop site, even when this does not seem to be the most favourable. There is also a restriction to low coverages of 0.5 ML and below, whereas coverages as high as 1 ML were considered in the previous section where they were found in the literature-preferred CO geometry. The same data from the atop site is presented in graphical form in Fig. 5.4. In summary, whereas Fig. 5.3 is plotted for the most favourable literature CO site and coverage, Fig. 5.4 is plotted for atop CO adsorption and 0.5 ML or less coverage, even when that was not the most favourable.

Table 5.4 shows the atomic softness of top-layer atoms and the atop CO adsorption energy for different surfaces. The same data is illustrated graphically in Fig. 5.4. The data falls into two groups, with the atomic softness correctly predicting that the coinage metals will be less reactive. This matches the observations made in the previous section for the CO adsorption at the preferred literature adsorption sites in Fig. 5.3 and Table 5.3. There is no overlap between the coinage and transition-metal groups. All the coinage-metal surfaces had lower atomic softness and smaller (less negative) atop site CO adsorption energy than any of the transition-metal surfaces. There is no particular trend to the distribution of atomic softness for different facets within the coinage-metal group. In contrast to this, for the transition-metal group, the three  $\{110\}$  facets had the highest atomic softness for top-layer atoms. Based on this it might be predicted that the adsorption energy for the  $\{110\}$  facets would be more exothermic than for the flat  $\{100\}$  and  $\{111\}$  surfaces. However, the atop adsorption energy for the stepped transition-metal surfaces was not as negative as might be expected based on these values of the atomic softness. In particular, the Pd $\{110\}$  surface is an outlier in Fig. 5.4 as it has less negative adsorption energy than might be expected. This may be partly because actually the surface would reconstruct at that coverage of

Surface	$s_1 / \text{eV}^{-1}$	CO Adsorption Energy/ eV	Coverage/ ML
Cu {111}	5.573	-1.099	1/3
Ag {110}	6.541	-0.625	1/2
Ag {100}	6.605	-0.548	1/2
Au {100}	7.039	-0.621	1/2
Cu {100}	7.104	-1.288	1/2
Ag {111}	7.288	-0.479	1/3
Cu {110}	7.981	-1.323	1/2
Au {110}	8.304	-0.843	1/2
Au {111}	9.697	-0.481	1/3
Pd {100}	11.222	-1.568 *	1/2
Rh {111}	14.558	-1.960	1/3
Pt {100}	15.517	-2.050	1/2
Rh {100}	16.058	-1.998	1/2
Pt {111}	16.443	-1.736	1/3
Pd {111}	18.827	-1.464 *	1/3
Rh {110}	20.058	-1.998 *	1/2
Pt {110}	22.388	-2.201	1/2 †
Pd {110}	26.723	-1.666	1/2 †

**Table 5.4:** Table showing the top-layer atomic softness and calculated atop site CO adsorption energy for eighteen different metal surfaces. The adsorption energies are all for CO adsorption at the atop site, even where a different site would have a more exothermic adsorption (marked \*). Also the coverages were kept at 0.5 ML or below, and the un-reconstructed surfaces were used, even where this was found not to be the case experimentally (marked †).



**Figure 5.4:** Upper panel shows the correlation between atomic softness of top-layer atoms,  $s_1$ , and the calculated CO adsorption energy at the atop adsorption site for coverages of 0.5 ML and less. Lower panel shows the residuals from the upper plot. The colour coding is the same as for Fig. 5.3.  $E_{\text{ads}} = -0.0722s_1 - 0.416$  The  $R^2$  value was 0.574.

CO, to form a lower-energy structure.<sup>112,122</sup>

### 5.4.3 General observations

The implication of Figs. 5.3 and 5.4 is that there is a large-scale trend where metal surfaces with very soft top-layer atoms tend to have higher CO adsorption energy. Therefore the atomic softness can be used to predict large-scale trends in reactivity, such as the difference between coinage metals and transition metals. However, within these two groups of metals, the atomic softness fails to accurately predict the differences in reactivity of similar metal surfaces as there is too much scatter on the graph. For example, the atomic softness of the gold {111} surface is anomalously high.

The general trend is that the adsorption heat becomes more negative as the atomic softness increases. This represents stronger binding for larger atomic softness values. The atomic softness can therefore be used to predict the order of reactivity of CO binding to these surfaces. The observed trend was between top-layer atomic softness and the adsorption energy of CO at the site of strongest binding. This was obtained for low coverage, where the metal-adsorbate interaction is the dominant feature of binding. The low coverages were chosen so that the metal-adsorbate binding was the main effect studied. This means that the direct effect of the metal surface reactivity on the strength of the metal-adsorbate bond can be observed. At higher coverages the adsorbate-adsorbate interactions (repulsive in this case) can be predicted to dominate the adsorption energy.

It should be noted that in Figs. 5.3-5.4 and Tables 5.3-5.4 the adsorption heats for the coinage metals were calculated using the Tkatchenko-Scheffler (TS) Van der Waals correction.<sup>141</sup> This is a semi-empirical method that has been found to improve the binding strength of adsorbates on coinage metals.<sup>141</sup> However, the TS Van der Waals correction was not used for Rh, Pd or Pt. It should be noted that since TS causes an increase in calculated binding strengths,<sup>142</sup> if TS had been switched on for both groups of metals or neither, then this would have caused the linear trend to have a higher

gradient. Therefore we can be relatively confident that the gradient of the trend line shown is a lower bound to the true gradient, and we can be fairly confident that there is a significant difference between the CO adsorption energy of coinage and transition metals. If anything, the trend shown is an under-estimate of the actual trend between atomic softness and CO adsorption energy.

Figures 5.3 and 5.4 have the same fitted gradient of  $-0.0722 \text{ eV}^2$  but different intercepts of  $-0.471 \text{ eV}$  and  $-0.416 \text{ eV}$  respectively. In both Fig. 5.3 and 5.4 the scatter (as shown in the right hand panels, which plot the residuals) seems relatively random, which suggests a straight line plot is the best model to fit the data. For Fig. 5.3 there is more scatter than in Fig. 5.4. This is characterised by the  $R^2$  values, which are 0.497 for Fig. 5.3 and 0.574 for Fig. 5.4. The greater scatter for the graph showing the literature minimum adsorption energy position may be because the atomic softness of top-layer atoms is better suited to predicting the atop adsorption energy. Also in Fig. 5.3 two of the data points for the  $\{110\}$  surfaces are for 1 ML coverage and therefore are higher in energy compared to the trendline (due to greater adsorbate-adsorbate repulsion). In Fig. 5.4 these points are lower in energy and therefore closer to the trendline. As the fit was better for the atop site adsorption with coverages of 0.5 ML and lower, this was used for the graphs of individual facets in Fig. 5.5, as will be discussed below.

#### 5.4.4 Trends for individual facets

Figure 5.5 shows the correlation between atomic softness and atop site CO adsorption energy for coverages of 0.5 ML and below for individual surface structures. For each surface, there is a roughly linear trend where the adsorption energy becomes more negative as the atomic softness increases. The trend is best for the  $\{100\}$  surface, which has an  $R^2$  value of 0.848. The trend is worst for the  $\{111\}$  surface, which has an  $R^2$  value of 0.498. In all the graphs, as in the graph of all the data together, the data points fall roughly into two clusters, one for the coinage metals and one for the transition metals.

The gradient for the  $\{100\}$  surface was quite a bit larger than the gradient for all the data together. In comparison, the gradient for the  $\{110\}$  surface was smaller than that obtained for the whole dataset. This is probably due to the random scatter of the data, which gives rise to a great deal of error in the calculated gradient, especially where the number of datapoints used to calculate the gradient is smaller.

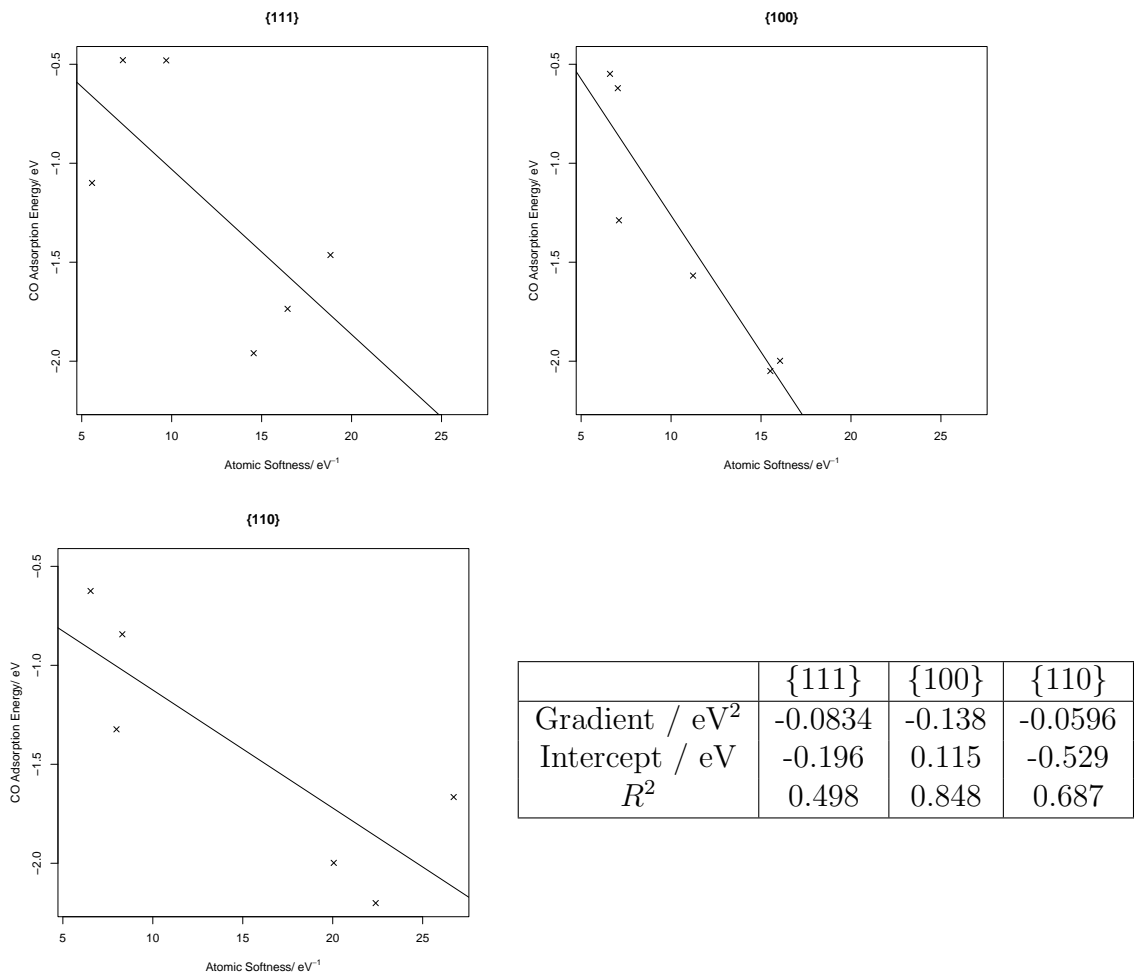


**Figure 5.5:** Correlation between atomic softness and atop CO adsorption energy for coverages of 0.5 ML and less, for the  $\{111\}$ ,  $\{100\}$  and  $\{110\}$  surfaces. Table in bottom right panel shows the coefficients of the fitted line from each graph.

## 5.5 Summary

There is a linear trend where as the atomic softness increases the adsorption energy becomes more exothermic. This is particularly apparent where the atomic softness is compared with the atop adsorption energy at coverages of 0.5 ML or below. While the trend between the atomic softness and the adsorption energies calculated at the adsorption sites preferred in the experimental literature is still a relatively clear linear trend, it has a larger scatter and correspondingly smaller  $R^2$  value. The atomic softness also predicts that step-edge atoms will be more reactive than terrace atoms, which is generally the case.<sup>96</sup>

The results in this chapter show that the atomic softness can be useful for predicting large-scale trends in reactivity. For example, all the coinage metals studied had lower atomic softness than any of the transition-metal surfaces studied. However, for more similar systems, the atomic softness does not necessarily predict the reactivity so well. Overall, despite these limitations, the atomic softness is a promising reactivity index for predicting the reactivity of metal atoms on surfaces. It would be interesting to see whether the atomic softness would also be useful to predict the reactivity of adsorbates on a metal surface. This will be investigated in the next chapter.

## Chapter 6

# The Local and Atomic Softness of Aromatic Adsorbates

One of the key problems in catalysis is understanding how the surface of a catalyst affects the reactivity of adsorbed reactants. The surface science approach involves calculating the electronic structure of an adsorbate on a metal surface and trying from this to draw conclusions about how a catalyst might affect the molecule, using the metal surface as a model system. It would be helpful to have a reactivity index that could be used to make qualitative and quantitative comparisons of reactivity between different atoms within an adsorbed molecule on a metal surface. It would also be useful to be able to compare an atom from one adsorbate on one metal surface with an atom in a different adsorbate on a different surface. For example, it would be interesting to investigate directing effects on different aromatic rings and see how they are affected by adsorption on a metal surface.

The main reactivity index used in surface science is the d-band centre, which was developed by Nørskov and co-workers as a measure of transition-metal reactivity.<sup>1</sup> As previously discussed in Section 1.6.1, the d-band centre is effectively the energy of the ‘centre of mass’ of the d band in the band structure. The d-band centre has been very successful in predicting the reactivity of transition-metal atoms. However, due to the nature of its formulation as

a function of the d-band structure, it is not suitable as a reactivity index for any element other than transition metals. Therefore it cannot be used for adsorbates.

One of the advantages of the local softness is that it can be calculated for adsorbates on a metal surface. In order to do this, it is helpful to make the assumption that the electronic properties of the metal-adsorbate system are mostly determined by the electronic properties of the clean metal surface. Therefore it can be assumed that the denominator of the local softness for an adsorbate on a metal surface is the same as the denominator of local softness for the clean metal surface.

This makes it much easier to calculate the local and atomic softness of adsorbates on metal surfaces. This is because performing spectral tasks is relatively expensive, especially for larger unit cells. As discussed in Section 3.4, a large number of spectral tasks need to be performed in order to find the denominator of local softness. As the corrected denominator converges exponentially towards the large-cell limit, it requires calculations with a range of increasingly larger surface-normal supercell dimensions. For a clean surface this is not too much of a problem as  $(1 \times 1)$  lateral dimensions are sufficient.

However, in order to perform a calculation with a large adsorbate, it becomes necessary to increase the lateral dimensions. As DFT calculations scale by  $N^3$  or higher with system size  $N$ , calculating the denominator for a surface with an adsorbate would be very expensive. By assuming that the denominator will be the same in each case, the denominator from a set of cheaper calculations for a  $(1 \times 1)$  clean cell can be used to calculate the local softness for a cell with an adsorbate that has larger lateral dimensions.

This approximation is helpful but makes it more difficult to compare the reactivity of an atom on an adsorbate with the reactivity of a different atom on a different adsorbate. However, the local softness, which has been calculated using this approximation, can still be compared between sites for a given metal-adsorbate system. Depending on how similar the denominator would

be for different adsorbates compared to the clean metal, it may be reasonable to make comparisons of the local and atomic softness between surfaces with different adsorbates as well. A good way of testing this hypothesis, and seeing how good the approximation of using the denominator from the clean surface is, would be to compare the atomic softness of middle-layer atoms between the clean surface and the surface with different adsorbates. This was done in Section 6.6.

## 6.1 Directing effects in aromatic adsorbates

It is a matter of some debate at present what constitutes an active site and whether an active site can be present in the absence of adsorbates.<sup>12</sup> For the processes where the active sites are known it would be very interesting to study the local softness of the active site with and without adsorbates. In particular this would also enable the effect of adsorbates on reactivity of the metal surface to be studied. In addition, it would be interesting to study the effect of the metal surface on the reactivity of the adsorbate.

An interesting problem in organic chemistry is understanding how the reactivity of benzene is modified by adding a side group.<sup>143</sup> Figure 6.1 shows the three distinct types of position on an aromatic ring with a side group (denoted by R). Of these positions, the ortho position is nearest to R, followed by meta, and para is opposite the side group. If R is a  $\pi$ -donating or  $\pi$ -withdrawing group, then it will conjugate with the aromatic ring in particular ways. Electron-donating groups such as OMe increase the rate of electrophilic attack at the ortho and para positions. This is due to the way in which the lone pairs of the oxygen conjugate with the aromatic ring.<sup>143</sup> In contrast, electron-withdrawing groups such as NO<sub>2</sub> make the aromatic ring less reactive to electrophilic attack. However, when they do react, the side group will direct electrophiles to the meta positions on the ring. In particular, groups that withdraw  $\pi$  electrons from the aromatic ring do so especially at the ortho and para positions. Therefore the ‘least unreactive’ sites are the meta sites, which do not conjugate as strongly with the side group.

It would be interesting to see how adsorption on a metal surface affects the conjugation of  $\pi$ -donating and  $\pi$ -withdrawing groups with the benzyl ring. This was investigated by Tan and co-workers in 2005.<sup>144</sup> They conducted a theoretical study of anisole on Pt{111}. The authors assumed that anisole adsorbed on the bridge site. They found that the metal significantly changed the nature of bonding in the aromatic ring. The reactivity was more affected by the metal surface than by the side group, and the ring was similar to benzene in its electronic properties. In particular, they found that the HOMO and LUMO of the adsorbed molecule had more similarity with those of adsorbed benzene than with free anisole. It would be interesting to calculate the local and atomic softness of anisole and see if it contributes some additional insight into reactivity.

Anisole, as an aromatic ring with a  $\pi$ -donor side group, only represents half the picture of directing effects in aromatic molecules. It would be interesting to also consider the reactivity of a conjugated electron-withdrawing group such as NO<sub>2</sub>. This would allow the local and atomic softness of a molecule with a group that should be ortho and para directing to be compared with that of a molecule with a group which should be meta directing. It would also be interesting to compare the reactivity of both with the reactivity of benzene, as a control for the study. Therefore, the local and atomic softness was calculated for anisole, nitrobenzene and benzene on the Pt{111} surface.

## 6.2 Computational methods used to study aromatic adsorption

As for the work in Chapters 3-5, calculations were done in CASTEP with the PBE exchange and correlation functional, which is a GGA functional. It should be noted that Tan and co-workers used a different GGA functional, that was developed by Perdew and Wang.<sup>86,144</sup> However, the two functionals are relatively similar and produce very similar results, for example the O-Me bond length and Ph-O-Me angle were almost identical. There was more of

a difference with the Ph-O bond length, which the PBE functional found to be 0.1 Å shorter than that found by Tan et al. The plane-wave basis set cutoff energy was 340 eV, which matches that used by Tan et al, as well as that used in previous chapters of this work. The standard CASTEP library pseudopotentials were used, as for Chapters 3-5.

Anisole, benzene and nitrobenzene were adsorbed at a coverage of 0.11 ML, which matches that used by Tan et al for anisole. The cell used was  $(3 \times 3)$  and there were four slab layers and seven vacuum layers. The top two metal layers were allowed to relax. This is the same as the supercell geometry used by Tan et al, with the exception that Tan et al used eight vacuum layers. The Brillouin-zone integration was performed using a  $3 \times 3 \times 1$  Monkhorst-Pack  $\mathbf{k}$ -point mesh. This is a finer mesh than that used by Tan et al.

The starting geometry for anisole was based upon Fig. 5 from Tan et al, with the ring planar and centred on a bridge site. It should be noted that Tan and co-workers did not do a comprehensive search of all the possible starting geometries, but used a starting structure that matched the minimum-energy structure found for benzene on Ni{111}.<sup>145</sup> In determining the starting geometry for benzene I made the positions of the carbon and hydrogen atoms analogous to those used by Tan et al for anisole. Likewise, the starting geometry for nitrobenzene was at the same bridge site and with the NO<sub>2</sub> group attached to the same carbon that the OMe group had been in anisole. The geometry optimisations were performed with and without the Tkatchenko-Scheffler (TS) Van der Waals correction.<sup>141</sup> All other computational details, such as tolerances, were the same as those used elsewhere in this thesis, and are described in Section 2.6.

### **6.3 Adsorption energy and optimised geometry for aromatic adsorbates**

The adsorption energy was calculated for anisole, benzene and nitrobenzene on Pt{111}, both with and without using the TS Van der Waals correction.

The results are shown in Table 6.1. The TS correction results in adsorption energies that are much more exothermic (by a factor of two to three). This is consistent with the overbinding that can be predicted by the TS correction.<sup>142</sup>

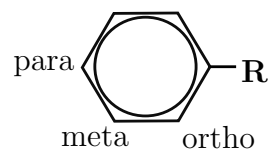
Adsorbate	$E_{\text{ads}} / \text{eV}$	$E_{\text{ads}} \text{ with TS} / \text{eV}$
anisole	-0.783	-2.19
benzene	-0.993	-2.09
nitrobenzene	-0.737	-2.08

**Table 6.1:** Table showing the adsorption energy with and without the TS Van der Waals correction.

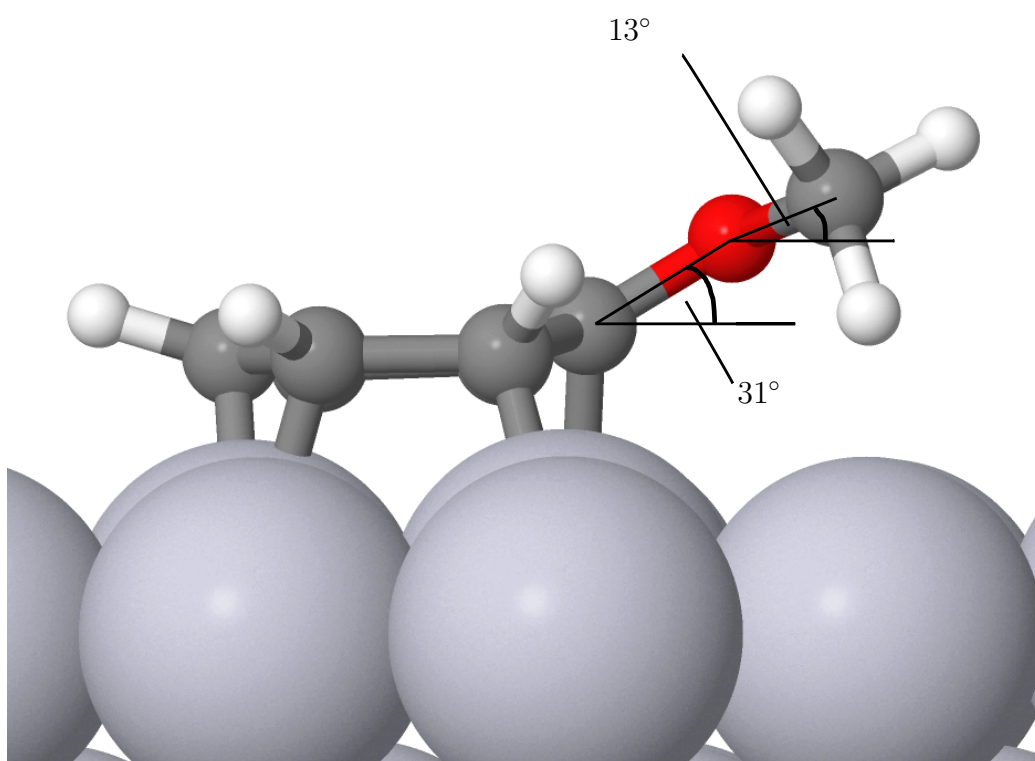
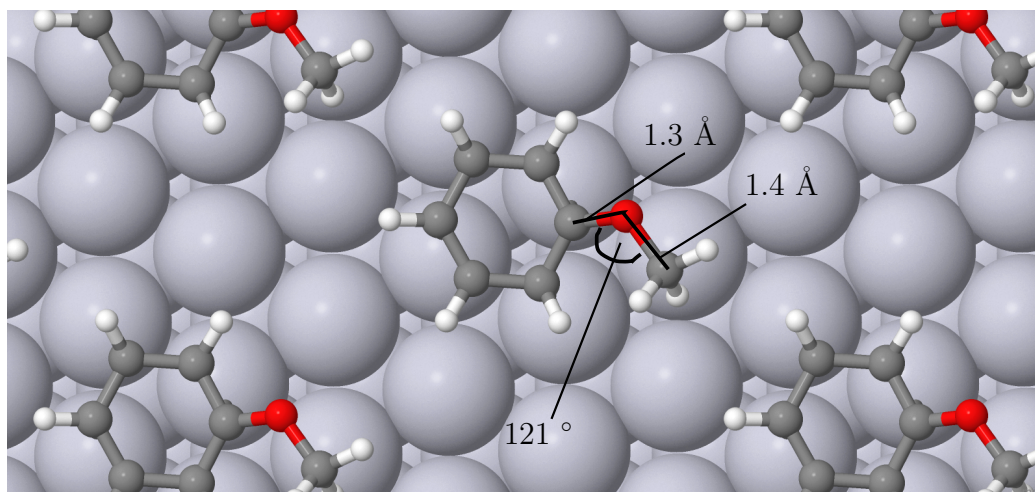
The more surprising result is that the order of the adsorption energies of anisole and benzene changes when the Van der Waals correction is switched on. Anisole is predicted to be bound less strongly than benzene without Van der Waals but with Van der Waals the prediction is for anisole to have the most exothermic binding of the three adsorbates. This can be understood as the methyl group of anisole causing only steric repulsion when Van der Waals interactions are not considered, but having favourable Van der Waals interactions that are included by the TS method. As there was very little difference in the geometries found with and without Van der Waals correction, the geometry found without Van der Waals was used to calculate the local and atomic softness.

Figure 6.2 shows the bond lengths and angles for anisole on Pt{111}. The diagrams in the upper and lower panels are top-down and side views illustrating the optimised structure obtained without using Van der Waals correction. With Van der Waals correction, the bond lengths were identical to 3 significant figures. The bond angles were also very similar with and without Van der Waals, except that the tilt between the oxygen and the methyl carbon was smaller with the TS correction, about  $8^\circ$  compared with  $13^\circ$  without Van der Waals. This smaller tilt from the plane parallel with the surface may be because of a weak Van der Waals attraction of the methyl group towards the surface, which is modelled more accurately using the TS correction.

The diagrams in Fig. 6.3 show the bond lengths and angles for nitrobenzene



**Figure 6.1:** Positions on an aromatic ring



**Figure 6.2:** Calculated bond lengths and angles for anisole on Pt{111}

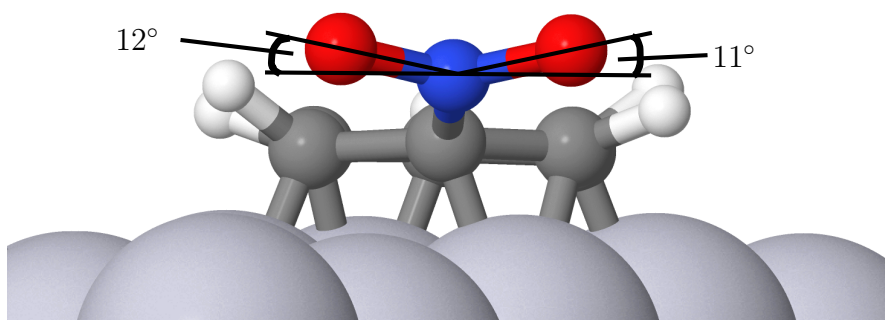
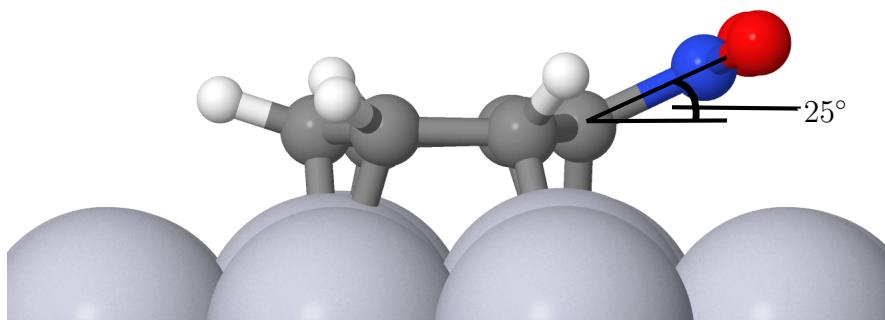
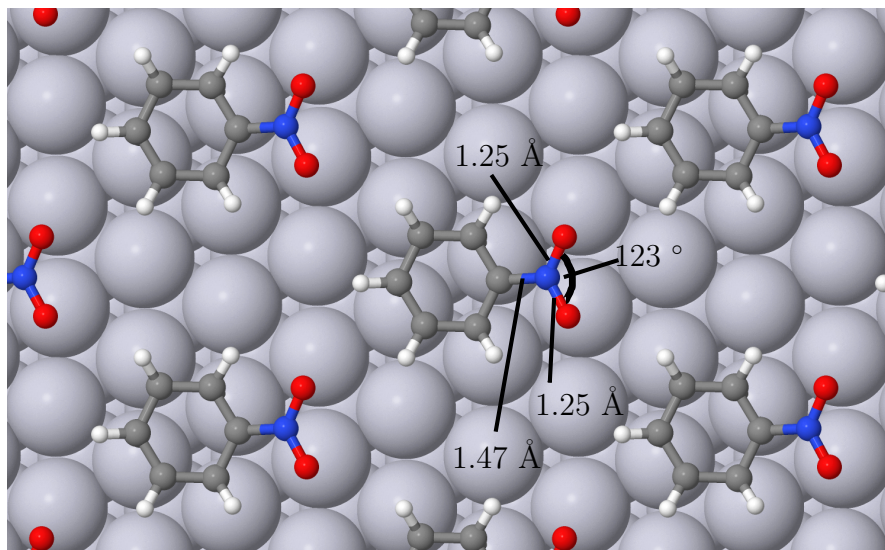


**Figure 6.3:** Calculated bond lengths and angles for nitrobenzene on Pt{111}

on Pt{111}. These were obtained for the optimised structure without using Van der Waals correction. With Van der Waals correction, the labelled bonds were the same length to three significant figures. The angles were also very similar, with the O-N-O angle identical to four significant figures. The tilt of the N-O bonds were slightly larger with Van der Waals, a percentage difference of one to two percent.

## 6.4 Local softness of aromatic adsorbates

Figures 6.4-6.7 show colourplots of the local softness calculated for the Pt{111} surface, with and without different aromatic adsorbates. Within the central unit cell, the local softness is plotted on an isosurface with a threshold of a fifth of the bulk valence-electron density. It should be noted that Figs. 6.4-6.7 use a different colour scale to Figs. 4.13-4.18 in Chapter 4. The colourplots in Chapter 4 use a scale from  $-0.1$  to  $3.7 \text{ eV}^{-1} \text{ \AA}^{-3}$  whereas the colourplots in this chapter use a scale from  $-1$  to  $3 \text{ eV}^{-1} \text{ \AA}^{-3}$ .

Surface	$s_{\min}(\mathbf{r})/ \text{ eV}^{-1} \text{ \AA}^{-3}$	$s_{\max}(\mathbf{r})/ \text{ eV}^{-1} \text{ \AA}^{-3}$
clean Pt{111} (1 × 1) 8+8	0.09	2.36
clean Pt{111} (3 × 3) 4+7	0.176	2.94
Pt{111}-benzene	-0.10	2.91
Pt{111}-anisole	-0.87	2.83
Pd{111}-nitrobenzene	-0.65	2.94

**Table 6.2:** Maximum values of local softness along a density isosurface with a threshold of a fifth of the bulk valence-electron density.

The minimum and maximum values of the local softness are compared in Table 6.2. The minimum value for the clean surfaces and for benzene were similar at about zero. The maximum values for the clean (3 × 3) 4+7 surface with and without benzene adsorbed were also very similar to each other. However, the local softness of the (1 × 1) surface with eight layers of slab and vacuum had a maximum that was smaller by about 22% than the (3 × 3) with four layers of slab and seven of vacuum. It may be that the higher softness of the latter surface was due to finite-size effects as the slab

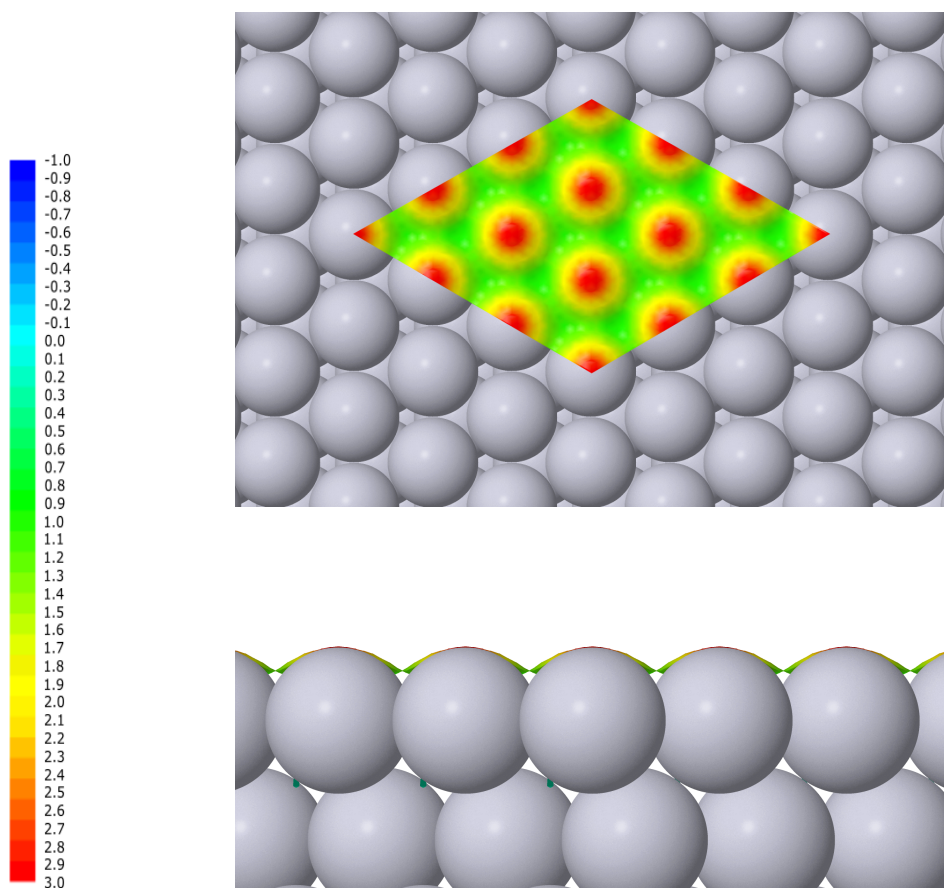


**Figure 6.4:** Colourplots of the local softness for the clean Pt{111} surface viewed from above (upper panel) and from the side (lower panel). The plots consist of isosurfaces of the density with a threshold of 1/5 of the bulk valence-electron density. The isosurface is coloured based on the local softness. The range of the colourplots was between  $-1$  and  $3 \text{ eV}^{-1} \text{ \AA}^{-3}$ .

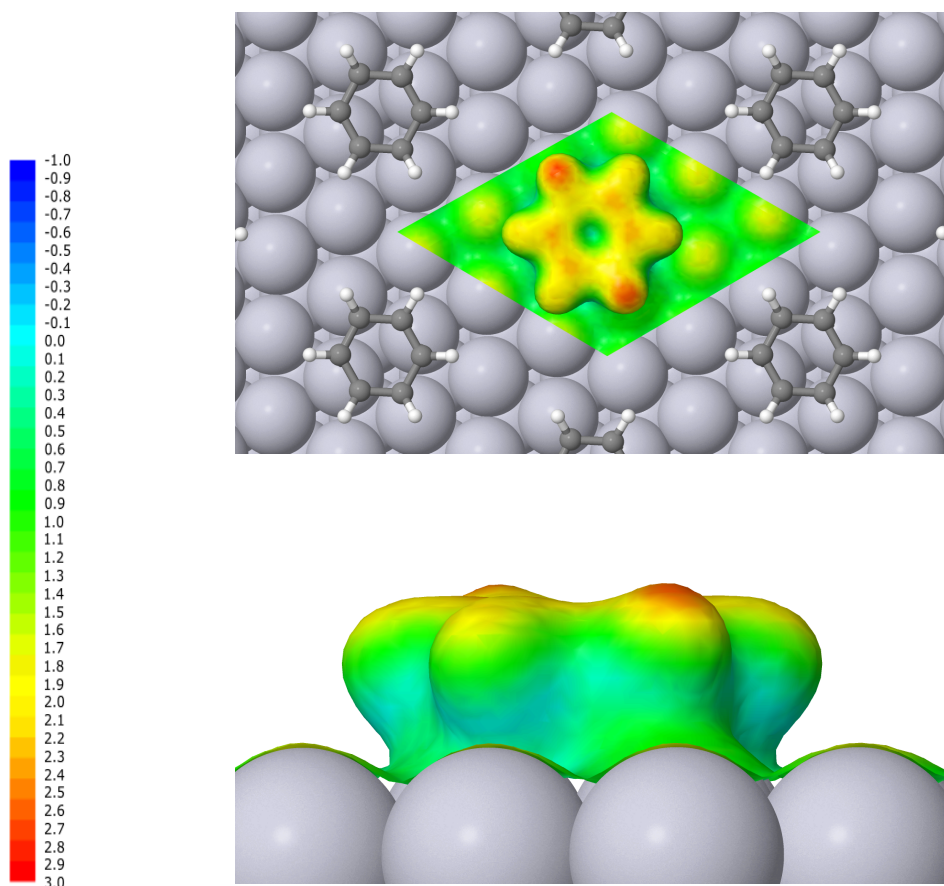


**Figure 6.5:** Colourplots of the local softness for benzene on the Pt{111} surfaces viewed from above (upper panel) and from the side (lower panel). The plots consist of isosurfaces of the density with a threshold of 1/5 of the bulk valence-electron density. The isosurface is coloured based on the local softness. The range of the colourplots was between -1 and  $3 \text{ eV}^{-1} \text{ \AA}^{-3}$ .

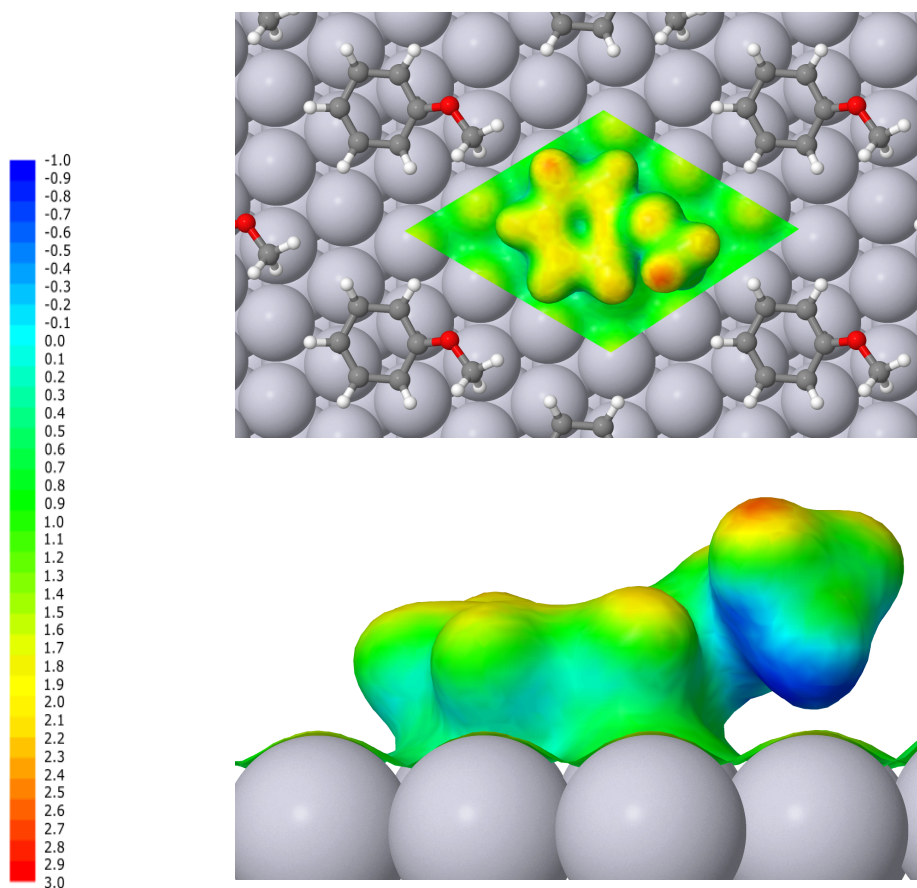


**Figure 6.6:** Colourplots of the local softness for anisole on the Pt{111} surfaces viewed from above (upper panel) and from the side (lower panel). The plots consist of isosurfaces of the density with a threshold of 1/5 of the bulk valence-electron density. The isosurface is coloured based on the local softness. The range of the colourplots was between -1 and  $3 \text{ eV}^{-1} \text{ \AA}^{-3}$ .

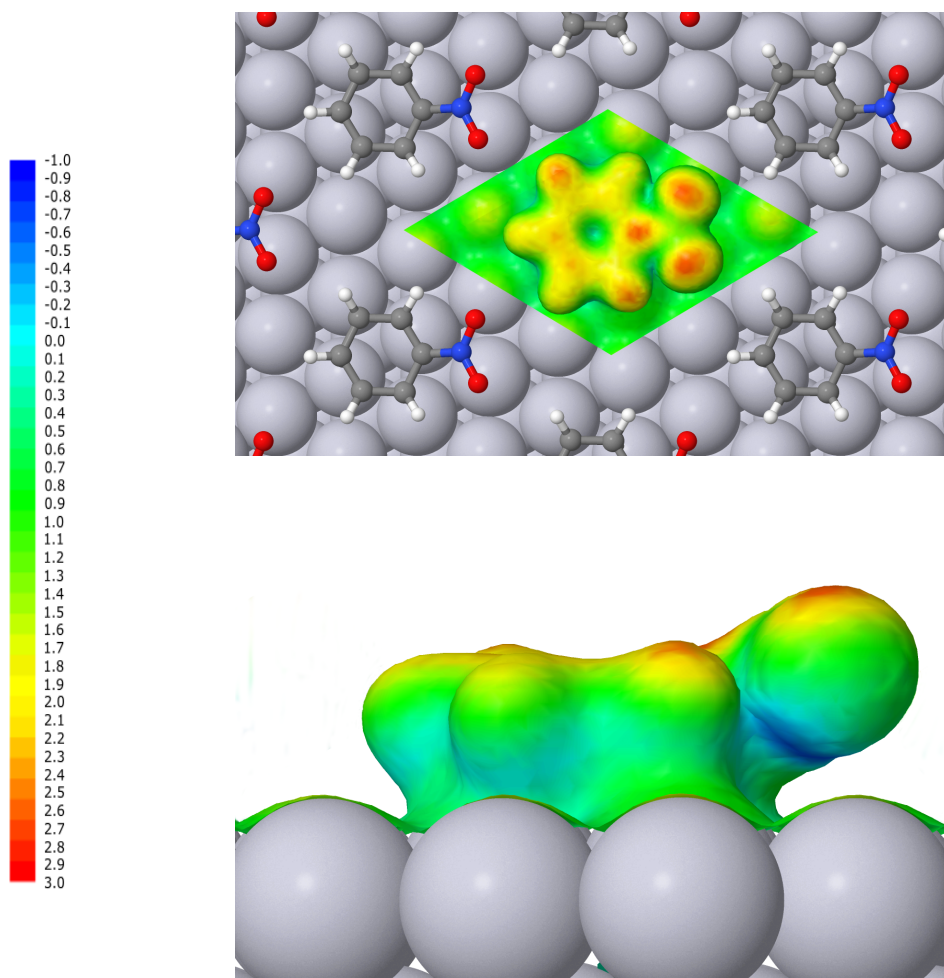


**Figure 6.7:** Colourplots of the local softness for nitrobenzene on the Pt{111} surfaces viewed from above (upper panel) and from the side (lower panel). The plots consist of isosurfaces of the density with a threshold of 1/5 of the bulk valence-electron density. The isosurface is coloured based on the local softness. The range of the colourplots was between -1 and  $3 \text{ eV}^{-1} \text{ \AA}^{-3}$ .

had only four layers. This higher softness means that it can be predicted that a thin metal film with only four metal layers would be more reactive than a metal slab with eight metal layers. This would generally be expected to be the case. While the  $(3 \times 3)$  4+7 surface with and without aromatic adsorbates had a maximum value of about  $2.9 \text{ eV}^{-1} \text{ \AA}^{-3}$ , the minimum values differed. In all the clean surfaces studied in Chapter 4, the minimum value was very near zero. This was also the case for the clean  $(3 \times 3)$  4+7 supercell. However, with anisole and nitrobenzene adsorbed the minimum local softness was much lower, at  $-0.87$  and  $-0.65 \text{ eV}^{-1} \text{ \AA}^{-3}$  respectively.

Figure 6.5 shows the local softness of benzene on Pt{111}. The values are plotted on a density isosurface with a threshold of a fifth of the bulk valence-electron density. In Fig. 6.5 the absolute range of values of the local softness is similar to that of the clean surface in Fig. 6.4. However, the way that regions of high local softness are distributed is rather different. For example, the local softness above the top layer of platinum atoms is much less with benzene adsorbed than for the clean surface. The local softness above the top layer of the clean metal surface ranges from about  $1\text{-}2.9 \text{ eV}^{-1} \text{ \AA}^{-3}$ . In contrast, the local softness above top-layer atoms with benzene adsorbed ranges from about  $1\text{-}1.8 \text{ eV}^{-1} \text{ \AA}^{-3}$ . This predicts that even metal atoms that are not directly obscured by the benzene molecule will nevertheless be somewhat deactivated electronically. The range of local softness above the top layer of metal atoms is very similar with anisole and nitrobenzene compared with benzene, which suggests that the deactivation would be similar for these different adsorbates.

In order to be sure that this deactivation of the top layer of atoms is a valid result and not a feature of the denominator being different for the surfaces with adsorbates, the atomic softness was compared for different layers with and without adsorbates. This is discussed in Section 6.6. It was found that the middle layers of the slab had very similar atomic softness with and without different adsorbates. This suggests that the difference in the local softness of the top layer is a genuine effect.

The density isosurface the local softness is plotted on for Pt{111} - benzene

bounds a roughly crown-shaped region. The highest values of the local softness are on the upper surface of this shape, not on the sides. Platinum atoms fall into one of three groups based on whether they are bound to two, one or zero carbons. Based on the approach of Yamagishi et al<sup>145</sup> these were designated type I, II or III respectively. Similarly, the carbon atoms fall into two distinct groups. The carbons bound to type I Pt atoms (carbons which share their Pt atom with another carbon) had higher local softness than those bound to type II platinum atoms. The hydrogen atoms of the benzene also fall into two groups, those that are bound to a carbon that is in turn bound to a type I or a type II platinum atom. The maximum in the local softness (about  $2.9 \text{ eV}^{-1} \text{ \AA}^{-3}$ ) is found over the two hydrogens that are above type II sites. This means that the hydrogens that have the highest local softness are bound to carbons that do not have to share their platinum atom with any other carbons. The hydrogens above type II sites are apparently softer than the carbons they are bonded to. In contrast, the hydrogens above the type I sites are harder than the hydrogens above type II sites and also harder than the carbon atoms they are bonded to.

Figures 6.6 and 6.7 show the local softness plotted on a density isosurface for anisole and nitrobenzene. In each case, the patterns of the local softness within the ring are similar to those obtained for benzene, which suggests that the electronic interaction with the metal is more important for determining the directing effects than the interaction with the side group. This is similar to the results found by Tan and co-workers.<sup>144</sup> For example, there is more difference between the local softness over hydrogens above type II sites versus type I sites than between hydrogens above type I sites that are at ortho, meta and para positions relative to the side group. This suggests that the binding to the metal weakens the  $\pi$  conjugation with the side group.

For anisole on Pt{111}, the highest local softness ( $2.2\text{-}2.9 \text{ eV}^{-1} \text{ \AA}^{-3}$ ) is on the upper surface of the molecule, specifically above the hydrogens on the methyl group that point away from the surface. Of those two hydrogens, the one that points towards the ring has higher local softness of about  $2.9 \text{ eV}^{-1} \text{ \AA}^{-3}$ . Interestingly, the region below the methyl group (below and to the side of

the methyl hydrogen that points towards the surface) has negative local softness of about  $-0.8 \text{ eV}^{-1} \text{ \AA}^{-3}$ . This suggests that the hydrogen that points down towards the surface is much harder than the two hydrogens that point up.

For nitrobenzene, the highest values of local softness are again on the upper surface of the molecule. These high values are localised above the oxygen atoms and above the carbon atom that is bound to the nitrogen of the  $\text{NO}_2$  group. There are also higher values over the two hydrogens on the phenyl ring that are directly above type II atoms. The oxygens on the  $\text{NO}_2$  group exhibit an interesting pattern of local softness as above they are positive but below they are negative. Analogously to the side group of anisole, below the  $\text{NO}_2$  group on nitrobenzene there is a region of negative local softness, of about  $-0.6 \text{ eV}^{-1} \text{ \AA}^{-3}$ . The regions of negative local softness below the side groups of anisole and nitrobenzene may be due to the strain of the groups that are repelled away from the surface. It would be interesting to look at this in more detail in the future.

Interestingly, there does appear to be a difference between the reactivity of the carbons that are bound to type I platinum atoms and that are para and meta as opposed to ortho to the side group. The carbons that are para and meta to the side group have a higher softness (about  $2.5 \text{ eV}^{-1} \text{ \AA}^{-3}$ ) compared with the carbon at the ortho position (about  $2.1 \text{ eV}^{-1} \text{ \AA}^{-3}$ ). However, this is less of a difference than that between the hydrogens above type I and type II platinum atoms. It may be that the lower local softness at the ortho positions is due to the electronegative and  $\sigma$ -withdrawing  $\text{NO}_2$  group. If it was due to  $\pi$  conjugation with the  $\text{NO}_2$  group then one would expect the ortho and para positions to be similar rather than the actual observed similarity, which is between the para and meta positions.

It should be noted that while the local softness is a measure of which areas in a molecule can be predicted to respond to an increase in electron density, regions of high local softness will not necessarily be the most reactive. In order for a reaction to occur, bonds would need to be broken, so there are other factors (such as bond strength) that determine the rate of reactions at

different sites on the molecule and surface. Nevertheless, the local softness of aromatic adsorbates gives useful data for understanding directing effects and predicting reactivity. In order to find complementary insight to the picture obtained from the local softness, it would be interesting to look at the softness of individual atoms on adsorbates as well. For this reason, the atomic softness of aromatic molecules was studied on platinum.

## 6.5 Visualising the atomic softness of aromatic molecules on platinum

Figures 6.8 and 6.9 show the atomic softness of Pt{111} with and without aromatic molecules adsorbed. The platinum atoms on the top layer of the clean metal surface had a much higher atomic softness (about  $21 \text{ eV}^{-1}$ ) compared to those with adsorbates present (from about  $6\text{-}12 \text{ eV}^{-1}$ ). For type I platinum atoms, which were bound to two carbon atoms, the atomic softness was about  $6 \text{ eV}^{-1}$ . For type II platinum atoms, which were bound to one carbon atom, the atomic softness was about  $8 \text{ eV}^{-1}$ . Type III platinum atoms, which were not bound to any carbon atoms, had the highest atomic softness in the top layer, of about  $11\text{-}12 \text{ eV}^{-1}$ . This variation in deactivation over the surface could be used to make predictions of where additional molecules might adsorb. It could also be predicted that the clean metal surface is more reactive than the same metal surface with a molecule adsorbed. The atomic softness shows the patterns of deactivation of Pt more clearly than the local softness, due to the way in which the local softness is displayed on a density isosurface.

The directing effects for benzene are similar to those already noted for the local softness. The hydrogens above the type II sites have an atomic softness of about 20, which is significantly higher than those above the type I sites by about  $13.5 \text{ eV}^{-1}$ . In contrast, the carbon atoms bound to type II platinum atoms have a lower local softness than those bound to type I platinum atoms. In the anisole and nitrobenzene aromatic rings, the directing effects are relatively similar to those for benzene. The overall directing effects

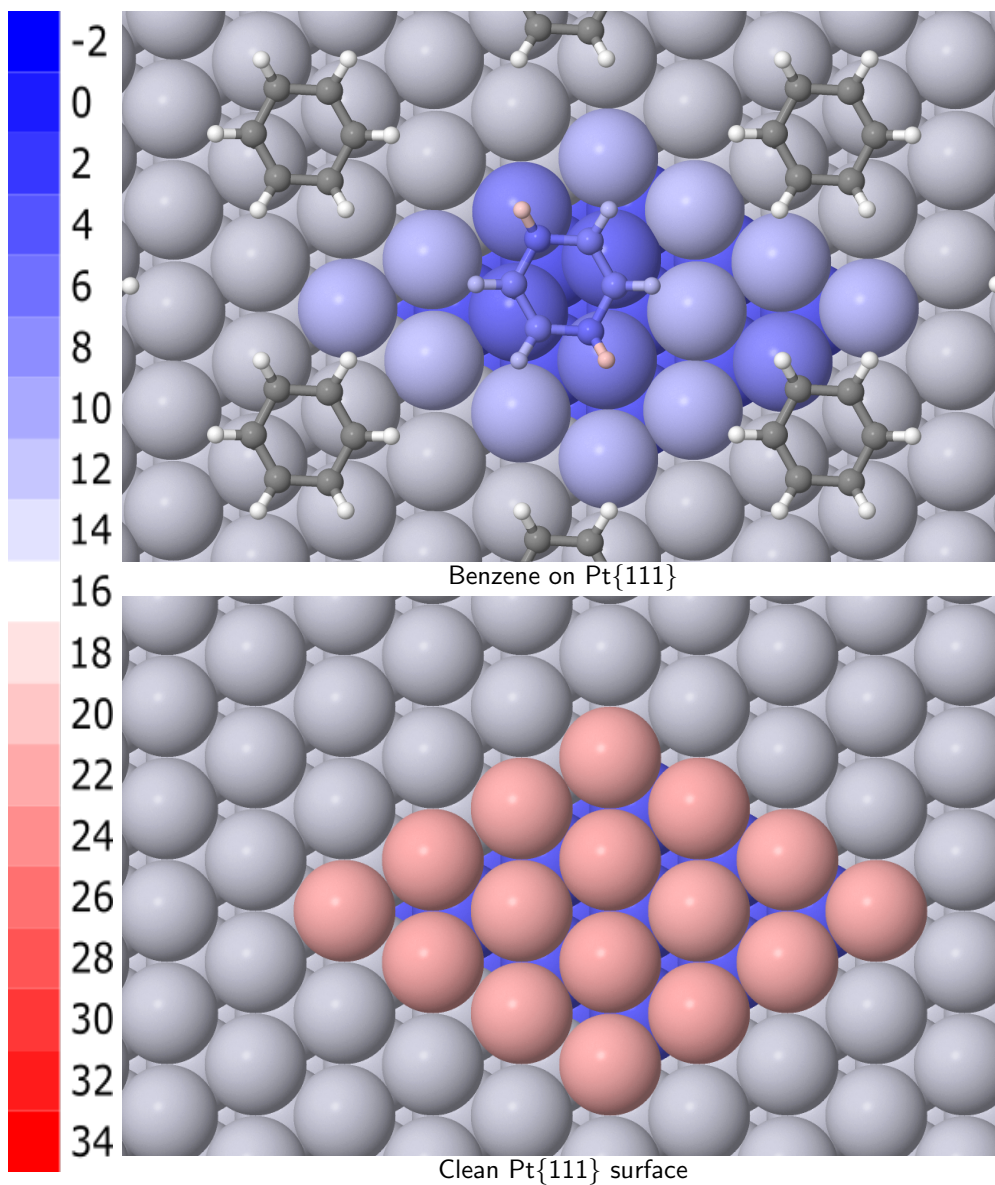


**Figure 6.8:** Atomic softness of the Pt{111} surface, with and without benzene adsorbed. The atoms in the central unit cell are coloured according to the values of the atomic softness. The range of the atomic softness was between -2 and 34 eV<sup>-1</sup>.

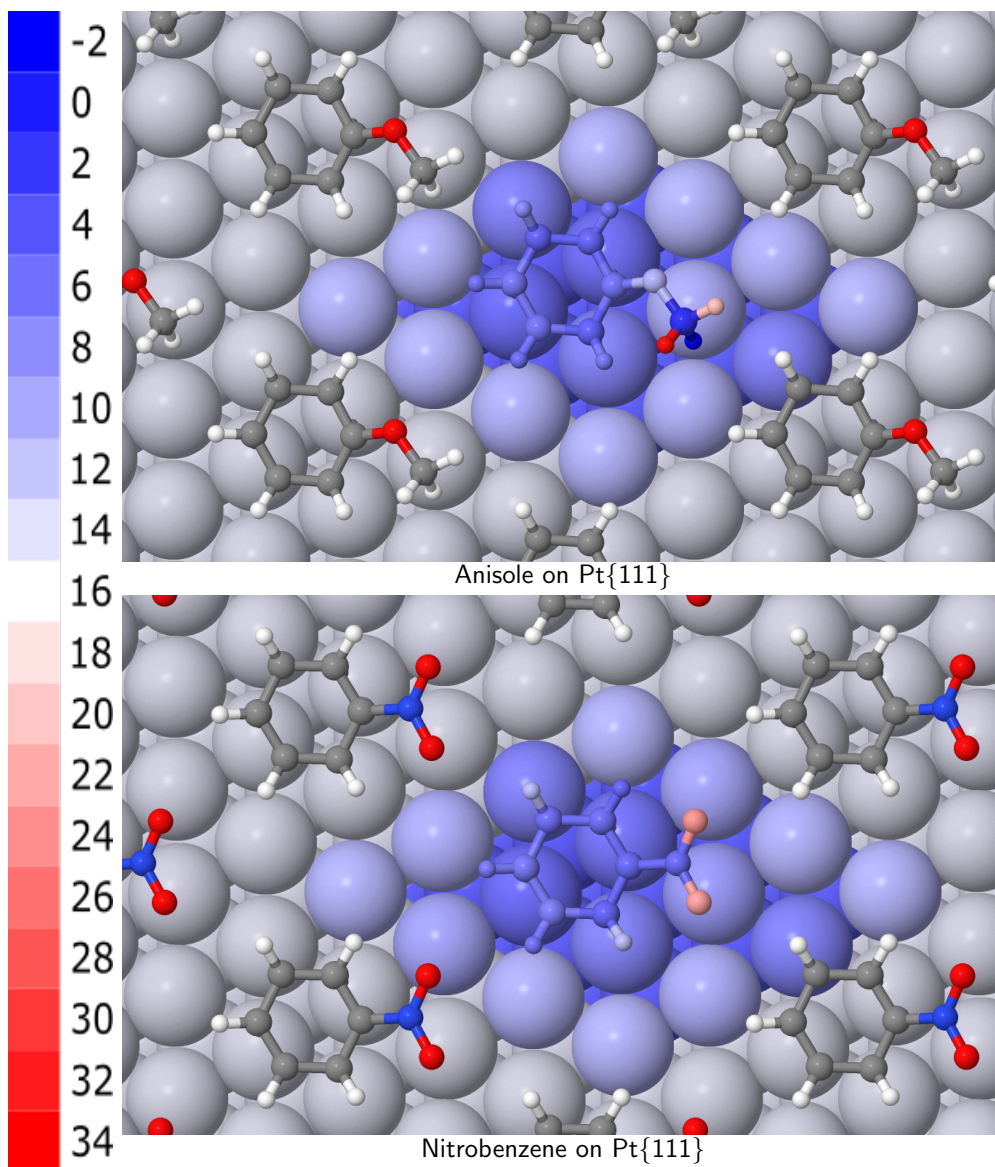


**Figure 6.9:** Atomic softness of the Pt{111} surface, with anisole and nitrobenzene adsorbed. The atoms in the central unit cell are coloured according to the values of the atomic softness. The range of the atomic softness was between -2 and 34 eV<sup>-1</sup>.

are a little less clear in the atomic softness compared with the local softness. This is probably because the local softness was plotted on an isosurface above the molecule, and that happens to be where the highest values of the local softness are.

The atomic softness of the side group in anisole is a little surprising in that the set of hydrogens on the methyl group in anisole contain both the softest and hardest atoms in the molecule, at 33 and  $-1.2 \text{ eV}^{-1}$  respectively. The carbon on the methyl group is relatively hard as well, with a softness of about  $2.3 \text{ eV}^{-1}$ . The oxygen has a larger value of the atomic softness than any of the carbons on the ring, at about  $11 \text{ eV}^{-1}$ .

For nitrobenzene the softest atoms were the oxygens in the  $\text{NO}_2$  group, at 22.3 and  $23.2 \text{ eV}^{-1}$ . The nitrogen in the  $\text{NO}_2$  group had a similar atomic softness to the carbons in the ring, at about  $6 \text{ eV}^{-1}$ . Within the anisole phenyl ring, the hardest carbons were those attached to a type II platinum. This matches the trends for benzene. However, for nitrobenzene, while these atoms are among the hardest carbon atoms, they are joined by the carbon directly bonded to the nitrogen, which is also relatively harder. This may be due to the  $\text{NO}_2$  group withdrawing electron density. As mentioned in terms of the trends in the local softness, among the three carbons that are bound to type I platinum atoms, the one at the para position is more similar in softness to that at the meta position than to that at the ortho position. This suggests that  $\sigma$  induction of electrons from the electron withdrawing  $\text{NO}_2$  group is more important than  $\pi$  conjugation in determining the local softness of phenyl carbon atoms.

## 6.6 Testing the approximation of using the clean-surface denominator

A measure of how reasonable it might be to compare the absolute values of the local and atomic softness between sites on surfaces with different adsorbates can be obtained by comparing the softness of the metal atoms in the

middle of the slab. When this was done, the atomic softness of middle-layer atoms was very similar for the clean ( $3 \times 3$ ) calculation and for those with benzene, anisole and nitrobenzene adsorbed. The percentage difference between the middle-layer atoms with different adsorbates was 0.2-1.5%. The difference between the atoms in the middle two layers for the clean ( $3 \times 3$ ) surface compared with that with adsorbates was only slightly larger, at about 2.5%.

The average atomic softness of the bottom layer was a bit more surprising, as the atomic softness decreased in the presence of adsorbates, despite the two metal atom layers separating the bottom layer and the top layer the adsorbates were placed on. The percentage difference was about 11-15%. This was a smaller change than that for the type III atoms in the top layer, which decreased in atomic softness by about 50%. It is likely that if the number of slab layers was increased, then there would be more screening between the top and bottom layers and then the bottom layer would not be significantly affected by the presence of an adsorbate on the opposite surface of the slab. However, the key result is that the atomic softness in the middle of the slab is very similar with and without different adsorbates. This suggests that the approximation that the denominator will be the same for the clean surface as for the surfaces with adsorbates is a reasonable one, at least for these three adsorbates.

## 6.7 Summary

The local and atomic softness of aromatic molecules on Pt{111} yield interesting information about directing effects. In particular, the hydrogens and carbons in the benzene ring could be classified as two groups based on whether the carbon is bound to a type I or type II platinum atom, with distinct local and atomic softness for each. This could lead to predictions about reactivity. The effect of the metal surface on the electronic properties of the ring was found to be more significant than the effect of  $\pi$  conjugation with the side group. However, for anisole and nitrobenzene there was some difference

between the carbons attached to type I platinum atoms in the ortho, meta and para positions relative to the side group. The carbons at the para and meta positions had similar softness, whereas the ortho position carbon had lower local and atomic softness. As  $\pi$  conjugation would generally lead to similar reactivity at the ortho and para positions, this suggests that the side group influences the reactivity of the ring through  $\sigma$  inductive effects due to the electronegative heteroatom more than by  $\pi$  conjugation. The local and atomic softness give understanding that is complementary to the more standard DFT approach followed by Tan et al. To summarise, the local and atomic softness predicts that for these aromatic adsorbates the interaction with the metal was more important than the side group for determining the softness of atoms in the aromatic ring.

# Chapter 7

## Summary and Outlook

Understanding the reactivity of metal surfaces is an important problem in catalysis. Reactivity indices are a helpful tool in order to predict the properties of different sites in model catalysts. For metal surfaces, various reactivity indices have been proposed. These have a variety of limitations and drawbacks. There is a need for a reactivity index that can be calculated for metal surfaces and adsorbates and that can yield both local and atomistic information about reactivity.

In this work a new method for calculating the local softness was developed. This method used the theoretical framework of DFT, using the plane-wave code CASTEP. The key step in the calculation of the local softness was using the chain rule to calculate the partial derivative of the local electron density by the chemical potential, in terms of derivatives by the surface charge  $\sigma$ . This approach allows the problem to be divided in order to calculate the numerator and denominator of local softness. The former is the partial derivative of  $\rho(\mathbf{r})$  with respect to the surface charge and the latter is the partial derivative of  $\mu$  with respect to the surface charge.

While the numerator of local softness was relatively easy to calculate, finding the denominator was more challenging. This was because of the limitations of using a plane-wave code, which requires periodic boundary conditions.

Calculating the derivative of the chemical potential with respect to the surface charge requires calculating energies for charged calculations. This is a problem as the local softness is defined as the derivative of the local electron density with respect to the chemical potential, at constant external potential  $v(\mathbf{r})$ . Unfortunately, the way CASTEP deals with charge in periodic boundary conditions involves adding a corrective potential. In order to find the derivative in a way that is independent of the external potential it is necessary to extrapolate to find the denominator of local softness at infinite slab and vacuum thickness.

An additional problem arises from the way in which CASTEP defines the energy origin. The problem with this is that the potential of the supercell is different for different supercell geometries and for different charges, therefore the energy reference for different calculations varies. This meant that it is difficult to extrapolate the denominator of local softness to infinite slab and vacuum thickness. In order to solve this problem, it is necessary to correct for the change in energy reference by subtracting an energy that should be constant with respect to supercell geometry and charge. Therefore this quantity only varies due to the change in energy reference and can be used to eliminate the dependence on energy reference.

Several different properties were investigated in order to correct the denominator. The most promising method was performing a spectral task to find an accurate band structure, then using OptaDOS to calculate a very accurate DOS. The cross-correlation of the lowest 5 eV of the DOS could then be used to find the energy shift with charge, and correct the denominator of local softness. This method was used in order to correct the dependence on the CASTEP energy reference, and then the result was extrapolated to infinite slab and vacuum thickness for a constant ratio of 1:1 slab to vacuum thickness.

## 7.1 Analysing the local softness of clean metal surfaces

The above method was used to find the local softness for eighteen metal surfaces. These consisted of three coinage metals (copper, silver and gold) and three transition metals (rhodium, palladium and platinum). Three facets were studied: the flat  $\{111\}$  and  $\{100\}$  facets and the stepped  $\{110\}$  facet. As the local softness is a scalar field in three dimensions, it was necessary to find a way to visualise it. Criteria for visualisation of complex data include clarity and chemical insight. The local softness was visualised as isosurfaces for the copper surfaces. These isosurfaces showed that the regions of highest local softness were above the top layer of atoms. There were also regions of higher local softness along close-packed rows. There appeared to be higher local softness for the stepped Cu $\{110\}$  surface than the flat copper surfaces, based on comparing the volume of space that had values of  $s(\mathbf{r})$  within the local softness threshold value.

In order to gain additional insight into the range of local softness values at the surface, colourmaps were plotted. These consisted of a density isosurface at a particular density threshold value, which was coloured based on the local softness at each point on the surface. By increasing the density isosurface threshold then points closer and closer to the atom centres will be sampled. For the figures in Chapter 4, two density thresholds were used, of  $1/5$  and  $1/3$  the bulk valence-electron density. The former resulted in a corrugated surface that would be similar to the topology experienced by an approaching molecule. The latter resulted in a more atomistic region, which did not form a continuous surface when viewed from above.

The local softness colourplots gave insight into predicting reactivity on the surfaces studied. For example, the maximum values on the density isosurfaces for the nine transition-metal surfaces were all larger than any of the maximum values for the nine coinage-metal surfaces. This suggests that the adsorption energy for a molecule like CO will be more exothermic for the transition metals than for the coinage metals (which was later found to be the case).

Also, the three-fold hollows on the  $\{111\}$  surfaces were found to have a higher local softness than the four-fold hollows on the  $\{100\}$  surfaces. This suggests that small molecules such as CO would be more likely to bind in a hollow site on  $\{111\}$  than on  $\{100\}$ .

## 7.2 Calculating the atomic softness for clean metal surfaces

The local softness gives useful information that can be used to predict the reactivity of different surfaces at a range of locations. However, it would be useful to have a measure of the softness of an individual site or atom. Therefore the atomic softness was calculated, as the integral of the local softness over the volume of space occupied by a specific atom. The atomic softness was calculated for the same 18 surfaces and was used to predict the adsorption energy of CO at both the literature-preferred adsorption site and at the atop site. It was found that large-scale trends in CO adsorption energy were predicted well by the atomic softness of top-layer atoms. The atomic softness of top-layer transition-metal atoms was higher than the atomic softness of any of the top-layer coinage-metal atoms. This result was matched by the CO adsorption energies, which also fell into two discrete groups of coinage and transition metals, with no crossover between the two sets. Overall there was a linear trend where for larger atomic softness, the adsorption energy was more negative (exothermic).

However, there were some limitations to using the atomic softness to predict the CO adsorption energy. The atomic softness was not so good at predicting differences in reactivity between elements that were similar to each other. There was also a lot of noise in the graph of atomic softness versus adsorption energy, especially for the adsorption energy at the literature-reported minimum-energy adsorption site. For example, the atomic softness of step-edge atoms was higher for the stepped transition-metal surfaces than for any of the terrace atoms on the flat surfaces. This means that the CO adsorption energy could be expected to be higher for these surfaces. However, this was

not necessarily the case, and while the most negative atop adsorption energy was obtained for the stepped Pt{110} surface, the next lowest adsorption energy was for the flat Pt{100} surface. Therefore, while the atomic softness is good at predicting large scale differences, it may be less accurate at predicting the fine detail between surfaces that are similar in reactivity.

### 7.3 Using the chemical softness to predict directing effects in aromatic adsorbates

As described in Sections 7.1-7.2, the local and atomic softness can be useful for studying the reactivity of clean metal surfaces and for predicting the adsorption energy of a small, simple adsorbate on different surfaces. One of the most interesting applications for a reactivity index is studying the properties of adsorbates as well as clean metal surfaces. In particular, directing effects in aromatic rings are an interesting application where it would be helpful to have more understanding of the relative strength of electronic coupling with the side group versus the metal surface. For this reason, the local and atomic softness were calculated for a Pt{111} ( $3 \times 3$ ) surface, both with and without three aromatic adsorbates. The adsorbates studied included a  $\pi$ -acceptor (nitrobenzene), a  $\pi$ -donor (anisole), and a control aromatic molecule with no  $\pi$ -conjugating side group (benzene). Benzene represents the simplest case, where the only modification to the  $\pi$ -bonding within the ring would be due to the metal surface. As discussed in Section 6.4, the platinum atoms with benzene adsorbed fall into three groups, depending on whether they are bound to two carbons (type I), bound to one carbon (type II) or not bound to any carbons (type III).

In all cases, the local softness was highest over the adsorbates rather than over the uncovered metal atoms between adsorbates. For benzene, the maxima in the local softness occurred above the hydrogens above type II platinum atoms and (to a lesser extent) the carbons above the type I platinum atoms. For anisole and nitrobenzene, the picture was made more complex by adding a side group. The three carbon atoms above type I platinum atoms, which are

not directly bound to the side group, can be classified as ortho, meta or para, depending on how near to the side group they are (for a labelled diagram, see Fig. 6.1). There are also two carbon atoms above type II platinum atoms, one ortho and one meta. Based on conventional wisdom, one would expect to see similar local and atomic softness on the ortho and para carbons and different reactivity for the meta carbons. However, the clearest trend is for the reactivity of the carbons above type I platinum atoms to be different to the carbons above type II platinum atoms, irrespective of whether they are ortho, meta or para. This suggests that the interaction with the metal surface is more important than the interaction with the side group for determining reactivity. In other words, the interaction of the ring with the metal surface decreases the  $\pi$  conjugation with the side group. There is a difference between the ortho carbons above type II platinum atoms and the meta and para carbons above type II platinum atoms for nitrobenzene, but this is more likely to be consistent with  $\sigma$  induction than  $\pi$  conjugation with the side group.

In addition to the directing effects in the aromatic ring, the local and atomic softness of the side groups themselves were investigated. For anisole, the lowest and highest local softness were found for different hydrogen atoms on the methyl group. In fact, the atomic softness for the atom that pointed down, towards the surface, was negative. This suggests that based on conformation with respect to the metal surface, the hydrogens in the methyl group of anisole have very distinct reactivity. The theme of the underside of the side group having negative local softness was continued for nitrobenzene, where the local softness of the underside of the  $\text{NO}_2$  group was also negative, though not as negative as the underside of the OMe group in anisole. These negative regions of the local softness represent areas where the local electron density would decrease in response to an overall increase in chemical potential. It is possible that this occurs due to strain on the side of the bond that might be expected to be tilting away from the surface (due to steric repulsion). It would be interesting to look at this in more detail in further work.

In terms of the reactivity of the platinum atoms, the general trend is deactivation in the presence of any adsorbate. This is the case even for type III platinum atoms which do not directly bind to any carbon atoms. However, the strongest deactivating effect is for type I platinum atoms (which are bound to two carbon atoms), followed by type II and then type III. It would be interesting to do more work on understanding the effect of deactivation of metal surfaces when different adsorbates are present.

## 7.4 Further work

As mentioned in the previous section, it would be interesting to further investigate the possible effects of strain in causing negative local softness. The strain under the side group arises due to steric repulsion with the metal surface. It would be helpful to investigate how the local softness is affected by other types of strain in an adsorbate. For example, the adsorption of cycloalkanes could be used to compare transannular strain with the effect of ring strain.

Another application for further research is the observation that the local and atomic softness can yield insight into the deactivation of a metal surface in the presence of an adsorbate. It would be interesting to compare the deactivation region for larger and larger lateral dimensions of the supercell. Then it could be found what size of supercell is needed in order for the type III platinum atoms to have an atomic and local softness that is similar to that of the clean surface. It would also be helpful to compare the deactivating effects for different adsorbates. The effect of the three aromatic adsorbates appeared to be similar but perhaps certain classes of molecule might be more or less deactivating. In particular, it would be interesting to study the electronic effect of poisoning on a catalytically relevant metal surface. This would give insight into a catalytically important problem, and might result in understanding that could help solve the problem of catalyst poisoning.

In the literature it is well documented that step-edge and kink sites are more reactive than any terrace sites on flat surfaces such as Cu{111} and

Cu{100}.<sup>18,146</sup> However, there is some debate over the relative order of reactivity of kink sites and step-edge sites.<sup>30</sup> It would be interesting to have a quantitative measure of the reactivity of step and kink sites from a variety of surfaces. The local softness could be used to predict whether there will be a quantitative difference in the reactivity, and whether more highly-corrugated surfaces have more reactive step and kink atoms. This kind of analysis using  $s(\mathbf{r})$  would be helpful in finding and characterising active sites. In order to investigate this, the local and atomic softness could, for instance, be calculated for the stepped {331} and the kinked {210} surfaces.

In addition, it has been shown in Chapter 5 that there is a correlation between the atomic softness of top-layer atoms and the adsorption energy of CO. It would be interesting to compare the atomic softness of top-layer atoms with the adsorption energy of some other small inorganic molecules (e.g. NO, O<sub>2</sub>, H<sub>2</sub>O and H<sub>2</sub>S). The correlation between the atomic softness and adsorption energy could then be compared between different adsorbates. It would be interesting to see how the correlation varied between the adsorption energy of softer or harder adsorbates. For example, whether the adsorption energy of H<sub>2</sub>S had a stronger correlation with the atomic softness than the analogous harder molecule, H<sub>2</sub>O.

As mentioned earlier in Section 1.4, BEP linear relations are found to generally hold for most metal-adsorbate combinations. They are a convenient way to separate electronic and geometric effects. In addition they have useful predictive power that extends to enabling catalyst design via Sabatier analysis.<sup>1</sup> As the slope of a BEP line is related to the electronic properties of the system, it may be well predicted by the local softness. Therefore studying the relation with the activation energy for activation and desorption and local softness would be interesting, as these should be linearly related also. Predicting BEP lines as mentioned above would be a test of to what extent catalytic activity can be predicted from the clean metal and adsorbate alone. This may shed light on the ongoing debate in this topic.<sup>12</sup>

## 7.5 Conclusions

The local softness and atomic softness are promising reactivity indices for studying heterogeneous catalysis. The local softness gives chemical insight into how the reactivity of different regions in space varies close to a surface. It can also be used to make quantitative predictions of the reactivity of different sites on various surfaces. The atomic softness gives insight into the overall reactivity of specific metal or adsorbate atoms on a surface. Both measures can be used to predict the reactivity of clean metal surfaces. The atomic softness can also be used to predict the adsorption of small molecules such as CO. In addition, unlike some other reactivity indices, the local and atomic softness can be calculated for both metal surfaces and adsorbates and have yielded significant insight into the ring directing effects for aromatic adsorbates. Overall, the local and atomic softness are useful tools in order to study heterogeneous catalysis.

# Appendix A

## Computational Details

### A.1 Calculation of lattice constants

The lattice constants were calculated using CASTEP with an energy cutoff of 340 eV. The  $\mathbf{k}$  points used to calculate the lattice constant were  $6 \times 6 \times 6$  in most cases as by then there was not much difference in energy when more  $\mathbf{k}$  points were added.

It should be noted that a slightly different lattice constant was inadvertently used for the Pd{111} and Cu{100} surfaces compared with the other surfaces of each metal. The lattice constant used for the Pd{100} and Pd{110} surfaces was calculated using  $12 \times 12 \times 12$   $\mathbf{k}$  points. For the Cu{100} a value calculated earlier by a co-worker was used inadvertently (Marco Sacchi, personal communication, Nov. 13th, 2013) The percentage difference between lattice constants for the copper surfaces was about half a percent so is unlikely to have affected calculations much. Similarly, the percentage difference between the lattice constant used for the palladium surfaces was only about a quarter of a percent.

Surface	Lattice constant / Å	$k$ points
Rh{111}	3.84	$6 \times 6 \times 6$
Rh{100}	3.84	$6 \times 6 \times 6$
Rh{110}	3.84	$6 \times 6 \times 6$
Pd{111}	3.90	$6 \times 6 \times 6$
Pd{100}	3.89	$12 \times 12 \times 12$
Pd{110}	3.89	$12 \times 12 \times 12$
Pt{111}	3.96	$6 \times 6 \times 6$
Pt{100}	3.96	$6 \times 6 \times 6$
Pt{110}	3.96	$6 \times 6 \times 6$
Cu{111}	3.60	$6 \times 6 \times 6$
Cu{100}	3.62	unknown
Cu{110}	3.60	$6 \times 6 \times 6$
Ag{111}	4.12	$6 \times 6 \times 6$
Ag{100}	4.12	$6 \times 6 \times 6$
Ag{110}	4.12	$6 \times 6 \times 6$
Au{111}	4.17	$6 \times 6 \times 6$
Au{100}	4.17	$6 \times 6 \times 6$
Au{110}	4.17	$6 \times 6 \times 6$

**Table A.1:** Table showing the lattice constants and the number of  $k$  points which were used to calculate them.

## A.2 Supercell geometries for CO adsorption calculations

Table A.2 shows the supercell geometries which were used for the CO adsorption energy calculations. As explained earlier,  $n_s$  and  $n_v$  are the number of slab and vacuum layers respectively.

The slab thickness was calculated as

$$d_s = c \frac{n_s}{n_s + n_v} \quad (\text{A.1})$$

where  $c$  is the supercell surface-normal dimension. There is a similar expression for the vacuum thickness,

$$d_v = c \frac{n_v}{n_s + n_v} \quad (\text{A.2})$$

## A.3 Aromatic adsorption computational details

As described in Section 6.2, a smaller number of layers of slab and vacuum were used for the aromatic adsorption calculations on Pt{111}. This was in order to reduce the computational cost due to the larger ( $3 \times 3$ ) lateral dimensions. Four slab layers and seven vacuum layers were used. A single-sided slab was used, where the top two layers were allowed to relax. As for previous chapters, a lattice constant of 3.96 Å was used for Pt.

Surface	$n_s$	$n_v$	$n_{\text{relax}}$	$d_s/\text{\AA}$	$d_v/\text{\AA}$	$c/\text{\AA}$
Rh{111}	9	9	3	20.0	20.0	39.9
Rh{100}	10	10	3	19.2	19.2	38.4
Rh{110}	14	14	4	19.0	19.0	38.1
Pd{111}	8	8	3	18.0	18.0	36.1
Pd{100}	10	10	3	19.5	19.5	38.9
Pd{110}	14	14	4	19.3	19.3	38.5
Pt{111}	8	8	3	18.3	18.3	36.6
Pt{100}	10	10	3	19.8	19.8	39.6
Pt{110}	13	13	4	18.2	18.2	36.4
Cu{111}	9	9	3	18.7	18.7	37.4
Cu{100}	10	10	3	18.1	18.1	36.2
Cu{110}	15	15	4	19.1	19.1	38.2
Ag{111}	8	8	3	19.0	19.0	38.0
Ag{100}	9	9	3	18.5	18.5	37.0
Ag{110}	13	13	4	18.9	18.9	37.8
Au{111}	8	8	3	19.2	19.2	38.5
Au{100}	9	9	3	18.7	18.7	37.5
Au{110}	13	13	4	19.1	19.1	38.3

**Table A.2:** Table showing the numbers of slab and vacuum layers, the number of layers of metal which were relaxed on each side of the slab, the thickness of slab and vacuum and the surface-normal supercell dimension  $c$ .

# References

- [1] J. K. Nørskov, T. Bligaard, J. Rossmeisl and C. H. Christensen, *Nat. Chem.*, 2009, **1**, 37–46.
- [2] R. Jin, G. Li, S. Sharma, Y. Li and X. Du, *Chem. Rev.*, 2021, **121**, 567–648.
- [3] J. Greeley, J. K. Nørskov and M. Mavrikakis, *Annu. Rev. Phys. Chem.*, 2002, **53**, 319–48.
- [4] K. O. Sulaiman and A. T. Onawole, *Comput. Theor. Chem.*, 2016, **1093**, 73–80.
- [5] M. V. Biezma and J. R. S. Cristóbal, *Corrosion*, 2006, **62**, 1051–1055.
- [6] F. Bentiss, M. Lebrini and M. Lagrenée, *Corros. Sci.*, 2005, **47**, 2915–2931.
- [7] A. Turner, *Water Res. X*, 2021, **12**, 100110.
- [8] J. Ko, H. Kwon, H. Kang, B.-K. Kim and J. W. Han, *Phys. Chem. Chem. Phys.*, 2015, **17**, 3123–3130.
- [9] C. H. Bartholomew and R. J. Farrauto, *Fundamentals of Industrial Catalytic Processes*, Wiley, 2005.
- [10] C. Stampfl, M. Veronica Ganduglia-Pirovano, K. Reuter and M. Scheffler, *Surf. Sci.*, 2002, **500**, 368–394.
- [11] J. C. Vedrine, *Catalysts*, 2017, **7**, 341.

- [12] R. Schlögl, *Angew. Chem. Int. Ed.*, 2015, **54**, 3465–3520.
- [13] S. Bhaduri and D. Mukesh, *Homogeneous Catalysis : Mechanisms and Industrial Applications*, Wiley, 2nd edn., 2014.
- [14] P. Sabatier, *Ber. Dtsch. Chem. Ges.*, 1911, **44**, 1984–2001.
- [15] F. H. Ribeiro, A. E. S. VonWittenau, C. H. Bartholomew and G. A. Somorjai, *Catal. Rev. - Sci. Eng.*, 1997, **39**, 49–76.
- [16] A. P. Umpierre, E. de Jesús and J. Dupont, *ChemCatChem*, 2011, **3**, 1413–1418.
- [17] E. Rideal, W. A. Bone, G. Ingle-Finch, E. C. C. Baly, W. C. McC. Lewis, E. Edser, E. F. Armstrong, T. P. Hilditch, H. E. Holtorp and I. Langmuir, *Trans. Faraday Soc.*, 1922, **17**, 655–675.
- [18] G. A. Somorjai, *Surf. Sci.*, 1994, **299–300**, 849–866.
- [19] G. A. Somorjai and Y. Li, *Introduction to Surface Chemistry and Catalysis*, Wiley, Hoboken, N.J., 2nd edn., 2010.
- [20] M. Bowker, *The Basis and Applications of Heterogeneous Catalysis*, Oxford University Press, 1st edn., 2023.
- [21] G. A. Somorjai, *Surf. Sci.*, 1979, **89**, 496–524.
- [22] K. Reuter, C. P. Plaisance, H. Oberhofer and M. Andersen, *J. Chem. Phys.*, 2017, **146**, 040901.
- [23] F. Calle-Vallejo, J. Tymoczko, V. Colic, Q. H. Vu, M. D. Pohl, K. Morgenstern, D. Loffreda, P. Sautet, W. Schuhmann and A. S. Bandarenka, *Science*, 2015, **350**, 185–9.
- [24] G. Ertl, *Handbook of Heterogeneous Catalysis*, Wiley, 2nd edn., 2008.
- [25] T. Zambelli, J. Wintterlin, J. Trost and G. Ertl, *Science*, 1996, **273**, 1688–1690.
- [26] S. H. Hakim, C. Sener, A. C. Alba-Rubio, T. M. Gostanian, B. J.

- O'Neill, F. H. Ribeiro, J. T. Miller and J. A. Dumesic, *J. Catal.*, 2015, **328**, 75–90.
- [27] R. Pestman, W. Chen and E. Hensen, *ACS Catal.*, 2019, **9**, 4189–4195.
- [28] O. R. Inderwildi and S. J. Jenkins, *Chem. Soc. Rev.*, 2008, **37**, 2274–2309.
- [29] F. F. Tao and P. A. Crozier, *Chem. Rev.*, 2016, **116**, 3487–3539.
- [30] S. Vollmer, G. Witte and C. Wöll, *Catal. Lett.*, 2001, **77**, 97–101.
- [31] P. Azadi, G. Brownbridge, I. Kemp, S. Mosbach, J. S. Dennis and M. Kraft, *ChemCatChem*, 2015, **7**, 137–143.
- [32] H. S. Taylor, *J. Phys. Chem.*, 1923, **28**, 897–942.
- [33] H. S. Taylor, *Proc. Math. Phys. Eng. Sci.*, 1925, **108**, 105–111.
- [34] K. Honkala, A. Hellman, I. N. Remediakis, A. Logadottir, A. Carlsson, S. Dahl, C. H. Christensen and J. K. Nørskov, *Science (New York, N.Y.)*, 2005, **307**, 555–558.
- [35] F. Calle-Vallejo, D. Loffreda, M. T. M. Koper and P. Sautet, *Nat. Chem.*, 2015, **7**, 403–10.
- [36] J. K. Nørskov, T. Bligaard, B. Hvolbæk, F. Abild-Pedersen, I. Chorkendorff and C. H. Christensen, *Chem. Soc. Rev.*, 2008, **37**, 2163.
- [37] K. Mudiyansele, F. Xu, F. M. Hoffmann, J. Hrbek, I. Waluyo, J. A. Boscoboinik and D. J. Stacchiola, *Phys. Chem. Chem. Phys.*, 2015, **17**, 3032–3038.
- [38] H. Chermette, *J. Comput. Chem.*, 1999, **20**, 129–154.
- [39] R. G. Parr and W. T. Yang, *J. Am. Chem. Soc.*, 1984, **106**, 4049–4050.
- [40] W. Yang and R. G. Parr, *Proc. Natl. Acad. Sci. U.S.A.*, 1985, **82**, 6723–6726.
- [41] R. G. Pearson, *J. Am. Chem. Soc.*, 1963, **85**, 3533–3539.

- [42] P. W. Ayers, R. G. Parr and R. G. Pearson, *J. Chem. Phys.*, 2006, **124**, 194107.
- [43] M. Berkowitz and R. G. Parr, *J. Chem. Phys.*, 1988, **88**, 2554.
- [44] T. C. Allison and Y. J. Tong, *Electrochim. Acta*, 2013, **101**, 334–340.
- [45] R. G. Parr and R. G. Pearson, *J. Am. Chem. Soc.*, 1983, **105**, 7512–7516.
- [46] W. Yang and W. J. Mortier, *J. Am. Chem. Soc.*, 1986, **108**, 5708–11.
- [47] B. Hammer and J. Nørskov, *Surf. Sci.*, 1995, **343**, 211–220.
- [48] B. Hammer and J. K. Nørskov, *Nature*, 1995, **376**, 238–240.
- [49] S. Jiao, X. Fu and H. Huang, *Adv. Funct. Mater.*, 2022, **32**, 2107651.
- [50] B. Hammer, O. H. Nielsen and J. K. Nørskov, *Catal. Lett.*, 1997, **46**, 31–35.
- [51] S. Zhao, Y. Tang, X. Yu and J. Li, *Sci. China Mater.*, 2023, **66**, 3912–3921.
- [52] N. V. Dokhlikova, M. V. Grishin and S. V. Doronin, *Int. J. Quantum Chem.*, 2023, e27242.
- [53] S. Wilke, M. Cohen and M. Scheffler, *Phys. Rev. Lett.*, 1996, **77**, 1560–1563.
- [54] J. H. Stenlid, A. J. Johansson and T. Brinck, *Phys. Chem. Chem. Phys.*, 2019, **21**, 17001–17009.
- [55] M. Galvan, A. Dal Pino, J. Wang and J. D. Joannopoulos, *J. Phys. Chem.*, 1993, **97**, 783–785.
- [56] C. Morell, A. Grand and A. Toro-Labbé, *J. Phys. Chem. A*, 2005, **109**, 205–212.
- [57] V. Tognetti, C. Morell and L. Joubert, *J. Comput. Chem.*, 2015, **36**, 649–659.

- [58] R. Balawender and L. Komorowski, *J. Chem. Phys.*, 1998, **109**, 5203.
- [59] B. Huang, L. Xiao, J. Lu and L. Zhuang, *Angew. Chem. Int. Ed.*, 2016, **55**, 6239–6243.
- [60] A. Miller, *MSci Thesis*, University of Cambridge, 2014.
- [61] G. Makov and M. C. Payne, *Phys. Rev. B*, 1995, **51**, 4014–4022.
- [62] I. Dabo, B. Kozinsky, N. Singh-Miller and N. Marzari, *Phys. Rev. B*, 2008, **77**, 115139.
- [63] E. Schrödinger, *Ann. Phys. (Berl.)*, 1926, **384**, 361–376.
- [64] E. Schrödinger, *Ann. Phys. (Berl.)*, 1926, **384**, 489–527.
- [65] W. Heisenberg, *Z. Physik*, 1925, **33**, 879–893.
- [66] P. W. Atkins and R. S. Friedman, *Molecular Quantum Mechanics*, Oxford University Press, 5th edn., 2010.
- [67] M. C. Payne, M. P. Teter and D. C. Allan, *Rev. Mod. Phys.*, 1992, **64**, 1045–1097.
- [68] P. A. M. Dirac, *Proc. R. Soc. A.*, 1929, **123**, 714–733.
- [69] S. M. McMurry, *Quantum Mechanics*, Addison-Wesley, 1994.
- [70] Y. Li and G. Wahnstrom, *Phys. Rev. Lett.*, 1992, **68**, 3444–3447.
- [71] B. G. Pfrommer, M. Côté, S. G. Louie and M. L. Cohen, *J. Comput. Phys.*, 1997, **131**, 233–240.
- [72] P. Hohenberg and W. Kohn, *Phys. Rev.*, 1964, **136**, B864–B871.
- [73] W. Kohn and L.J. Sham, *Phys. Rev.*, 1965, **140**, A1133–A1138.
- [74] R. G. Parr and W. Yang, *Density-Functional Theory of Atoms and Molecules*, Oxford University Press, 1989.
- [75] L. H. Thomas, *Proc. Cambridge Philos. Soc.*, 1927, **23**, 542–548.
- [76] E. Fermi, *Z. Physik*, 1928, **48**, 73–79.

- [77] R. G. Parr and W. Yang, *Annu. Rev. Phys. Chem.*, 1995, **46**, 701–728.
- [78] N. Lang, *Solid State Commun.*, 1969, **7**, 1047–1050.
- [79] N. D. Lang and W. Kohn, *Phys. Rev. B*, 1970, **1**, 4555–4568.
- [80] N. Lang and W. Kohn, *Phys. Rev. B*, 1971, **3**, 1215–1223.
- [81] B. Mrowka and A. Recknagel, *Phys. Z.*, 1937, **38**, 758.
- [82] E. Teller, *Rev. Mod. Phys.*, 1962, **34**, 627–631.
- [83] K. Burke, *J. Chem. Phys.*, 2012, **136**, 150901.
- [84] M. C. Holthausen and W. Koch, *A Chemist’s Guide to Density Functional Theory*, Wiley, 2nd edn., 2007.
- [85] D. M. Ceperley and B. J. Alder, *Phys. Rev. Lett.*, 1980, **45**, 566–569.
- [86] J. P. Perdew and Y. Wang, *Phys. Rev. B*, 1992, **45**, 13244–13249.
- [87] J. P. Perdew, K. Burke and M. Ernzerhof, *Phys. Rev. Lett.*, 1996, **77**, 3865–3868.
- [88] R. J. Bartlett and M. Musiał, *Rev. Mod. Phys.*, 2007, **79**, 291–352.
- [89] A. J. W. Thom, *Phys. Rev. Lett.*, 2010, **105**, 263004.
- [90] W. Kohn, A. D. Becke and R. G. Parr, *J. Phys. Chem.*, 1996, **100**, 12974–12980.
- [91] R. Car and M. Parrinello, *Phys. Rev. Lett.*, 1985, **55**, 2471–2474.
- [92] M. D. Segall, P. J. D. Lindan, M. J. Probert, C. J. Pickard, P. J. Hasnip, S. J. Clark and M. C. Payne, *J. Phys. Condens. Matter*, 2002, **14**, 2717–2744.
- [93] D. Vanderbilt, *Phys. Rev. B*, 1990, **41**, 7892–7895.
- [94] V. Eyert, *J. Comput. Phys.*, 1996, **124**, 271–285.
- [95] Y. Iwasawa, R. Mason, M. Textor and G. A. Somorjai, *Chem. Phys. Lett.*, 1976, **44**, 468–470.

- [96] S. J. Jenkins and S. J. Pratt, *Surf. Sci. Rep.*, 2007, **62**, 373–429.
- [97] S. J. Clark, M. D. Segall, C. J. Pickard, P. J. Hasnip, M. I. J. Probert, K. Refson and M. C. Payne, *Z. Kristallogr. Cryst. Mater.*, 2005, **220**, 567–570.
- [98] H. J. Monkhorst and J. D. Pack, *Phys. Rev. B*, 1976, **13**, 5188–5192.
- [99] H. M. Al-Allak and S. J. Clark, *Phys. Rev. B*, 2001, **63**, 033311.
- [100] M. Stengel and N. Spaldin, *Phys. Rev. B*, 2007, **75**, 205121.
- [101] R. J. Nicholls, A. J. Morris, C. J. Pickard and J. R. Yates, *J. Phys.: Conf. Ser.*, 2012, **371**, 012062.
- [102] A. J. Morris, R. J. Nicholls, C. J. Pickard and J. R. Yates, *Comput. Phys. Commun.*, 2014, **185**, 1477–1485.
- [103] C. J. Pickard and M. C. Payne, *Phys. Rev. B*, 1999, **59**, 4685–4693.
- [104] C. J. Pickard and M. C. Payne, *Phys. Rev. B*, 2000, **62**, 4383–4388.
- [105] J. R. Yates, X. Wang, D. Vanderbilt and I. Souza, *Phys. Rev. B*, 2007, **75**, 195121.
- [106] L. R. Rabiner, *Theory and Application of Digital Signal Processing*, Prentice-Hall, 1975.
- [107] L. R. Rabiner, *Digital Processing of Speech Signals*, Prentice-Hall, 1978.
- [108] L. Aballe, A. Barinov, N. Stojić, N. Binggeli, T. O. Mendes, A. Locatelli and M. Kiskinova, *J. Phys. Condens. Matter*, 2010, **22**, 015001.
- [109] S. D. Kevan, *Phys. Rev. Lett.*, 1983, **50**, 526–529.
- [110] N. Smith and D. Woodruff, *Prog. Surf. Sci.*, 1986, **21**, 295–370.
- [111] P. O. Gartland and B. J. Slagsvold, *Phys. Rev. B*, 1975, **12**, 4047–4058.
- [112] D. Wei, D. Skelton and S. Kevan, *Surf. Sci.*, 1997, **381**, 49–64.
- [113] F. Abild-Pedersen and M. P. Andersson, *Surf. Sci.*, 2007, **601**, 1747–1753.

- [114] R. F. W. Bader, *Atoms in Molecules: A Quantum Theory*, Oxford University Press, 1st edn., 1990.
- [115] R. F. W. Bader, *J. Phys. Chem. A*, 2010, **114**, 7431–44.
- [116] J. Batteas, A. Barbieri, E. Starkey, M. Van Hove and G. A. Somorjai, *Surf. Sci.*, 1994, **313**, 341–348.
- [117] R. Marbrow and R. Lambert, *Surf. Sci.*, 1977, **67**, 489–500.
- [118] V. R. Dhanak, A. Baraldi, G. Comelli, G. Paolucci, M. Kiskinova and R. Rosei, *Surf. Sci.*, 1993, **295**, 287–294.
- [119] C. M. Comrie and R. M. Lambert, *J. Chem. Soc., Faraday trans.*, 1976, **72**, 1659–1669.
- [120] R. L. Park and H. H. Madden, *Surf. Sci.*, 1968, **11**, 188–202.
- [121] R. J. Behm, K. Christmann, G. Ertl, M. A. Van Hove, P. A. Thiel and W. H. Weinberg, *Surf. Sci.*, 1979, **88**, L59–L66.
- [122] R. Raval, S. Haq, M. Harrison, G. Blyholder and D. King, *Chem. Phys. Lett.*, 1990, **167**, 391–398.
- [123] R. J. Behm, P. A. Thiel, P. R. Norton and G. Ertl, *J. Chem. Phys.*, 1983, **78**, 7437–7447.
- [124] P. A. Thiel, R. J. Behm, P. R. Norton and G. Ertl, *J. Chem. Phys.*, 1983, **78**, 7448–7458.
- [125] G. McElhiney, H. Papp and J. Pritchard, *Surf. Sci.*, 1976, **54**, 617–634.
- [126] W. Hansen, M. Bertolo and K. Jacobi, *Surf. Sci.*, 1991, **253**, 1–12.
- [127] U. Burghaus, L. Vattuone, P. Gambardella and M. Rocca, *Surf. Sci.*, 1997, **374**, 1–8.
- [128] S. Krause, C. Mariani, K. C. Prince and K. Horn, *Surf. Sci.*, 1984, **138**, 305–318.
- [129] S. A. C. Carabineiro and B. E. Nieuwenhuys, *Gold Bull.*, 2009, **42**, 288–301.

- [130] L. Piccolo, D. Loffreda, F. Aires, C. Deranlot, Y. Jugnet, P. Sautet and J. C. Bertolini, *Surf. Sci.*, 2004, **566**, 995–1000.
- [131] M. S. Pierce, K.-C. Chang, D. C. Hennessy, V. Komanicky, A. Menzel and H. You, *J. Phys. Chem. C*, 2008, **112**, 2231–2234.
- [132] I. Nakamura, A. Takahashi and T. Fujitani, *Catal. Lett.*, 2009, **129**, 400–403.
- [133] Y. Jugnet, F. J. Cadete Santos Aires, C. Deranlot, L. Piccolo and J. C. Bertolini, *Surf. Sci.*, 2002, **521**, L639–L644.
- [134] A. Sandell, P. Bennich, A. Nilsson, B. Hernnas, O. Bjorneholm and N. Martensson, *Surf. Sci.*, 1994, **310**, 16–26.
- [135] R. Meyer, C. Lemire, S. K. Shaikhutdinov and H. Freund, *Gold Bull.*, 2004, **37**, 72–124.
- [136] J. M. Gottfried, K. J. Schmidt, S. L. M. Schroeder and K. Christmann, *Surf. Sci.*, 2003, **536**, 206–224.
- [137] K. F. Peters, P. Steadman, H. Isern, J. Alvarez and S. Ferrer, *Surf. Sci.*, 2000, **467**, 10–22.
- [138] W. A. Brown, R. Kose and D. A. King, *Chem. Rev.*, 1998, **98**, 797–832.
- [139] Q. Ge, R. Kose and D. A. King, in *Advances in Catalysis*, Elsevier, 2000, vol. 45, pp. 207–259.
- [140] S. J. Jenkins, *Proc. Math. Phys. Eng. Sci.*, 2009, **465**, 2949–2976.
- [141] A. Tkatchenko and M. Scheffler, *Phys. Rev. Lett.*, 2009, **102**, 6–9.
- [142] E. R. McNellis, J. Meyer and K. Reuter, *Phys. Rev. B*, 2009, **80**, 205414.
- [143] J. Clayden, *Organic Chemistry Jonathan Clayden, Nick Greeves, Stuart Warren.*, Oxford University Press, 2nd edn., 2012.
- [144] Y. P. Tan, S. Khatua, S. J. Jenkins, J. Q. Yu, J. B. Spencer and D. A. King, *Surf. Sci.*, 2005, **589**, 173–183.

- [145] S. Yamagishi, S. J. Jenkins and D. A. King, *J. Chem. Phys.*, 2001, **114**, 5765–5773.
- [146] L. M. Falicov and G. A. Somorjai, *Proc. Natl. Acad. Sci. U.S.A.*, 1985, **82**, 2207–11.